Terms and Conditions of Use of Digitised Theses from Trinity College Library Dublin

Copyright statement

All material supplied by Trinity College Library is protected by copyright (under the Copyright and Related Rights Act, 2000 as amended) and other relevant Intellectual Property Rights. By accessing and using a Digitised Thesis from Trinity College Library you acknowledge that all Intellectual Property Rights in any Works supplied are the sole and exclusive property of the copyright and/or other IPR holder. Specific copyright holders may not be explicitly identified. Use of materials from other sources within a thesis should not be construed as a claim over them.

A non-exclusive, non-transferable licence is hereby granted to those using or reproducing, in whole or in part, the material for valid purposes, providing the copyright owners are acknowledged using the normal conventions. Where specific permission to use material is required, this is identified and such permission must be sought from the copyright holder or agency cited.

Liability statement

By using a Digitised Thesis, I accept that Trinity College Dublin bears no legal responsibility for the accuracy, legality or comprehensiveness of materials contained within the thesis, and that Trinity College Dublin accepts no liability for indirect, consequential, or incidental, damages or losses arising from use of the thesis for whatever reason. Information located in a thesis may be subject to specific use constraints, details of which may not be explicitly described. It is the responsibility of potential and actual users to be aware of such constraints and to abide by them. By making use of material from a digitised thesis, you accept these copyright and disclaimer provisions. Where it is brought to the attention of Trinity College Library that there may be a breach of copyright or other restraint, it is the policy to withdraw or take down access to a thesis while the issue is being resolved.

Access Agreement

By using a Digitised Thesis from Trinity College Library you are bound by the following Terms & Conditions. Please read them carefully.

I have read and I understand the following statement: All material supplied via a Digitised Thesis from Trinity College Library is protected by copyright and other intellectual property rights, and duplication or sale of all or part of any of a thesis is not permitted, except that material may be duplicated by you for your research use or for educational purposes in electronic or print form providing the copyright owners are acknowledged using the normal conventions. You must obtain permission for any other use. Electronic or print copies may not be offered, whether for sale or otherwise to anyone. This copy has been supplied on the understanding that it is copyright material and that no quotation from the thesis may be published without proper acknowledgement.

Optical characterisation and manipulation of active microspheres

by

Matthias Gerlach

A thesis submitted for the degree of Doctor of Philosophy in the University of Dublin

Under the supervision of

Prof. John F. Donegan

School of Physics,

Trinity College,

Dublin.

May 2007

Declaration

This thesis has not been submitted as an exercise for a degree at this or any other university. The work presented is entirely my own, apart from the assistance mentioned in the acknowledgements. I agree that Trinity College Library may lend or copy this thesis upon request.

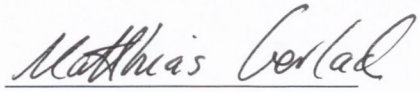

Matthias Gerlach

May, 2007.

Abstract

Spherical microcavities are of great interest for both photonic applications and for fundamental physics. In this thesis, a novel active dielectric microsphere emitter coated with colloidal CdTe nanocrystals is studied. In the first experimental part of the thesis, the microsphere emitter was optically characterized in a micro-photoluminescence/micro-Raman setup. Strong enhancement of photoluminescence and Raman scattering was observed due to the optical feedback in the microcavity. At excitation below the bandgap, anti-Stokes photoluminescence was observed due to an efficient phonon-assisted up-conversion process. In the second part of the thesis, a novel type of an active microsphere emitter was fabricated for an optical trapping experiment. The microsphere was coated with a several nanometer thick polyelectrolyte multilayer and the layer was additionally softened with a chemical treatment. The elastic polyelectrolyte shell was then coated with a monolayer of CdTe nanocrystals. Controlled radiation force deformed the elastic shell of the microsphere in contact with a substrate. The deformation induced a lifting of the azimuthal mode degeneracy and therefore a splitting of the azimuthal resonances which was observed in the photoluminescence spectrum. This experiment demonstrates the first all-optical deformation of a solid microsphere by radiation pressure. Optical switching of resonances based on the radiation pressure controlled deformation is shown. In the third part in this thesis, the intersphere mode coupling in a bi-sphere system is demonstrated. Coherent and weak coupling is observed under different coupling conditions. Highly efficient optical coupling was observed in the strong coupling regime. The weakly coupled bi-sphere system was studied in regards to optical mode switching. The potential for switching devices based on the bi-sphere system in optical communications is briefly discussed.

Acknowledgements

Very special thanks go to my supervisor Professor John Donegan who is also head of this research group and to Dr. Yury Rakovich, my day to day supervisor. Both gave me a lot of support and helped me to gather a lot of knowledge in the photonics area.

I would like to acknowledge the contribution of Ronan Daly, Professor John Boland, Dr. Nikolai Gaponik and Dr. Andrey Rogach for the collaboration. Thanks to Dr. Tania Perova for her support with the PL/Raman setup. I would like to thank Steven J. Byrne for synthesizing the nanocrystals and Dr. Yurii Gun'ko and his group of the School of Chemistry for allowing me to use their lab.

I would like to thank all our present and former group members for their help and support. Especially Torsten who was a good companion, also outside college, and John O'Dowd, my desk neighbour, who always stimulated helpful discussions. Thanks to Seve, Mick & Tina and Pablo for the Friday after-work pint which was always good fun.

I would like to acknowledge the help from the mechanical workshop, from Ken when encountering computer problems, Nigel for his help in fixing electronic equipment, Marie Kinsella and John Kelly.

Yet another special thanks goes to all my new friends I met in and outside college and especially to Diana.

Finally, I would like to thank my parents and my brother for their great support over the years.

Publications

M. Gerlach, Yu. P. Rakovich, and J. F. Donegan, "*Radiation-pressure-induced mode splitting in a spherical microcavity with an elastic shell*", Opt. Exp., vol. 15, n. 6, 2007, p 3597-3606.

M. Gerlach, Yu. P. Rakovich, and J. F. Donegan, "*Radiation-pressure-induced mode splitting in a spherical microcavity with an elastic shell*", Virtual Journal of Biological Physics Research, vol. 13, n. 7, 2007.

M. Gerlach, Yu. P. Rakovich, J. F. Donegan, N. Gaponik, and A. L. Rogach, "*Radiation pressure induced splitting of resonant modes in a nanocrystal-coated Microcavity*", Physica Status Solidi C, n 11, 2006, p 3689-92.

Yu. P. Rakovich, N. Gaponik, A. L. Rogach, M. Gerlach, A. L. Bradley, T. Connolly, J. J. Boland, and J. F. Donegan, "*Coupled cavity modes in photonic molecules with semiconductor nanocrystals*", Proceedings of the SPIE - The International Society for Optical Engineering, vol. 5840, n. 1, 2005, p 572-83.

Yu. P. Rakovich, M. Gerlach, A. L. Bradley, J. F. Donegan, T. Connolly, J. J. Boland, N. Gaponik, and A. L. Rogach , "*Photonic molecules modes in resonantly coupled spherical microcavities with semiconductor nanocrystals*", Proceedings of the SPIE - The International Society for Optical Engineering, v 5825, n 1, 2005, p 73-84.

M. Gerlach, Yu. P. Rakovich, J. F. Donegan, N. Gaponik, and A. L. Rogach, "*Enhanced coupling of electronic and photonic states in a microcavity-quantum dot system*", Proceedings of the SPIE - The International Society for Optical Engineering, v 5825, n 1, 2005, p 370-7.

Yu. P. Rakovich, N. Gaponik, and A. L. Rogach, M. Gerlach, A. L. Bradley, T. Connolly, J. J. Boland, and J. F. Donegan, "*Coupled cavity modes in photonic molecules with semiconductor nanocrystals*", Proceedings of SPIE - The International Society for Optical Engineering, v 5840 PART II, Photonic Materials, Devices, and Applications, 2005, p 572-583.

K. I. Rusakov, A. A. Gladyshchuk, Yu. P. Rakovich, M. Gerlach, J. F. Donegan, T. M. Connolly, J. J. Boland, N. Gaponik, and A. L. Rogach, "*Modification of photon states in photonic molecules with semiconductor nanocrystals*", Optics and Spectroscopy (English translation of Optika i Spektroskopiya), v 99, n 3, September, 2005, p 493-497.

J. F. Donegan, Yu. P. Rakovich, M. Gerlach, T. M. Connolly, J. J. Boland, N. Gaponik, and A. L. Rogach, "*Photonic molecules: a new concept for wavelength tunable optical delay*", Proceedings of 2005 7th International Conference on Transparent Optical Networks (IEEE Cat. No. 05EX1100), 2005, pt. 2, p 116-19 Vol. 2.

Yu. P. Rakovich, M. Gerlach, A. L. Bradley, J. F. Donegan, T. Connolly, J. J. Boland, N. Gaponik, and A. L. Rogach, "*Photonic molecules modes in resonantly coupled spherical microcavities with semiconductor nanocrystals*', Proceedings of SPIE - The International Society for Optical Engineering, v 5825, Opto-Ireland 2005: Optoelectronics, Photonic Devices, and Optical Networks, 2005, p 73-84.

M. Gerlach, Yu. P. Rakovich, J. F. Donegan, N. Gaponik, and A. L. Rogach, "*Enhanced coupling of electronic and photonic states in a microcavity-quantum dot system*", Proceedings of SPIE - The International Society for Optical Engineering, v 5825, Opto-Ireland 2005: Optoelectronics, Photonic Devices, and Optical Networks, 2005, p 370-377.

Yu. P. Rakovich, M. Gerlach, A. L. Bradley, J. F. Donegan, J. J. Boland, T. Connolly, M. Przyjalgowski, A. Ryder, N. Gaponik, and A. L. Rogach, "*Spontaneous emission from semiconductor nanocrystals in coupled spherical microcavities*", Physica Status Solidi C: Conferences, vol. 2, n. 2, 2005, p 858-861.

K. I. Rusakov, A. A. Gladyshchuk, Yu. P. Rakovich, M. Gerlach, T. M. Connolly, J. J. Boland, N. Gaponik, and A. L. Rogach, "*Modification of photon states in photonic molecules with semiconductor nanocrystals*", Optics and Spectroscopy, Sept. 2005, p 493-7.

Yu. P. Rakovich, M. Gerlach, J. F. Donegan, N. Gaponik, and A. L. Rogach, "*Three-dimensional photon confinement in a spherical microcavity with CdTe quantum dots: Raman spectroscopy*", Physica E, vol. 26, n. 1-4, Feb. 2005, p 28-32.

Yu. P. Rakovich, M. Gerlach, A. L. Bradley, J. F. Donegan, T. Connolly, J. J. Boland, M. Przyjalgowski, A. Ryder, N. Gaponik, and A. L. Rogach, "*Confined optical modes in small photonic molecules with semiconductor nanocrystals*", Journal of Applied Physics, v 96, n 11, Dec 1, 2004, p 6761-6765.

Yu. P. Rakovich, J. F. Donegan, M. Gerlach, A. L. Bradley, T. Connolly, J. J. Boland, N. Gaponik, and A. L. Rogach, "*Fine structure of coupled optical modes in photonic molecules*" Physical Review A - Atomic, Molecular, and Optical Physics, v 70, n 5 A, November, 2004, p 051801-1-051801-4.

Conferences

"*Radiation pressure induced splitting of resonant modes in a nanocrystal-coated microcavity*", M. Gerlach, Yu. P. Rakovich , J. F. Donegan, N. Gaponik, and A. L. Rogach, presented at the Quantum Dots 2006 conference in Chamonix (France).

"*Controlled splitting of resonant modes in spherical microcavities confined in an optical tweezers*", M. Gerlach, Yu. P. Rakovich , J. F. Donegan, N. Gaponik, and A. L. Rogach, presented at the Photon06 conference 2006 in Manchester (UK).

"*Manipulation of whispering gallery modes in a microsphere through an optical microscope*", M. Gerlach, Yu. P. Rakovich , J. F. Donegan, N. Gaponik, and A. L. Rogach, presented at the Microscopic Society of Ireland 30th Annual Symposium 2006, National University of Ireland-Galway, Dublin (IRE).

"*Enhanced coupling of electronic and photonic states in a microcavity quantum-dot system*", M. Gerlach, Yu. P. Rakovich , J. F. Donegan, N. Gaponik, and A. L. Rogach, presented at the SPIE Opto Ireland conference 2005, Dublin (IRE).

"*Photonic molecule modes in resonantly coupled spherical microcavities with semiconductor nanocrystals*", Yu. P. Rakovich, M. Gerlach, J. F. Donegan, N. Gaponik, and A. L. Rogach, presented at the SPIE Opto Ireland conference 2005, Dublin (IRE).

"*Photoluminescence spectrum of levitated microspheres*", M. Gerlach, Yu. P. Rakovich , J. F. Donegan, N. Gaponik, and A. L. Rogach, presented at the Microscopic Society of Ireland 29th Annual Symposium 2005, DIT, Dublin (IRE).

"*Wavelength tunable optical mode lifetimes in photonic molecules: new concept for multiplexing and delaying an optical signal*", Yu. P. Rakovich, M. Gerlach, A. L. Bradley, J. F. Donegan, T. Connolly, J. J. Boland, N. Gaponik, and A. L. Rogach, presented at the CLEO EUROPE 2005 conference, Munich (Germany).

"*Photobleaching and resonant mode shift in a microsphere-quantum dot system*", Yu. P. Rakovich, M. Gerlach, A. L. Bradley, J. F. Donegan, T. Connolly, J. J. Boland, N. Gaponik, and A. L. Rogach, presented at the CLEO EUROPE 2005 conference, Munich (Germany).

"*Three-dimensional photon confinement in a spherical microcavity with CdTe quantum dots: Raman spectroscopy*", Yu. P. Rakovich, M. Gerlach, J. F. Donegan, N. Gaponik, and A. L. Rogach, presented at the Quantum Dots 2004 conference, Banff, Canada.

"*Micro-Raman studies on a nanocrystal-microcavity system*", M. Gerlach, Yu. P. Rakovich , J. F. Donegan, N. Gaponik, and A. L. Rogach, presented at the Microscopic Society of Ireland 28th Annual Symposium 2004, Trinity College, Dublin (IRE).

"*Three-dimensional Photon Confinement in a Spherical Microcavity with CdTe Quantum Dots: Raman Spectroscopy*", M. Gerlach, Yu. P. Rakovich , J. F. Donegan, N. Gaponik, and A. L. Rogach, presented at the ETOS 2004 conference, Cork (IRE).

Table of Contents

Chapter 4: Raman scattering and photoluminescence from a composite nanocrystals-microcavity system

Chapter 5: Radiation pressure induced mode splitting in a spherical microcavity with an elastic shell

Chapter 6: Resonance mode coupling in a bi-sphere system

Chapter 7: Conclusions and future work

Acronyms

WGM(s)	Whispering gallery mode(s)
Q-factor	Quality factor
PL	Photoluminescence
PE	Polyelectrolyte
PS	Polystyrene
MF	Melamine Formaldehyde
TGA	Thioglycolic acid
PAH	Poly(allylamine hydrochloride)
PSS	Poly(sodium 4-styrenesulfonate)
LbL	Layer-by-layer
CQED	Cavity quantum electrodynamics
TE	Transverse-electric
TM	Transverse-magnetic
N. A.	Numerical aperture
GLMT	Generalized Lorenz-Mie theory
MOEMS	Micro-optical-electromechanical systems
DWDM	Dense wavelength division multiplexing
PM	Photonic molecule
ABN	anti-bonding
BN	bonding
MTA	Maximum term approximation
SMTB	Single-mode tight-binding method

Chapter 1

Introduction and thesis overview

1.1 Introduction

In fundamental physics and in photonics technology, microcavities with high finesse and high quality (Q)-factor are key optical elements for modern linear and non-linear optics. Spherical microcavities provide unique properties with an extremely high Q-factors and a small mode volume. The research on spherical microcavities can be roughly separated into two areas: the small microsphere regime, with sizes of a maximum diameter of several tens of microns, and the large microsphere regime, with up to several hundreds of microns diameter. While large microspheres provide ultra-high Q-factors (up to 10^{10} [1]), a, small spheres possess a moderate Q-factor (up to 10^{5}) but with a smaller mode volume.

A very common method to produce large microspheres is fusing fibre tips in a flame or in a CO_2 laser beam. The melted tip forms a sphere or spheroid by surface tension at the very end of the fibre attached to the fibre stem. The advantage of these microspheres is the easier handling because the sphere is still attached to a fibre. However, it is extremely difficult to produce very small spheres by this method. The diameters of these large spheres are commonly between $50\ \mu m$ and $200\ \mu m$. Small spheres are commonly silica or polymer particles which are commercially available. One of the main goals for using whispering gallery mode (WGM) cavities is the enhancement of the radiative rate by what is known as the Purcell effect. The Purcell factor expresses the enhancement of the spontaneous emission rate of an emitter in a resonator in relation to the emission rate of the emitter in vacuum. It is proportional to (Q/V), where Q is the quality factor and V the effective mode volume of the micro-resonator. Even in a small sphere with moderate Q, the Purcell factor can be comparable to that of a big sphere due to the smaller mode volume. The work in this thesis is focused on the smaller microspheres. The first

experiments were carried out with *70* microns spheres while spheres of only *3* microns in diameter were used in the optical trapping experimental work.

Apart from the sphere size, a further discrimination in spherical microcavities is to distinguish between passive and active resonators. Passive devices possess no active materials such as doping or coatings and consequently do not emit radiation generated by the device. Passive microsphere resonators are often used in cavity QED (CQED) experiments. In this area, the interaction between electronic quantised energy levels of single atoms or molecules and the extremely narrow optical resonances of the microcavity is studied. These experiments require a high Purcell factor, which is a unique feature of spherical microcavities of high optical quality. Many research groups have studied CQED in combination with microspheres in recent years. For example, coupling of atoms to microcavities is discussed in [2]. A recent CQED experiment published in 2006 demonstrates strong exciton-photon coupling of nanocrystals with the optical modes of a microsphere [3]. Another coupling experiment which investigates controlled coupling of a single nanoparticle to a microsphere is published in [4]. In this thesis, the area of active microcavities is studied. These microcavities employ optically active material, which emit light when excited with a pump source. Very common active materials are dyes, rare-earth ions or semiconductor nanocrystals. The microcavity active volume can be doped with colloidal nanocrystals and rare-earth ions or coated with dyes or nanocrystals on the surface. In the microsphere, the light is confined into an extremely small mode volume, which causes high field density and a long photon storage lifetime, reaching the micro-seconds regime in high-Q spheres. Therefore, microspheres provide strong enhancement of both linear and non-linear optical processes when the optical modes interact with the active material. Nanocrystals are of particular interest as they offer considerably higher photostability than dyes. Further unique optical properties such as adjustable emission wavelength due to the tuneable electronic energy level properties generate great interest for nanocrystals as building blocks for novel light sources. The physical properties of colloidal nanocrystals are complex and are still the subject of intense investigation. Optimising the growing process and applying a suitable capping agent is an important factor for good stable optical properties of the nanocrystals. Thioglycolic acid capped CdTe nanocrystals were used as the chief active material for this thesis. Detailed information about the nanocrystals utilised in this project can be found in [5], where the fabrication process and

optical characterisation is discussed. The colloidal nanocrystals are deposited on the sphere surface by a layer-by-layer (LbL) technique [6], which is a widely used method. It was first applied to flat substrates before successfully brought forward to coat spherical particles.

Amongst others, the composite system consisting of nanocrystals and a dielectric microsphere is the basis of research on microsphere lasers. The extremely high Q-factors of microspheres allow the development of lasers with very narrow linewidth and low threshold. Research was focused on the realisation of low threshold microcavity lasers in recent years. One type of laser was implemented with rare-earth doped microspheres. The fused microspheres itself were usually made of silica or different types of glasses, such as fluoride, phosphate, ZBLAN, fluoro-zirconate or tellurite glass. The doping materials were neodymium [7, 8], erbium [9-14], erbium:ytterbium [15], or thulium [16]. All these materials show radiative emission due to up-conversion processes and recombination within ion transition levels, respectively. The emission wavelength is determined by the radiative transition levels in the ions. Lasing was realised mainly around 1.5 μm, which is the very convenient low absorption window of silica fibres, commonly used for data transmission in optical communications. The active ion-doped material can also be applied on the sphere surface. A low-threshold laser was realised with a silica sphere coated with erbium-doped solgel films in [17]. The main limitation of ion-doped lasers is the fact that the emission wavelength is fixed to the energy transition levels. This shows that the advantage of the nanocrystal-coated active microspheres studied in this thesis. The emission of nanocrystals is highly tuneable by size over a broad spectral range, depending on the semiconductor material applied for growing the nanocrystals. One of the objectives in this thesis is the optical characterisation of a novel nanocrystals-microsphere emitter, where the nanocrystals are deposited on the sphere surface. Similar active microsphere resonators based on CdSe nanocrystals were studied in [18, 19]. In these publications, the enhancement of the spontaneous emission rate of a nano-emitter interacting with the spherical microcavity was studied. Furthermore, the positioning of the nano-emitter within the microcavity is studied. Based on their results which approve strong enhancement of the emission rate, experimental studies of enhanced Raman scattering and photoluminescence are carried out in this thesis. CdSe/ZnS core/shell nanocrystals were studied in [20]. In this publication, the time-resolved photoluminescence in the nanosecond regime from the nanocrystals embedded in the microsphere is studied. In this thesis, experimental studies

on photoluminescence decay at continuous excitation on a larger time-scale are discussed. A fused-silica microsphere laser coated with HgTe nanocrystals is presented in [21]. HgTe nanocrystals provide strong infrared luminescence at room temperature over a broad spectrum between 1200 nm and 2000 nm, while emission of CdTe and CdSe is in the visible region. A nanocrystal-based microsphere laser is demonstrated in [22]. The authors observed stimulated emission from the active microsphere emitter which is a promising result for potential visible microlaser applications, realised with nanocrystal-coated microspheres whose optical properties are studied in this thesis.

In this thesis, a novel approach of sphere-deformation was investigated. A several nanometer thick polyelectrolyte (PE) multilayer was deposited on the surface of the sphere and additionally softened to achieve an elastic layer. The nanocrystals were deposited on top of the PE layer. Initial experimental work was carried out to study the effect of elastic deformation on the whispering gallery modes. Several groups have carried out experimental work in sphere-deformation to realise tuning of the optical resonances [23-25]. The tuning was achieved by mechanical stress applied to the sphere, which deforms the microcavity. Additional bulky equipment is required to tune the modes in these experiments. Apart from mode tuning, mode splitting due to deformation is achieved by lifting the azimuthal mode degeneracy. This is for example observed in a liquid ethanol droplet [26] or in a laser-melted polystyrene microsphere [27]. In this thesis, mode tuning was observed by a thermally-induced refractive index change. The advantage is that no further equipment is required. However, it is not applicable for experiments where constant or low temperature is needed (CQED at low temperatures) but applicable in less temperature sensitive applications in optical communications. For example, a thermo-optical switch based on a microsphere coated with a polymer is demonstrated in [28]. Extensive research has been carried out in the field of optical tweezing in recent years, following the fundamental work of Ashkin [29] who discovered the optical tweezing effect. Optical tweezers gained particular interest in the biological sector for handling bacteria, cells or molecules or trapping and manipulation of atoms and particles in the micrometer regime [30, 31]. To our knowledge, radiation pressure deformation of spherical particles was only published so far on liquid droplets [32-34]. In this thesis, new experimental work for a novel approach of all-optical deformation of spherical microcavities is demonstrated. The experimental work provides fundamental knowledge

for studying the potential of soft-shell active microsphere-emitter as a device for research or applications in photonics.

1.2 Thesis overview

Chapter one is a general introduction and a literature review. Chapter 2 introduced the two components of the active microsphere emitter: the colloidal nanocrystals which were deposited on the surface of the sphere and the microsphere itself. The optical properties and the fabrication process of the nanocrystals are briefly discussed. The characterisation of the active microcavity is the target of the composite system consisting of the microcavity and the nanocrystal layer. The background knowledge about optical resonances (WGMs) in a microsphere is given in this chapter, as well as an introduction to the Mie-scattering theory for calculating the resonance spectrum. The strategy for the derivation of the required analytical formulas from Maxwell's equations is pointed out.

In Chapter 3, the sample preparation procedure for coating the sphere with the polyelectrolyte multilayers and the final CdTe nanocrystal layer is presented. The softening process of the PE multilayers is also discussed. The micro-Raman/micro-luminescence setup and the operation of the machine are introduced. The setup is an enclosed, fully computer controlled machine which was used to gather the experimental results in this thesis.

Chapter 4 is the first experimental chapter, where the optical characterisation of the composite nanocrystal-microcavity system is presented and discussed. The PL and Raman spectrum of a sample with a diameter of $70\ \mu m$ was taken under varying excitation conditions. A strong enhancement of coupling of the optical resonances with the electronic and vibrational states of the nanocryal layer was observed. Strong up-conversion of luminescence and Raman scattering of CdTe nanocrystals was detected due to the optical feedback in the microcavity. The resonance mode identification with an approximation formula was demonstrated. A characteristic intensity modulation of the whispering gallery modes due to interference was observed and finally, characteristic changes in photoluminescence (PL) intensity and mode structure were studied during continuous excitation of the samples over 18 minutes.

In Chapter 5, the experimental work on a novel approach of shape distortion of an active microcavity consisting of a microsphere (*3 μm* diameter) coated with a soft PE shell and the CdTe nanocrystal layer in an optical trap is presented. In this experiment, radiation pressure exerted on a sphere is controlled by the focus position. The theory of radiation pressure is discussed briefly. The applied equations for the theoretical interpretation of the experimental work in this chapter are presented. Theoretical background for deformed spherical objects is given, and azimuthal mode splitting in a deformed microcavity is discussed. The experimental data is presented and discussed on the basis of a mathematical model which was developed for the interpretation of the experimental results. The measurements show a mode shape distortion due to the azimuthal mode splitting induced by radiation pressure. The modelled mode shape fits very well with the experimental data. A temperature-induced blue shift of the optical resonances was also observed and the temperature increase during excitation was estimated from the data. An optical switching experiment is demonstrated based on controlled radiation pressure deformation.

In Chapter 6, work on coupled active microspheres is presented. Coherent and weak coupling in a bi-sphere system is demonstrated. A polystyrene (PS) pore substrate was used to align the spheres and to keep the leakage into the substrate as low as possible. Optical switching between the resonances depending on the focus position based on weak inter-sphere coupling was demonstrated in the final part of this chapter.

The work is summarized in chapter 7, along with the main conclusions of this thesis. Finally, an outlook to future work is given.

References

[1] A. A. Savchenko, V. S. Ilchenko, A. B. Matsko, and L. Maleki, "Kilo-Hertz optical resonances in dielectric crystal cavities", Phys. Rev. A **70**, 804 (2004).

[2] G. Rempe, "Atoms in an optical cavity: quantum electrodynamics in confined space", Contemp. Phys. **34**, 119 (1993).

[3] N. Le Thomas, U. Woggon, O. Schoeps, M. V. Artemyev, M. Kazes, and U. Banin, "Cavity QED with semiconductor nanocrystals", Nano Letters **6**, 557 (2006).

[4] S. Goetzinger, O. Benson, and V. Sandaghar, "Towards controlled coupling between a high-Q whispering gallery mode and a single nanoparticle", Appl. Phys. B **73**, 825 (2001).

[5] N. Gaponik, D. V. Talapin, A. L. Rogach, K. Hoppe, E. V. Shevchenko, A. Kornowski, A. Eychemueller, and H. Weller, "Thiol-capping of CdTe nanocrystals: An alternative to organometallic synthetic routes", J. Phys. Chem. B. **106**, 7177 (2002).

[6] A. S. Susha, F. Caruso, A. L. Rogach, G. B. Sukhorukov, A. Kornowski, H. Möhwald, M. Giersig, A. Eychmüller, and H. Weller, "Formation of luminescent spherical core-shell particles by the consecutive adsorption of polyelectrolyte and CdTe(S) nanocrystals on latex colloids," Coll. Surf. A **163**, 39 (2000).

[7] V. Sandoghdar, F. Treussart, J. Hare, V. Lefevre-Seguin, J. M. Raimond, and S. Haroche, "Very low threshold whispering-gallery-mode micro-sphere laser," Phys. Rev. A **54,** R1777 (1996).

[8] K. Miura, K. Tanaka, and K. Hirao, "CW laser oscillation on both the $^4F_{3/2} \rightarrow {}^4I_{11/2}$ and $^4F_{3/2} \rightarrow {}^4I_{13/2}$ transitions of Nd^{3+} ions using a fluoride glass microsphere," J. Non-Crystalline Solids **213**, 276 (1997).

[9] X. Peng, F. Song, S. B. Jiang, N. Peyghambarian, M. Kuwata-Gonokami, and L. Xu, "Fiber-taper-coopled L-band Er^{3+} -doped tellurite glass microsphere laser", Appl. Phys. Lett. **82**, 1497 (2003).

[10] W. v. Klitzing, E. Jahier, R. Long, F. Lissillour, V. Lefevre-Seguin, J. Hare, J. M. Raimond, and S. Haroche, "Very low threshold lasing in Er^{3+} doped ZBLAN microsphere", Electron. Lett. **35**, 1745 (1999).

[11] W. v. Klitzing, E. Jahier, R. Long, F. Lissillour, V. Lefevre-Seguin, J. Hare, J. M. Raimond, and S. Haroche, "Very low threshold green lasing in microspheres by up-conversion of IR photons", J. Opt. B **2**, 204 (2000).

[12] F. Lissillour, P. Feron, N. Dubreuil, P. Dupriez, M. Poulain, G. M. Stephan, "Erbium-doped microspherical lasers at 1.56 μm", Eletron. Lett. **36**, 1382 (2000).

[13] F. Lissillour, D. Messager, G. Stephan, and P. Ferron, "Whispering-gallery-mode laser at 1.56 μm excited by a fiber taper", Opt. Lett. **26**, 1051 (2001).

[14] H. Fujiwara, and K. Sasaki, "Microspherical lasing of an erbium-ion-doped glass particle", Jpn. J. Appl. Phys. II. **41**, L46 (2002).

[15] M. Cai, O. Painter, K. J. Vahala, and P. C. Sercel, "Fiber-coupled microsphere laser", Opt. Lett. **25**, 1430 (2000).

[16] K. Sasagawa, Z. Yonezawa, R. Iwai, J. Ohta, and M. Nunoshita, "S-band Tm^{3+} - doped tellurite glass microsphere laser via a cascade process", Appl. Phys. Lett. **85**, 4325 (2004).

[17] L. Yang, and K. J. Vahala, "Gain functionalization of silica microresonators", Opt. Lett. **28**, 592 (2003).

[18] U. Woggon, R. Wannemacher, M. V. Artemyev, B. Moeller, N. LeThomas, V. Anikeyev, and O. Schoeps, "Dot-in-a-dot: electronic and photonic confinement in all three dimensions", Appl. Phys. B: Lasers and Optics, **77**, 469 (2003).

[19] B. Moeller, M. V. Artemyev, and U. Woggon, "Mode identification in spherical microcavities doped with quantum dots", Appl. Phys. Lett. **80**, 3253 (2002).

[20] X. Fan, M. C. Lonergan, Y. Zhang, and H. Wang, "Enhanced spontaneous emission from semiconductor nanocrystals embedded in whispering gallery optical microcavities", Phys. Rev. B **64**, 115310 (2001).

[21] S. I. Shopova, G. Farca, A. T. Rosenberg, W. M. S. Wickramanayake, and N. A. Kotov, "Microsphere whispering-gallery-mode laser using HgTe quantum dots", Appl. Phys. Lett. **85**, 6101 (2004).

[22] S. Lu, D. Jiang, R. Jia, L. An, L. Bian, X. Liang, B. Ma, and B. Sun, "Lasing of CdSexS1-x quantum dots in a glass spherical microcavity", J. Phys.: Condens. Matter **14**, 6395 (2002).

[23] V. S. Ilchenko, P. S. Volikov, V. L. Velichansky, F. Treussart, V. Lefevre-Seguin, J.-M. Raimond, and S. Haroche, "Strain-tuned high-Q optical microsphere resonators", Opt. Commun. **145**, 86 (1998).

[24] W. v. Klitzing, R. Long, V. S. Ilchenko, J. Hare, and V. Lefevre-Seguin, "Tunable whispering gallery modes for spectroscopy and CQED experiments", New. J. Phys. **3**, (2001).

[25] W. v. Klitzing, R. Long, V. S. Ilchenko, J. Hare, and V. Lefevre-Seguin, "Frequency tuning of the whispering-gallery modes of silica microspheres for cavity quantum electrodynamics and spectroscopy", Opt. Lett. **26**, 166 (2001).

[26] G. Chen, R. K. Chang, S. C. Hill, and P. W. Barber, "Frequency splitting of degenerate spherical cavity modes: stimulated Raman scattering spectrum of deformed droplets", Opt. Lett. **16**, 1269 (1991).

[27] A. J. Trevitt, and P. J. Wearne, "Observation of nondegenerate cavity modes for a distorted polystyrene microsphere" Opt. Lett. **31**, 2211 (2006).

[28] H. C. Tapalian, J. P. Laine, and P. A. Lane, "Thermooptical switches using coated microsphere resonators", IEEE Photon. Technol. Lett. **14**, 1118 (2002).

[29] A. Ashkin, "Acceleration and trapping of particles by radiation pressure", Phys. Rev. Lett. **24**, 156 (1970).

[30] A. Ashkin, "Optical trapping and manipulation of neutral particles using lasers", Proc. Natl. Acad. Sci. **94**, 4853 (1997).

[31] K. C. Neuman, and S. M. Block, "Optical trapping", Rev. Sci. Instrum. **75**, 2787 (2004).

[32] J. Z. Zhang and R. K. Chang, Opt. Lett. **13**, 916 (1988).

[33] H. M. Lai, P. T. Leung, K. L. Poon, and K. Young, J. Opt. Soc. Am. B **6**, 2430 (1989).

[34] J. M. Hartings, X. Pu, J. L. Cheung, and R. K. Chang, J. Opt. Soc. Am. B **14**, 2842 (1997).

Chapter 2

Active nanocrystal-coated microsphere-emitter

2.1 Introduction

The novel nanocrystal-microcavity system whose optical and mechanical properties are studied in this thesis, consist of a transparent dielectric microsphere which is coated with a monolayer of CdTe colloidal nanocrystals. Either polystyrene (PS) or melamine formaldehyde latex (MF) microspheres where used as our samples. The microspheres were purchased from microParticles GmbH in Berlin, Germany. The microspheres offer high optical transparency and thermal and mechanical stability which are optimal features for a spherical microcavity resonator. MF microspheres have a particularly high refractive index of $n_{MF} = 1.68$ compared with silica ($n = 1.47$), ensuring optimal confinement of the light within the microsphere. Colloidal nanocrystals are potential candidates for novel light emitting devices, as they show unique chemical and optical properties. With the tunable emission properties, they possess strong potential as quantum dot laser structures [1], LEDs [2], and in biological labelling [3]. The microsphere is a highly uniform microcavity, which provides exceptionally high Q-factors and photon storage lifetimes. The mode volume is very small, which causes very high electromagnetic field intensities in the microsphere. However, the electromagnetic wave is not fully confined to the inside of the sphere. At the boundary, where the light is totally reflected, an evanescent electromagnetic field propagates outside to a distance on the order of a micrometer. The CdTe nanocrystals on the surface of the microsphere are placed within the evanescent field originated from the optical resonances within the sphere. This causes strong interaction between the confined electromagnetic field of the microcavity and the electronic recombination process in the nanocrystals. In order to coat the microspheres with a monolayer of CdTe

nanocrystals, PE multilayers are first deposited on the sphere surface to enhance the electrostatic force, which bonds the nanocrystals to the sphere. The PE multilayers are tuneable to any desired thickness by simply adding the required number of layers.

In this chapter, fundamental information about the two components of the composite system, the nanocrystals and the spherical microcavity, is presented. In the first section, a short description of colloidal nanocrystals and the manufacturing process used to produce them is given. The second and third sections provides the theory and background knowledge about the optical resonances in a spherical microcavity and a summary of the Mie-scattering theory for calculating the resonance spectrum. The optical characteristics and a novel approach to achieve controlled lifting of the azimuthal mode degeneracy are presented in the following chapters of this thesis.

2.2 Colloidal CdTe nanocrystals

CdTe is a II-VI composite semiconductor material with a direct bandgap of *1.56 eV* ($\Delta\lambda$ = *795 nm*) at *300 K* in bulk material. Photostable colloidal nanocrystals are synthesized in an aqueous solution and capped with a stabilizer agent. The emission wavelength is highly size-dependent, due to the confinement of the electronic states in the nanocrystal in all three dimensions. The result is a zero dimensional quantum box where the continuous conduction band known from bulk semiconductor material develops into discrete energy states with highly size-dependent transition energy levels. Colloidal nanocrystals also possess high quantum efficiency at room temperature. Our samples reach a quantum efficiency of about $\eta_{eff} \approx 25\%$. The absorption and PL spectrum for colloidal CdTe nanocrystals in an aqueous solution is shown in Fig. 1. The size of the nanocrystals is around *4.8 nm* with a PL maximum at around *630 nm* wavelength. The absorption graph (black curve) clearly shows the peak of the first electronic transition in the nanocrystals. The emission maximum is located near the absorption threshold. The strong electronic confinement in the nanocrystals induces a blue shift of the absorption peak by almost *610 meV* with respect to bulk CdTe. The linewidth of the emission peak is characterised by the spectral inhomogeneous broadening caused by the size distribution of the colloidal nanocrystals in solution. Due to the high number of quantum dots in a sample, the natural

or homogeneous broadening of the electronic transition linewidth is considerably smaller than the inhomogeneous broadening effect and therefore, not visible in the spectrum. Thioglycolic acid (TGA) capped CdTe nanocrystals are synthesised as described in [4]. In a typical synthesis process, $Cd(ClO_4)_2$ is mixed with the capping agent, the thioglycolic acid, in an aqueous solution. H_2Te gas is formed by the reaction of Al_2Te_3 with H_2SO_4 in a nitrogen atmosphere in a separate flask. The gas is passed through the solution together with nitrogen. A CdTe nanocrystal precursor develops in the solution. In the next step, the CdTe nanocrystals slowly grow under heating (*100 ℃*) and open air conditions. The size of the nanocrystals is monitored by absorption and PL measurements of a sample taken from the solution. The smallest producible size is around

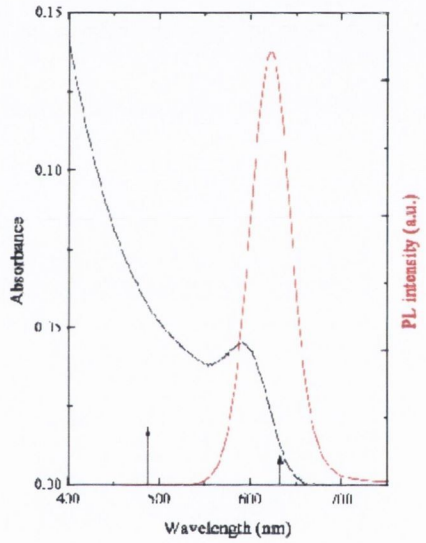

Figure 1. *Absorption and photoluminescence spectrum of CdTe nanocrystals in aqueous solution.*

2 nm with an emission peak at a wavelength of $\lambda = 520\ nm$. The largest nanocrystals are about *6 nm* in diameter, which corresponds to a PL maximum at $\lambda = 730\ nm$. The strongly size-dependent photoluminescence of the CdTe nanocrystals for nanocrystals from *2 nm* to *5 nm* is indicated in the schematic graph in Fig. 2. The thioglycolic acid capped CdTe nanocrystals are slightly negatively charged due to the –OH and –SH groups on the surface. This makes them ideal candidates for deposition on differently charged material surfaces by electrostatic attraction. The nanocrystals show an extreme high stability of up to several years when stored in a dark place at room temperature. The optical properties do

not change during the storage time. When irradiated, the photostability of the nanocrystals is very high when kept under vacuum condition. Under these conditions, they possess sufficient stability for light-emitting device applications [2].

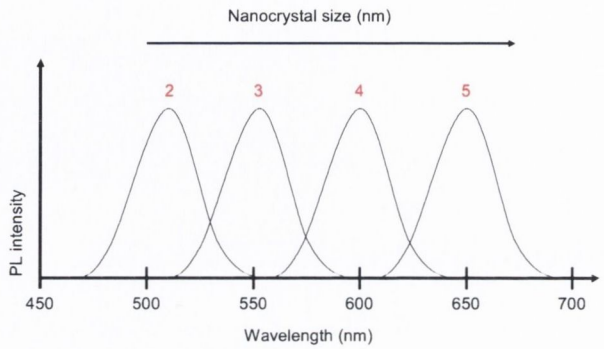

Figure 2. *Size-dependent luminescence of colloidal thioglycolic acid capped CdTe nanocrystals.*

2.3 Resonances (Whispering Gallery Modes) in spherical microcavities

At the beginning of the last century, Lord Rayleigh studied the propagation of acoustic waves along a curved gallery, which he called a whispering gallery [5]. A whisper near the gallery walls was still clearly heard at the other end of the structure, as the sound travels along the wall near the surface. Today in optics, the electromagnetic resonances inside a microsphere, which occur only at discrete wavelengths, are also called whispering gallery modes. Light, which is coupled into the sphere, travels around the circumference close to the surface, as a result of total internal reflection at the boundary of the sphere surface and the surrounding medium. The light, trapped in a spherical resonator, give rise to optical resonances. Calculations based on Maxwell's equations allow the exact identification of the resonance frequencies. Fundamental work with regard to these calculations was carried

out by G. Mie in 1908, in which he developed equations to determine the scattering field of a plane electromagnetic wave from a spherical particle [6]. Apart from the circular trajectory, the light also travels around the sphere with different inclination angles with respect to the equatorial plane, which characterises the azimuthal dependency of a resonance mode. The modes are characterised by three mode numbers [7] similar to the three quantum numbers in an atom, which describe the energy states of an electron. In a sphere, the modes are characterised by the radial mode number n, the angular mode number ℓ and the azimuthal mode number m. The angular mode number ℓ is close to the number of wavelengths which fit around the circumference of the microsphere. The value of $\ell - |m| + 1$ is equal to the number of field maxima in the polar direction. The radial mode number n specifies the number of field maxima in the radial direction. The negative or positive value of m show that light the can travel inside the sphere in either clockwise or anti-clockwise direction. The different values of m characterise the inclination angles of the resonances with respect to the equatorial plane. The characteristics of the azimuthal modes are discussed in chapter 5.4 in more detail with regard to deformed microspheres. The other factor which defines the characteristics of WGMs is the polarisation. There are two possible polarisation states, the transverse-electric (TE_ℓ^n) and the transverse-magnetic (TM_ℓ^n) mode. These modes have an electric and a magnetic field vector which is normal to the direction of propagation. In case of TE-modes, the electric field vector is perpendicular to the equatorial plane of the sphere and in case of TM-modes, the magnetic field vector is perpendicular to the equatorial plane. The existence of TE and TM polarised modes in a microsphere is the result of the required continuity of the tangential electric and magnetic fields at the interface of the dielectric and the surrounding medium. The different phase shift of TE and TM polarised light upon reflection at the interface results in a frequency shift and thus, in a spectral separation of TE and TM modes with the same mode numbers. The calculation of the whispering-gallery modes was carried out by G. Mie in 1908 for the first time [6]. The WGM-spectrum of a microsphere can be computed from the Maxwell equations with appropriate boundary conditions as discussed in section 2.4.

As an optical resonator, microspheres offer the unique property of a very high Q-factor. The Q-factor characterises the energy storage capability of the sphere with respect to the power dissipation due to internal and external losses such as attenuation, leakage, scattering and coupling. The quality factor is given by

$$Q = \frac{f}{\Delta f_{FWHM}} = \frac{\lambda}{\Delta \lambda_{FWHM}} = \omega \cdot \tau \tag{2.1}$$

in which f is the frequency of a particular whispering gallery mode, Δf_{FWHM} is the linewidth of the cavity mode, λ the corresponding wavelength of the mode, $\Delta\lambda_{FWHM}$ the linewidth and τ the 1/e-photon lifetime. The Q-factor is determined by the following factors [8, 9]

$$Q^{-1} = Q_{rad}^{-1} + Q_{surf}^{-1} + Q_{mat}^{-1}. \tag{2.2}$$

Q_{rad} are the intrinsic radiative losses due to a finite D/λ-ratio. When the diameter D of the sphere decreases, and accordingly the curvature of the sphere surface increases, higher radiative losses occur in the sphere. Q_{surf} describes the surface scattering losses of the light while travelling along the rim of the sphere. The losses such as attenuation, caused by the material of the sphere is characterised by Q_{mat}. In larger spheres with diameter $D \gg 100\ \mu m$, the Q-factor is limited by the material losses. In case of small spheres, the radiative losses are the limiting value for the Q-factor. In practice, Q-factors up to 10^{10} can be obtained [8] in large spheres. The high-Q characteristic is ideal for potential applications of microsphere laser or optical filters with very narrow bandwidth in the sub-nanometer range. The work in this thesis is based on the optical characterization of spheres with a diameter of $70\ \mu m$ and small microspheres with a diameter of $3\ \mu m$. The next section provides a discussion of the theoretical background of the Mie-scattering calculations which was necessary to identify the modes in the measured spectra. We also used approximations for analytical calculations of the resonances and for calculations analysing the lifted azimuthal mode degeneracy as discussed in chapter 5.

2.4 Calculations of the Mie-scattering coefficients

The scattering and absorption of light by a small spherical particle with arbitrary size and refractive index is not simple to describe in a physical manner, although the mathematical characterisation is straightforward but complex. Gustav Mie developed a theory to calculate absorption and scattering of a plane wave by spheres, which was published in 1908 [6]. Maxwell's equations are the theoretical background for describing the electric and magnetic field in a homogeneous dielectric sphere without free electric charge. In the following, the strategy for the Mie theory calculation of the electromagnetic field is briefly outlined. Propagation of electromagnetic waves in a medium which is uniform, isotropic, dielectric and charge free is considered. These conditions reduce the initial Maxwell equations to two standard equations for wave propagation in the dielectric medium. The next step is to seek solutions for the wave equations with the boundary conditions that the tangential components of the electric and magnetic field is continuous across the spherical surface. The wave equations are re-written in spherical coordinates and the fields inside and outside the sphere are expressed in vector spherical harmonic expansions. The boundary conditions to match the tangential fields are applied to obtain the scattered spherical wave Mie coefficients a_n and b_n. To find solutions for this vector wave equation the scalar equation, which is the well-known Helmholtz equation will be solved in spherical polar coordinates. The Helmholtz wave equation is given by

$$\nabla^2\Psi + k^2\Psi = 0, \tag{2.3}$$

which is described in spherical polar coordinates as

$$\frac{1}{r^2}\frac{\partial}{\partial r}\left(r^2\frac{\partial\Psi}{\partial r}\right) + \frac{1}{r^2\sin\theta}\frac{\partial}{\partial\theta}\left(\sin\theta\frac{\partial\psi}{\partial\theta}\right) + \frac{1}{r^2\sin\theta}\frac{\partial^2\psi}{\partial\phi^2} + k^2\psi = 0. \tag{2.4}$$

ψ is a scalar wave function which gives the particular solutions for the wave equation. The wave number is given by $k=2\pi/\lambda$, the spherical polar coordinates are the distance r from the centre of the sphere, the azimuthal angle θ and the polar angle ϕ. The separation of variables approach is used to obtain particular solutions. The general solution for the Helmholtz equation is

$$\psi = \frac{1}{\sqrt{kr}} Z_l(kr) Y_l^m(\theta,\phi). \tag{2.5}$$

The Bessel function Z is used depending on the boundary conditions, Y is the spherical harmonic. The spherical harmonics are expressed as Bessel functions $J_n(x)$ for finite values at the origin, Neumann functions $N_n(x)$ for vanishing at infinity and Hankel functions for travelling waves. To derive the scattering coefficients a_n and b_n, it is necessary to apply the boundary conditions for the transverse electric and transverse magnetic field at the sphere surface. That means, that the inner and outer transverse fields must match at the intersection between the sphere medium and the surrounding medium, which results in the following 4 equations

$$\begin{aligned} E_{i\theta} + E_{s\theta} = E_{l\theta}, E_{i\phi} + E_{s\phi} = E_{l\phi} \\ H_{i\theta} + H_{s\theta} = H_{l\theta}, H_{i\phi} + H_{s\phi} = H_{l\phi} \end{aligned} \tag{2.6}$$

plus the condition $r = a$ where a is the radius of the sphere. With these boundary conditions, the Mie coefficients are derived by using expansion formulae for the incident fields E_i and H_i, the scattering fields E_s and H_s, and the internal fields E_l and H_l [10]. The boundary conditions are then expressed in the 4 equations

$$\begin{aligned} & j_n(mx)c_n + h_n^{(l)}(x)b_n = j_n(x), \\ & [mxj_n(mx)]'c_n + [xh_n^{(l)}(x)]'b_n = [xj_n(x)]', \\ & mj_n(mx)d_n + h_n^{(l)}(x)a_n = j_n(x), \\ & [mxj_n(mx)]'d_n + m[xh_n^{(l)}(x)]'a_n = m[xj_n(x)]', \end{aligned} \tag{2.7}$$

where x is the size parameter and m the relative refractive index. Solving the equations for the Mie coefficients results in the Mie scattering coefficients a_n and b_n and the coefficients for the field inside the sphere (c_n and d_n)

$$\begin{aligned} a_n &= \frac{m^2 j_n(mx)[xh_n^{(1)}(x)]' - h_n^{(1)}(x)[xj_n(x)]'}{m^2 j_n(mx)[xh_n^{(1)}(x)]' - h_n^{(1)}(x)[mxj_n(mx)]'}, \\ b_n &= \frac{j_n(mx)[xj_n(x)]' - j_n(x)[mxj_n(mx)]'}{j_n(mx)[xh_n^{(1)}(x)]' - h_n^{(1)}(x)[mxj_n(mx)]'}, \end{aligned} \tag{2.8}$$

$$\begin{aligned} c_n &= \frac{j_n(x)[xh_n^{(1)}(x)]' - h_n^{(1)}(x)[xj_n(x)]'}{j_n(mx)[xh_n^{(1)}(x)]' - h_n^{(1)}(x)[mxj_n(mx)]'}, \\ d_n &= \frac{mj_n(x)[xh_n^{(1)}(x)]' - mh_n^{(1)}(x)[xj_n(x)]'}{m^2 j_n(mx)[xh_n^{(1)}(x)]' - h_n^{(1)}(x)[mxj_n(mx)]'}. \end{aligned}$$

The resonances appear in the spectrum when the denominator approaches zero. Therefore, the conditions for a_n and b_n are

$$\frac{[xh_n^{(1)}(x)]'}{h_n^{(1)}(x)} = \frac{[mxj_n(mx)]'}{m^2 j_n(mx)} \tag{2.9}$$

and

$$\frac{[xh_n^{(1)}(x)]'}{h_n^{(1)}(x)} = \frac{[mxj_n(mx)]'}{j_n(mx)}, \tag{2.10}$$

respectively. These two transcendental equations are satisfied for an infinite number of particular size parameter $x_{n,l}$ which correspond to the wavelengths of the optical resonances in the sphere, each for the radial l^{th} root for each angular mode with the angular mode number n. In the next step, the transcendental equations are simplified by applying the Riccati-Bessel functions

$$\begin{aligned} \psi_n(x) &= xj_n(x), \\ \xi_n(x) &= xh_n^1(x). \end{aligned} \tag{2.11}$$

Finally, the Lorentz-Mie scattering coefficients are given by

$$a_n = \frac{m\psi_n(mx)\psi_n'(x) - \psi_n(x)\psi_n'(mx)}{m\psi_n(mx)\xi_n'(x) - \xi_n(x)\psi_n'(mx)},$$
$$b_n = \frac{\psi_n(mx)\psi_n'(x) - m\psi_n(x)\psi_n'(mx)}{\psi_n(mx)\xi_n'(x) - m\xi_n(x)\psi_n'(mx)}. \tag{2.12}$$

According to the Lorentz-Mie theory, the extinction cross-section is given by

$$C_{ext} = \frac{2\pi}{k_1^2}\mathrm{Re}\sum_{n=1}^{\infty}(2n+1)(b_n + a_n) \tag{2.13}$$

and the scattering cross-section by the following equation

$$C_{sca} = \frac{2\pi}{k_1^2}\sum_{n=1}^{\infty}(2n+1)\left(|b_n|^2 + |a_n|^2\right), \tag{2.14}$$

where n is the radial mode number and k_1 is the wave number in the surrounding region. The variables k_1 and ω *are*

$$k_1 = \omega\sqrt{\varepsilon_1\mu_0} \qquad \omega = \frac{2\pi c}{\lambda}. \tag{2.15}$$

Due to energy conservation, the absorption cross-section C_{abs} is

$$C_{abs} = C_{ext} - C_{sca}. \tag{2.16}$$

The frequently used efficiencies Q_{ext}, Q_{sca} and Q_{abs} are the cross-sections C normalised to the particle cross-section,

$$Q = \frac{C}{\pi a^2}. \tag{2.17}$$

The variable a is the particle radius. The radiation pressure efficiency is expressed by

$$Q_{pr} = Q_{ext} - Q_{sca}\langle\cos\theta\rangle. \tag{2.18}$$

The parameter $\langle \cos\theta \rangle$ is the average cosine of the scattering angle θ. Radiation pressure and the calculations for our experimental configuration are discussed in more detail in chapter 5.2. Based on the scattering coefficients in Eq. 2.12, we identified TE and TM modes in the PL spectrum of the small microspheres.

References

[1] S. I. Shopova, G. Farca, A. T. Rosenberger, W. M. S. Wickramanayake, and N. A. Kotov, "Microsphere whispering-gallery-mode laser using HgTe quantum dots", Appl. Phys. Lett. **85**, 6101 (2004).

[2] Nir Tessler, Vlad Medvedev, Miri Kazes, ShiHai Kan, and Uri Banin, "Efficient Near-Infrared Polymer Nanocrystal Light-Emitting Diodes", Science **295,** 1506 (2002).

[3] X. Michalet, F. F. Pinaud, L. A. Bentolila, J. M. Tsay, S. Doose, J. J. Li, G. Sundaresan, A. M. Wu, S. S. Gambhir, and S. Weiss, "Quantum Dots for Live Cells, in Vivo Imaging, and Diagnostics", Science **307**, 538 (2005).

[4] N. Gaponik, D. V. Talapin, A. L. Rogach, K. Hoppe, E. V. Shevchenko, A. Kornowski, A. Eychemueller, and H. Weller, "Thiol-capping of CdTe nanocrystals: An alternative to organometallic synthetic routes", J. Phys. Chem. B. **106**, 7177 (2002).

[5] Lord Rayleigh, "The problem of the whispering gallery", Scientific papers **5**, 617 (1912).

[6] G. Mie, "Beitraege zur Optik ueber Medien", Ann. Phys. **25,** 377 (1908).

[7] B. E. Little, J.-P. Laine, and H. A. Haus, J. Lightwave Technol. **17**, 704 (1999).

[8] M. L. Gorodetsky, A. A. Savchenkov, and V. S. Ilchenko, "Ultimate Q of optical microsphere resonators", Opt. Lett. **21**, 453 (1996).

[9] V. B. Braginsky, M. L. Gorodetsky, and V. S. Ilchenko, "Quality-factor and nonlinear properties of optical whispering-gallery modes", Phys. Rev. A **137**, 393 (1989).

[10] Bohren, C.F., and D.R. Huffman, "Absorption and Scattering of Light by Small Particles", Wiley-Interscience, New York (1983).

Chapter 3

Sample preparation and experimental methods

3.1 Introduction

In this chapter, the experimental equipment and the method which was employed to carry out the micro-Raman and micro-photoluminescence measurements is discussed. The sample preparation which consists of coating the microspheres with PE multilayers and a monolayer of CdTe nanocrystals as well as the softening process of the PE layer is also described. The commercial micro-Raman/micro-PL machine provided a setup with high spatial resolution, high spectral resolution and high sensitivity which was necessary to carry out the radiation pressure experiments. In this chapter, the fabrication process of the composite nanocrystal-microcavity system into an optically pumped active microsphere-emitter is outlined. Prior to the nanocrystal layer, the sphere must be coated with PE multilayers. The so called layer-by-layer self-assembly technique is based on electrostatic attraction between two oppositely charged polyelectrolytes. The melamine formaldehyde (MF) microsphere coated in our lab is slightly positively charged. The electrostatic force of the uncoated spheres is not sufficient to attach a nanocrystal layer on the surface. The polyelectrolytes applied in this coating are Poly(allylamine hydrochloride) (PAH) which is positively charged and poly(sodium 4-styrenesulfonate) (PSS) which is negatively charged. The thioglycolic acid capped CdTe nanocrystals have a negative surface charge. The layers are alternately deposited on the sphere surface. The thickness of one PE layer is approximately *1.5 nm* [1]. Theoretically, any desired thickness of the PE multilayers can be built up by applying new layers step by step. As the top layer always requires the opposite charge of the nanocrystals for electrostatic attraction, the layers have to be build up in pairs of PSS/PAH bi-layers. When the desired thickness is reached, the nanocrystal

monolayer is deposited on top of the PE multilayers, also due to the electrostatic force. The nanocrystals form a closed packed dense monolayer of nanocrystals by self-assembly.

3.2 Layer-by-layer technique

The charged polyelectrolyte multilayer enhances the electrostatic attraction required for a dense and homogeneous coating of nanocrystals on the microsphere. The technique of assembling polyelectrolyte multilayers on a sphere surface was already successfully carried out several years ago [2-4]. This so called layer-by-layer technique (LbL) is a convenient and simple method to deposit a layer of charged colloidal particles such as nanocrystals or metallic particles on a sphere surface. The sulfonate group $-SO_3^-$ of PSS results in a negative charge and the ammonia group $-NH_3^+$ charges PAH positive (see Fig. 1). The MF microsphere surface is positively charged, while the thioglycolic capped CdTe nanocrystals possess a slightly negatively surface charge. The negative charge is a result of the –OH and –SH groups of the capping agent thioglycolic acid.

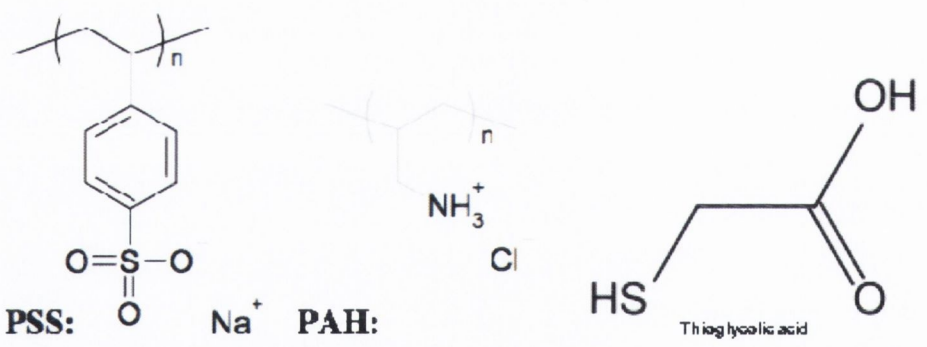

Figure 1. *Chemical composition of the polyelectrolytes used for the multilayers (PSS and PAH) and chemical formula for thioglycolic acid (capping agent of the colloidal CdTe nanocrystals).*

The process starts with the sequential deposition of the oppositely charged polyelectrolytes PAH and PSS. As the MF microsphere is positively charged, the first layer is negatively charged PSS. When the PSS layer is deposited, the sphere surface is negatively charged.

The next layer is positively charged PAH. Now the process continues with a PSS layer and so on until the required number of layers is attached to the sphere surface. The outer most PE layer has to be oppositely charged to the colloidal particles, here CdTe nanocrystals, for electrostatic bonding. At least 3 or 4 PE single layers are required for a homogeneous deposition of the nanocrystal layer [4]. The procedure for assembling the layers in the lab requires a centrifuge and a sonicate bath. The chemicals were prepared with deionized Millipore water with a resistivity higher than *18 MΩ/cm*. The microspheres were diluted in the particular polyelectrolyte solution, either PSS or PAH. The polyelectrolyte is adsorbed on the sphere surface by electrostatic interaction. The PE solution consists of an excess concentration to assure homogeneous covering of the surface. The spheres are coated with a new PE layer within 15 minutes exposed to the PE solution. To separate the coated spheres from the solution, the flask is centrifuged so that the spheres accumulate on the bottom of the centrifuge tube. The excess PE solution is then removed by tipping over the tube. The get rid of all PE material which is not adsorbed by the spheres, several washing steps are carried out. Therefore, the sphere are diluted in water, shaked in a sonicate bath and again separated from the water by centrifugation. After the washing steps, the spheres are diluted in the PE solution which will be used to form the next PE layer and so on. The preparation steps for the assembling of the PE multilayers as performed in the lab are sketched as follows.

Preparation protocol:

1. **PSS:** 100 mg PSS + 50 ml of 0.5 M NaCl
2. **PAH:** 100 mg PAH + 50 ml 0.5 M NaCl
3. Sonicate both solutions for 15 minutes
4. **NaCl:** Preparation 50 ml of 0.15 M NaCl
5. Take 0.5 ml concentrated sphere solution and add water (Millipore water) up to 5 ml volume
6. Shake and sonicate for 4 seconds
7. Repeat step 6 three times
8. **Applying PSS layer:**
9. Add 15 ml of PSS solution to the 5 ml sphere solution
10. Shake and sonicate for 4 seconds
11. Repeat step 9 three times

12. Leave it aside for 15 minutes for adsorption while shaking every few minutes
13. Centrifuge for 5 minutes at 1250 rpm
14. Take off the excess water by tipping over the flask so that only the spheres remain at the bottom
15. **Washing steps: 1 x NaCl + 2 x water**
16. **NaCl washing step:**
17. Add 15 ml of NaCl (0.15 M)
18. Shake and sonicate for 4 seconds; repeat 3 times
19. Centrifuge for 5 minutes at 1250 rpm
20. Take of excess water
21. **Water washing step:** (2 times)
22. Add 25 ml of water
23. Shake and sonicate for 4 seconds; repeat 3 times
24. Centrifuge for 5 minutes at 1250 rpm
25. Take off excess water
26. Repeat washing step 2 times
27. **Applying PAH layer:**
28. Add water to spheres up to 5 ml volume
29. Shake and sonicate for 4 seconds; repeat 3 times
30. Add 15 ml of PAH solution
31. Shake and sonicate for 4 seconds; repeat 3 times
32. Leave it aside for 15 minutes for adsorption while shaking every few minutes
33. Centrifuge 5 minutes at 1250 rpm
34. Take of excess water
35. **Washing steps: 1 x NaCl + 2 x water (as described from point 15)**
36. **Continue alternately with PSS and PAH layer (point 8)**
37. **After last PE layer, 1 NaCl washing step and 4 water washing steps are applied**
38. Coated spheres are stored in water (filled up to 5 ml volume)

The process can be discontinued after any washing step and the spheres can be kept in water over night. The procedure has to be started with a water-washing step before continuing the process. After the PE multi-layer is applied to the sphere surface, the sphere

is coated with the CdTe nanocrystals. The very last topmost PE layer must have the opposite charge of the nanocrystals to ensure electrostatic attraction to the microsphere. The topmost layer for thioglycolic acid capped CdTe is PAH. The following steps are used to deposit the nanocrystals on the sphere surface:

1. 250 µl of sphere solution is taken and 200 µl of CdTe solution is added (in 1.5 ml Eppendorf flask)
2. **Sonicate step:** Shake and sonicate for 4 seconds; repeat 3 times
3. Shake for 1 hour with shaker (800 1/min), sonicate step every 10 minutes
4. Fill up Eppendorf flask with water (1.5 ml)
5. Centrifuge for 1 minute with fast centrifuge
6. Remove 1ml of solution with pipette
7. Fill up with water (1.5 ml)
8. Sonicate step
9. Centrifuge fast for 1 minute
10. Repeat from point 6 at least 4 times or until no nanocrystals are left in the solution
11. Store finished samples in water

The excess nanocrystals in solution have to be separated from the spheres very carefully (step 6). Therefore, a pipette is used to remove 1 ml of solution from the top of the flask, while the spheres are gathered at the bottom after centrifugation. This is achieved by tilting the flask by approximately *45°* and pipetting a few millimetres below the solution surface. After that, the flask is filled up with water and the samples are sonicated and centrifuged again. The flask was put under a UV lamp to monitor the cleaning steps. It is repeated until there is no visible luminescence in the solution left but only from the coated microspheres at the bottom of the flask.

3.3 Chemical softening of the PE multilayer

The novel experimental approach discussed in chapter 5 required a soft elastic shell on the sphere surface. In theory, a wide range of polymers can be used for deposition of a multilayer on the dielectric particle. The materials also vary in elastic strength. PSS/PAH multilayers are very well studied and applicable for deposition with a nanocrystal layer on top. Instead of searching for a new soft polymer, the decision was taken to additionally soften the PSS/PAH multilayer with a chemical procedure. We applied the treatment for reducing the stiffness of the PE multilayer in some of our samples as discussed in [5]. In this work, hollow and MF-core multilayered PSS/PAH capsules are studied in regards to their physical stiffness. According to these authors, the elasticity for a PE multilayer, expressed by the Young's modulus is on the order of *100-200 MPa*, while another publication [6] determined a maximum value of *100 MPa* and a presumable range of *70-100 MPa*. Exposing the multilayers to NaCl induces a change in the mechanical properties of the PE layer. The elasticity of PE capsules varies depending on a change of salt concentration. The authors in [5] and [6] explain the softening of the PE multilayers by a reduction of the ionic bonds between the layers. At salt concentrations above *3 mol/L*, the reduction of solidity appears to remain constant. According to [6], the salt softens the PE multilayers noticeably, although the Young's modulus remains in the same order of the untreated PE multilayers. It is determined to have a value of about *40-80 MPa*. To apply the treatment to our microsphere-emitter, the preparation procedure for the samples was changed. An additional step was necessary after the spheres were coated with the PE multilayers and before the nanocrystals were deposited on the sphere. A small amount of sphere solution, containing blank microspheres only coated with the PE multilayers was taken and a highly concentrated NaCl solution (*7 mol/l*) was added to the spheres. The spheres were kept in this solution for 5 days. After that, several water-washing steps were carried out, similar to the steps in the previous section.

1. Centrifuge for 1 minute with fast centrifuge

2. Remove 1 ml of solution with pipette
3. Fill up with water (1.5 ml)
4. Sonicate step
5. Centrifuge fast for 1 minute
6. Repeat from point 2 for at least 5 times

The NaCl solution is now separated from the samples and the spheres are kept in pure water for further processing. The procedure is now continued as described in the previous section with the coating of CdTe nanocrystals. It is worth mentioning that the procedure does not cause any problems with regards to the deposition process of the CdTe nanocrystals. The nanocrystal monolayer was applied to the softened PE multilayers without any difficulty. Furthermore, no quenching in photoluminescence from the nanocrystals or any enhanced photobleaching was observed in the measurements carried out with the new samples compared to untreated samples. In contrast, during the measurements, the samples appeared to be more stable than the samples without the salt treatment. Unfortunately no further measurements could be made yet to verify this observation. A potential process which increases the photostability is the weakening of photo-oxidation due to neutralisation of the nanocrystal surface charges by the salt ions of the highly concentrated solution. This is a very preliminary assumption which requires more experimental evidence for detailed studies.

3.4 Micro-photoluminenscence and micro-Raman setup

The experimental results in this thesis are mainly derived from the spectra of photoluminescence and Raman scattering from the CdTe nanocrystal-microcavity system. We applied a commercially available micro-Raman/micro-photoluminescence spectroscopy system from Renishaw for our measurements (*1800* mm^{-1} grating, *1* cm^{-1} resolution). The spectroscope is an enclosed system including all necessary components, apart from the excitation lasers which are coupled into the system by a free space entrance. The setup is enclosed by a dark chamber which blocks any stray light from outside. It is

equipped with a Leica optical microscope. The objective lens in the microscope illuminates the sample and collects the scattered light operating in a 180° backscatter geometry. The maximum magnification is achieved with a 100x microscope objective (Leitz, Germany) with a numerical aperture of $NA = 0.9$. The system is a confocal setup which blocks out-of-focus and off-axis light to detect the scattered light from only a limited sampling volume. The confocal optics is achieved by two apertures - one physical (the spectrograph entrance slit) and one defined in software (the height of the captured image on the CCD) to spatially filter the scattered light and give the required depth resolution. Using this approach, full confocal capability is achieved similar to a conventional pin-hole system. The system is shown in Fig. 2. The laser beam is coupled into the system and focused on a substrate holder, mounted on a microstage with high spatial resolution (*0.1 μm/step*) in all three directions. The sample is moved relative to the fixed microscope objective. The backscattered light is collected through the objective and guided to a CCD camera for selecting the samples under the microscope. During the measurement, the light is guided to the spectrometer. The notch plasma filter removes the Rayleigh scattering coming from the sample at the excitation wavelength. The spectrometer in combination with the CCD camera scans the spectrum of the collected light. Two lasers, coupled to the system as excitation sources, are an Ar^+-ion laser (λ = *488 nm, 457 nm or 514.5 nm, 45 mW* maximum output power) and a HeNe laser (λ = *632.8 nm, 20 mW*). Either one of the lasers is available for measurements at the same time, as the notch filter has to be changed in the system for each laser line. No angle-dependent detection of the scattered light is possible with this setup in standard configuration. The backscattered light is always collected

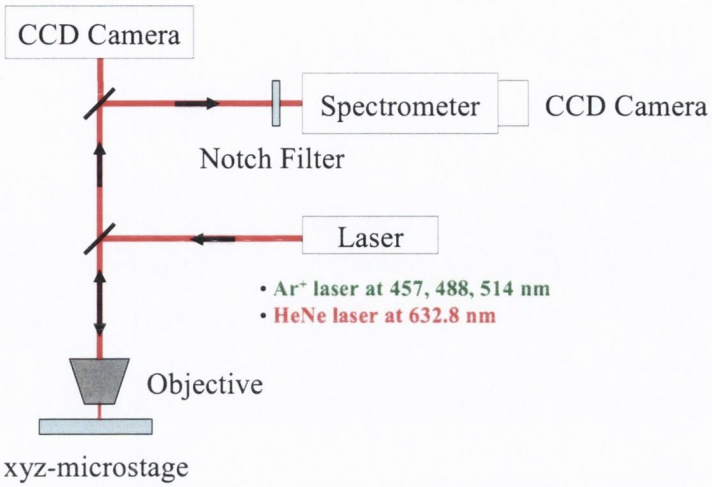

Figure 2. *Schematic of micro-PL/micro-Raman setup.*

perpendicular to the substrate. The machine is equipped with a ¼ waveplate to circularly polarise the laser beam and a ½ waveplate as an analyser for linear polarised light in the beam path of the collected backscattered light to discriminate between different polarisations of the detected signal. The CCD camera detector provides high sensitivity for the system. The variable integration time allows an increase of the signal to noise ratio. A variable mechanical slit installed in the beam path of the detected light in front of the spectrometer is used to tune the balance between the spectral resolution and the signal intensity. The measurements were carried out with this system by placing the substrate with the sphere-samples on the xyz-microstage. The samples were selected under white light through the CCD camera and the focus was set to the required position, either manually with an analog joystick and micrometer screws or computer-controlled by the software. When the sample is aligned, the laser shutter is opened and the measurement is started. The data is converted to ASCII for processing. This setup was used for all Raman and PL measurements throughout this thesis.

References

[1] F. Caruso, "Nanoengineering of Particle Surfaces", Adv. Mater. **13**, 11 (2001).

[2] F. Caruso, R. A. Caruso, and H. Moehwald, "Nanoengineering of inorganic and hybrid hollow spheres by colloidal templating", Science **282**, 1111 (1998).

[3] F. Caruso, H. Lichtenfeld, M. Giersing, and H. Moehwald, "Electrostatic self-assembly of silica nanoparticles-polyelectrolyte multilayers on polystyrene latex particles", J. Am. Chem. Soc. **120**, 8523 (1998).

[4] A. S. Susha, F. Caruso, A. L. Rogach, G. B. Sukhorukov, A. Kornowski, H. Moehwald, M. Giersig, A. Eychmueller, and H. Weller, "Formation of luminescent spherical core-shell paticles by the consecutive adsorption of polyelectrolyte and CdTe(S) nanocrystals on latex colloids", Coll. Surf. A: Physiochem. Eng. Aspects **163**, 39 (2000).

[5] O. V. Lebedeva, B. – S. Kim, K. Vasilev, and O. I. Vinogradova, "Salt softening of polyelectrolyte multilayer microcapsules," J. Colloid Interface Sci. **284**, 455–462 (2005).

[6] V. V. Lulevich, and O. I. Vinogradova, "Effect of pH and salt on the stiffness of polyelectrolyte multilayer microcapsules", Langmuir **20**, 2874 (2004).

Chapter 4

Raman scattering and photoluminescence from a composite nanocrystal-microcavity system

4.1 Introduction

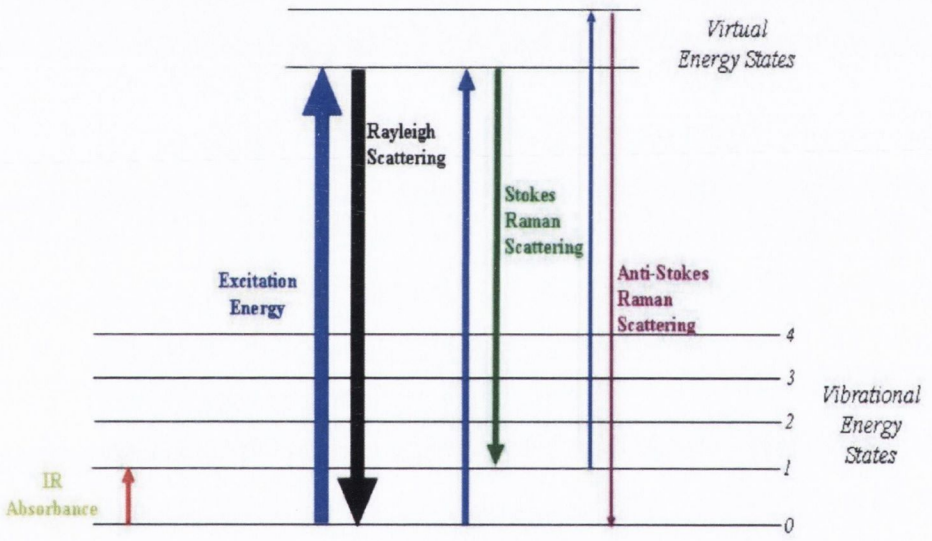

Figure 1. *Schematic illustration of Rayleigh scattering, Stokes and anti-Stokes Raman scattering.*

If a ray of light which is incident on an atom or molecule is not elastically scattered (Rayleigh scattering), an interaction between the photon and the molecules of the material occurs. When the scattered photon exchanges energy with the vibrational states of the molecules, the scattering is called Raman scattering. The incident photon can either gain or loose energy which induces a blue shift and a red shift in the wavelength spectrum, respectively. The energy is transferred as vibrational energy to and from the molecule,

appearing as modes in the spectrum of the scattered light. When the molecule is in the lowest energy state, the incident photon excites the molecule to a virtual energy state. The photon transfers energy to the molecule which is then excited to the first vibrational state. The scattered photon looses energy and experiences a red-shift. The mode appears as a Stokes line in the spectrum red-shifted relative to the excitation wavelength. In anti-Stokes Raman scattering, the molecule is already excited to a higher vibrational state. When the photon excites the molecule to the virtual state, the photon gains energy corresponding to the energy difference between the ground state and the first vibrational level and the molecule relaxes to the ground state. The scattered photon experiences a blue shift and a blue-shifted Raman mode appears in the spectrum. Raman excitation is normally far below the electronic transition level of the molecule, so that no electrons are excited into the electronic excited states. Real Raman peaks and luminescence peaks can be distinguished in this way.

In resonance Raman spectroscopy, the excitation energy is chosen so that the molecule is excited into the region of the electronic transition states. The result is a strong enhancement of the Raman scattering, comparable to Rayleigh scattering intensities. The Raman scattering is usually plotted as intensity versus the Raman shift in the unit of the wavenumbers cm^{-1}. The Raman modes are identified by the relative shift in relation to the excitation line. The Raman shift is therefore expressed independent of the excitation energy. The Raman spectrum is symmetric in the anti-Stokes and Stokes region relative to the excitation line. As Fig. 1 illustrates, the Raman scattered photon either gains or looses the same energy difference. Therefore, the Stokes region of the spectrum is sufficient for analysis of the spectrum. Both regions are only required for particular measurements. The intensities of the Raman modes in both regions depend on the populations of different vibrational energy states. In agreement with Boltzmann statistics, the population decreases at higher vibrational energy levels. The ratio of the populations in different energy levels is proportional to an exponential factor, depending on the energy gap and the temperature.

$$\frac{N_1}{N_0} \propto e^{-\frac{\Delta E}{kT}} \quad . \tag{4.1}$$

N_0 is the number of molecules in the lower energy state, N_1 the number of molecules in a higher vibrational energy state, ΔE the energy difference between the two levels, k the

Boltzmann constant and T the temperature. The ratio of $\frac{N_1}{N_2}$ becomes larger with increasing temperature T, as more molecules are excited to the higher vibration energy state. Anti-Stokes emission is highly temperature dependent as it requires the molecules in the higher vibrational state and therefore, the ratio of Stokes to anti-Stokes Raman emission intensities experiences a strong temperature dependency. The intensity ratio is expressed by [1]

$$\frac{I_{anti-Stokes}}{I_{Stokes}} = \frac{(\nu_0 + \nu)^4}{(\nu_0 - \nu)^4} e^{\left\{-\frac{hc\nu}{kT}\right\}} \quad , \tag{4.2}$$

where ν_0 and ν are the wavenumbers of the excitation line and the Raman mode, respectively. Consequently, the intensity of anti-Stokes modes is generally lower than the intensity of Stokes transitions at low temperatures, but with increasing temperature, these modes become observable in the Raman scattering spectrum.

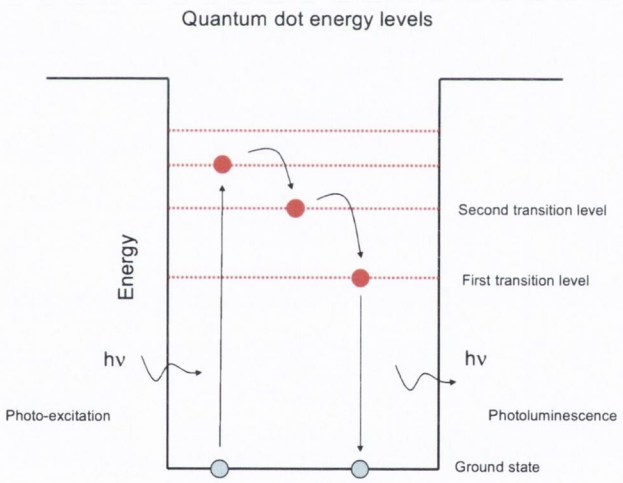

Figure 2. *Schematic of photo-excitation and photoluminescence in a quantum dot.*

Another form of interaction of light with matter is the radiative process called photoluminescence. A photon incident on a semiconductor material excites the electrons to a higher energy level. This process is called photo-excitation. In a nanocrystal or quantum dot, the electrons are excited to discrete energy levels. Radiative recombination within the

nanocrystals emits a photon. The principle process is shown in Fig. 2. An electron is excited from the ground state into a higher transition level by the incident photon. The energy of the emitted photon depends on the energy difference between the ground state and the first transition level. Non-radiative relaxation takes place between the higher transition levels. Electrons loose energy in the form of phonons during relaxation to the first energy level, while the radiative recombination process results in emission of a photon. The intensity of the photoluminescence is related to the quantum efficiency of the nanocrystals. Non-radiative recombination at defects on the surface and inside the nanocrystals reduces the efficiency of photon emission

As our sample is a composite of a dielectric resonator (melamine formaldehyde or polystyrene) and semiconductor CdTe nanocrystals on the sphere surface, our first experiments were aimed at the investigation of Raman scattering of the microsphere and the CdTe semiconductor material, respectively, as well as the photoluminescence from the CdTe nanocrystals. Our interest lies in the conditions under which we observe either Raman scattering or luminescence or both signals at the same time. Depending on the excitation energy and conditions, electronic and vibrational excitation is created in our nanocrystal-microcavity system. We first studied the interaction between the optical modes of the high-Q microcavity and the electronic states of the semiconductor nanocrystals by analyzing the photoluminescence emission spectrum in the Stokes and anti-Stokes region. The spectral analysis of the Raman scattering provides information about the efficiency of the high-Q microcavity photon emission enhancement due to coupling of electronic and vibrational energy states to the optical modes in the microcavity. Measurements were carried out under two different excitation conditions. Excitation of the nanocrystals was either induced off-resonance far below the first energy transition level of the nanocrystals with a HeNe laser ($\lambda = 632.8\ nm$) or on-resonance excitation above the first energy level with the $\lambda = 488\ nm$ line of the Ar^+- ion laser. The HeNe laser excitation was applied to detect Raman scattering from the samples and minimising photoluminescence, as excitation is below the first energy state of the nanocrystals. Exciting with the Ar^+- ion laser induces strong photoluminescence as the electrons are excited into the electronic states which dominates the Raman scattering in the spectrum. Varying the excitation conditions provides a method to observe Raman scattering and photoluminescence in the spectrum at the same time.

4.2 Enhanced Stokes and anti-Stokes emission

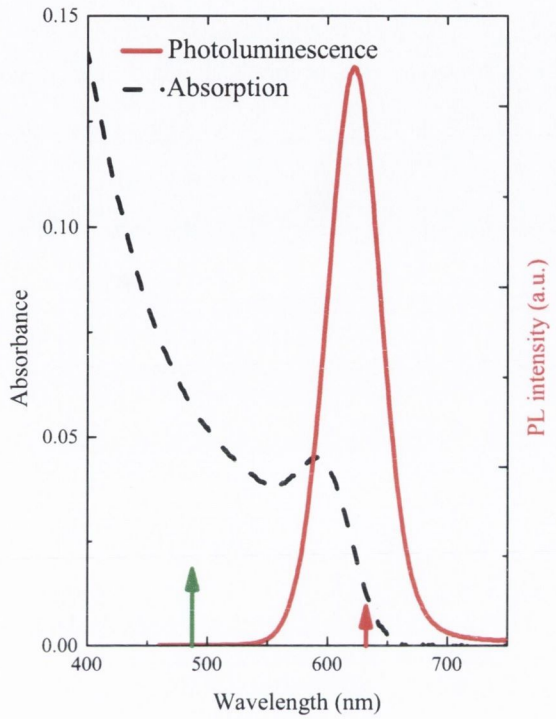

Figure 3. *Arrows indicate off-resonance (red arrow, HeNe laser at 632.8 nm) excitation and resonance (green arrow, Ar+-ion laser at 488 nm) excitation.*

In this series of measurements, the enhancement of photoluminescence and Raman scattering from the CdTe nanocrystals due to strong optical feedback in the microcavity was demonstrated. The samples were excited below the first electron transition state of the nanocrystals. The energy levels in nanocrystals are tuneable due to strong confinement in all three dimensions. That means that the bandgap and the separation between the energy levels increase with decreasing nanocrystals size. When the size is comparable to or smaller than the exciton Bohr radius, the electron-hole pairs cannot move freely in the bulk material anymore. The electron-hole pairs are spatially confined and discrete energy levels establish rather than a continuous energy band. The absorption measurement of colloidal

CdTe nanocrystals in an aqueous solution (see Fig. 3) clearly shows the first energy transition peak. The average dot size of the nanocrystals in this sample is about *4.8 nm*. The quantum efficiency at room temperature is about *25%*. The spectra were taken with a Shimadzu-3101 spectrophotometer and a Spex Fluorolog spectrofluorometer, respectively. The absorption peak is blue shifted by nearly *610 meV* with respect to bulk CdTe electronic transition level which proves the strong quantum confinement in the nanocrystals. The inhomogeneous broadening of the luminescence peak is due to the size distribution of the nanocrystals in the solution. The absorption graph (dashed line) shows the peak of the first electronic transition level. More light is absorbed with increasing photon energy, but higher energy levels cannot be distinguished in the curve. The red arrow indicates the off- resonance excitation wavelength with the HeNe laser, the green arrow points to the excitation wavelength of the Ar^+-ion laser. The sphere samples consist of polystyrene microspheres with a nominal diameter of *70 μm*.

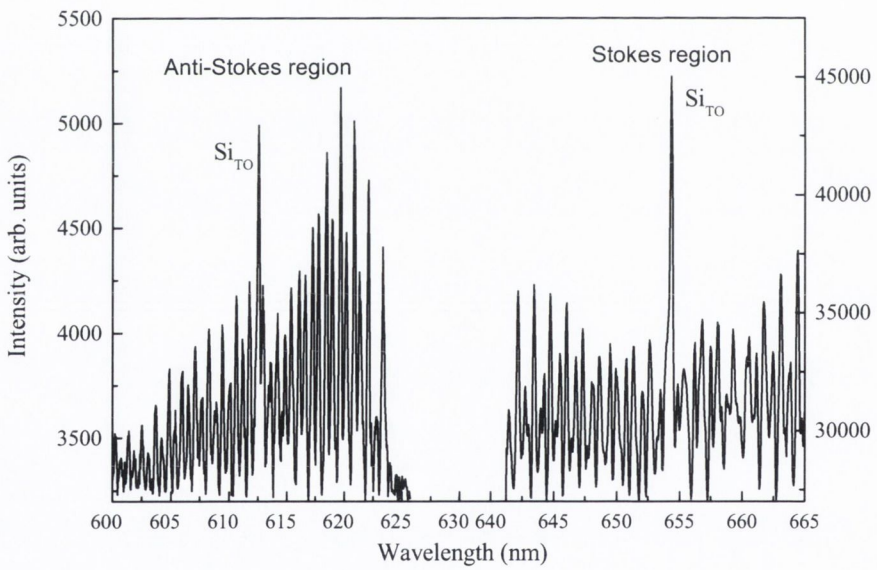

Figure 4. *Photoluminescence spectrum excited off-resonance with a HeNe laser at P = 3 mW output power.*

The spheres are coated with one monolayer of CdTe nanocrystals. A spectrum taken in the micro-Raman and photoluminescence setup excited with a HeNe laser below the absorption peak is shown in Fig. 4. The photoluminescence intensity is plotted against the wavelength. The background luminescence was subtracted in this graph for a better

presentation of the whispering gallery mode structure. The sample is placed on a Si-wafer substrate, the Si transverse-optical (TO) Raman mode is clearly visible in the spectrum in both the anti-Stokes and Stokes region. Nearly *100* resonance modes appear within the measured spectral range between *600 nm* and *665 nm*. The free spectral range between modes of the same polarization is less than *2 nm*. The gap in the centre is the region of the excitation laser, in this experiment, the *632.8 nm* line of the HeNe laser. To reduce Rayleigh scattered light from the excitation source to a minimum, a plasma notch filter is implemented in the setup. Excitation with the laser beam in this experiment also induces Raman scattering from the CdTe nanocrystals and the polystyrene sphere. However, the intensity of the Raman signal is very small in comparison with the luminescence from the excited nanocrystals, so that the Raman scattering in this measurement is masked by the photoluminescence of the nanocrystals. Although the excitation energy is below the energy gap of the first electronic transition state, only photoluminescence is observable in this measured spectrum. To emphasis this fact, the intensity is plotted versus the wavelength and not as a function of the Raman shift. In addition to that, remarkably high photoluminescence intensity above the excitation line corresponding to the anti-Stokes region in a Raman measurement is observed in this spectrum. Comparing the intensity scale of anti-Stokes PL emission on the left hand side of the graph with the scale on the right hand side for Stokes PL emission reveals that the anti-Stokes signal is only one order of magnitude below the intensity of the signal in the Stokes region. Such strong anti-Stokes excitation requires high quantum efficiency of the semiconductor nanocrystals [2, 3]. To explain the strong photoluminescence at excitation below the first electronic transition of the nanocrystals, we assume the existence of shallow trap level below the energy level of the first electronic state. Such trap level can be attributed to defect states on the surface of the nanocrystals. When the nanocrystals are excited with the HeNe laser, the electrons are excited to the trap levels. Recombination results in photoluminescence in the "Stokes region". As discussed in [4] and [5], the highly efficient emission in the "anti-Stokes" region is attributed to thermal re-excitation of the electrons into the first electronic transition state from where they recombine into the ground state. So the electrons are excited by two successive processes, the photo-excitation and the temperature-induced phonon energy transfer into the first transition state. The feedback of the optical signal inside the microcavity strongly increases the intensity of photoluminescence emitted from

the nanocrystals due to the enhanced coupling of the optical modes to the electronic states of the nanocrystals.

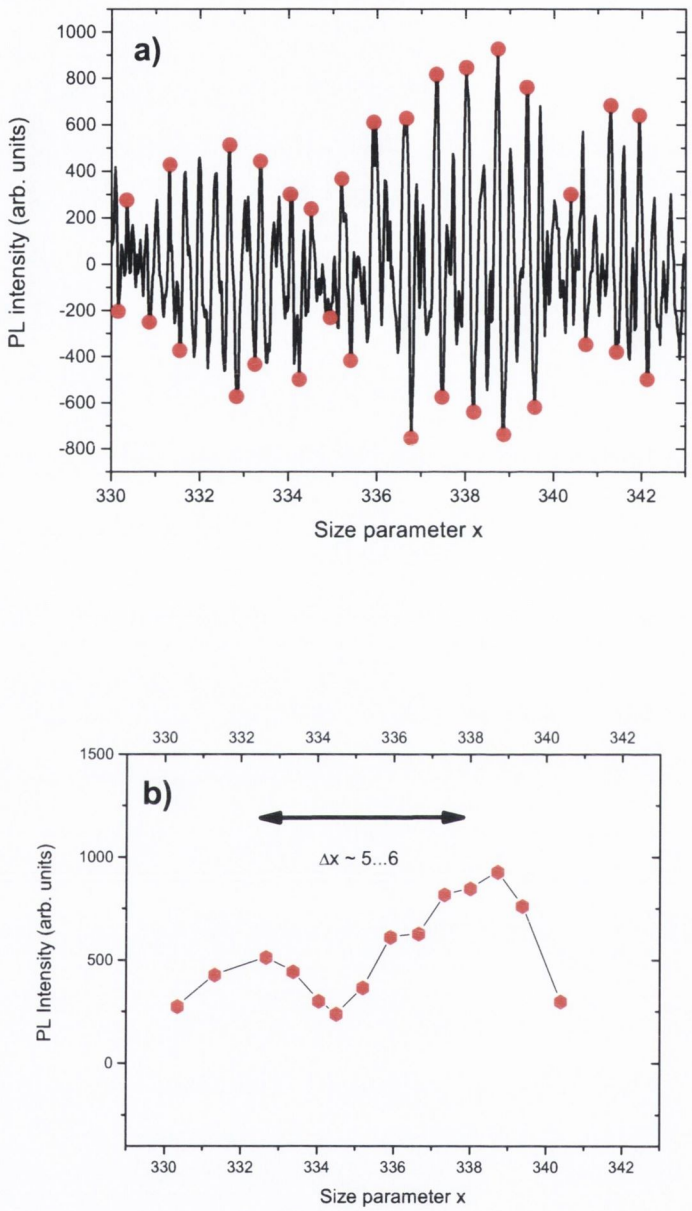

Figure 5. *Interference structure of the resonances in the PL spectrum. a) Spectrum with peak maxima and minima (red dots), determined with a programme. b) Plot of peak maxima without PL spectrum.*

Apart from the strong luminescence, the measured spectrum also shows a sinusoidal-shaped intensity fluctuation of the resonant modes. This effect is caused by interference of the reflected light between the bottom and the top of the microsphere [6]. A rough estimation of the periodicity in the PL spectrum verifies that the intensity modulation in the measurements is caused by this interference effect. The analysis of the PL spectrum showing the intensity modulation is illustrated in Fig. 5a and 5b. The PL emission as a function of the size parameter x is shown in Fig. 5a. The maxima of the resonance peaks were identified in the spectrum (red dots in Fig. 5a). These maxima were plotted separately in Fig. 5b. From this plot, the periodicity Δx was estimated to Δx between 5 and 6. Applying the approximation formula

$$\Delta x = \frac{\pi}{n-1} \quad , \tag{4.3}$$

given in [14] for the dependence of periodicity of the interference structure on the refractive index n, a refractive index for the measured period Δx was determined to be

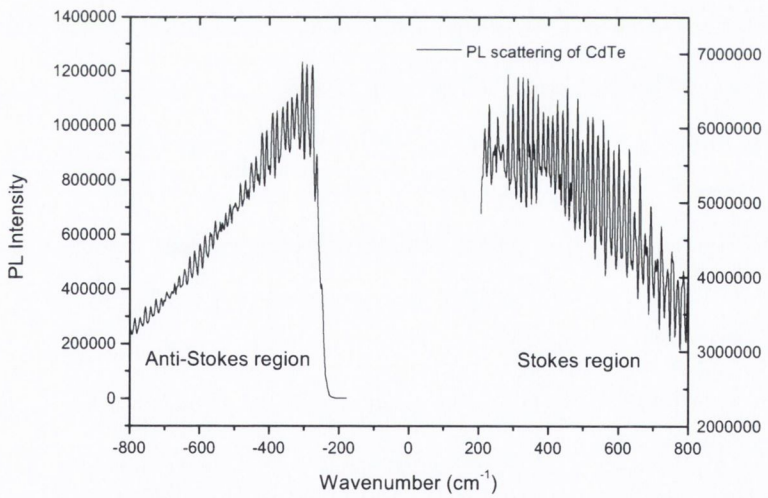

Figure 6. *PL spectrum of CdTe nanocrystals coupled to a spherical microcavity with 70 μm diameter. Excitation with a HeNe laser at 10 mW.*

between $n = 1.52$ and $n = 1.62$, which is a reasonable result as the refractive index of polystyrene is *about* $n = 1.58$. A more accurate determination of the refractive index in this wavelength range from the interference periodicity would only be possible with a PL

spectrum which includes more interference peaks. However, our experimental data do not allow carrying out a more accurate analysis due to the spectral width limited by the emission of the nanocrystals. In Fig. 6, another example for a PL measurement with excitation below the first electronic transition of CdTe nanocrystals is shown. This time, the substrate was porous polystyrene instead of a silicon wafer, therefore there is no Raman peak from the silicon substrate in the spectrum. The plot also shows no polystyrene Raman features of the substrate or the sphere material in the spectrum. The background emission is caused by photoluminescence of the nanocrystals that is not coupled into the microsphere but scattered from the sphere surface. Once again, the intensity of the emission in the anti-Stokes region is about one order of magnitude smaller than in the Stokes region, which is a remarkably high efficiency for photoluminescence created by excitation with off-resonance pump energy at a point of low absorption. In the following measurements, we varied the coupling efficiency of the microsphere. As a result we observed a superposition of Raman scattering and photoluminescence in the spectrum. Further measurement revealed a superposition of photoluminescence from the CdTe nanocrystals and Raman scattering from the polystyrene microsphere and the CdTe monolayer.

The *70* micrometer sphere was excited with the Ar^+-ion laser at *488 nm*. The coupling efficiency was varied by exciting the sphere at two different focus positions. In the first measurement, we focused the beam in the centre of the sphere and in the second measurement at the rim of the sphere. One spectrum was taken from a bulk polystyrene film on a plane substrate as a reference. The graphs are shown in Fig. 7. In agreement with the measurements in [7], the overall intensity of the spectrum taken when excited at the rim of the sphere is higher compared to the intensity when excited in the sphere centre. The high-Q optical resonances are located near the surface of the sphere, where they travel along the circumference. When the sphere is excited in the centre, the light cannot be well coupled into the high-Q modes efficiently, as the light in the microsphere travels almost perpendicular to the incoming beam. A considerable fraction of the light in this excitation direction is refracted through the sphere (see Fig. 8 a)). Excitation in the centre is discussed in detail in the next chapter, where it plays an important role in controlling radiation pressure exerted on the sphere. Focusing at the rim of the sphere couples the light into the optical modes near the surface more efficiently (see Fig. 8 b)). If light would only be

coupled into the surface modes by refraction on the surface of the incoming beam, the higher efficiency would not be apparent, since the beam hits the sphere surface almost tangential, most of the light would be totally reflected. The coupling is still more efficient than in the sphere centre excitation for the reason, that light which is not even touching the sphere surface when examined from the ray optics point of view, couples into the sphere by highly efficient evanescent

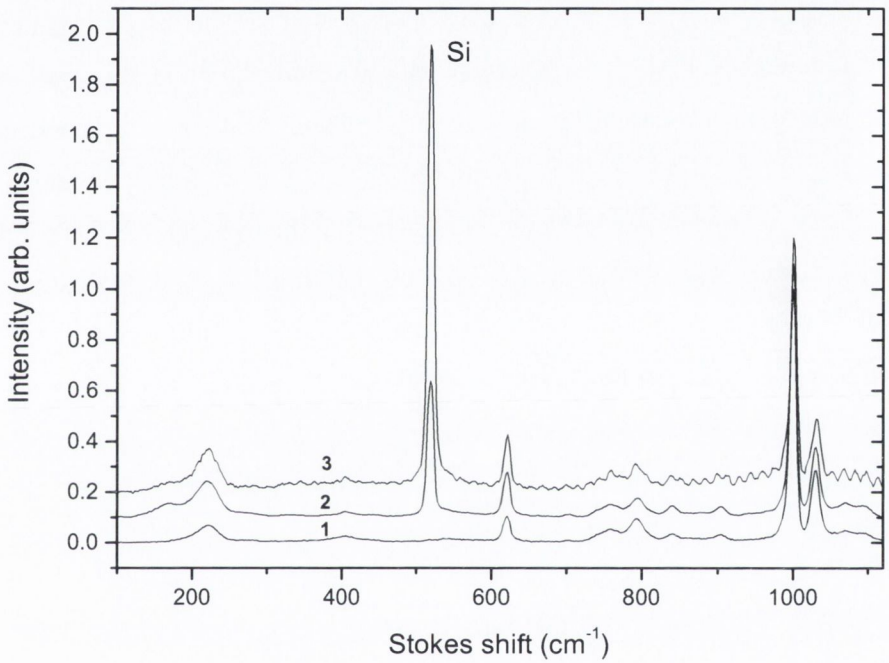

Figure 7. *Raman spectrum of:*

(1) bulk polystyrene film on glass substrate.

(2) polystyrene microsphere/CdTe quantum dots excited in the sphere centre.

(3) polystyrene microsphere/CdTe quantum dots excited at rim of sphere.

coupling. This can only be physically described when the light is regarded as an electromagnetic wave as discussed in [8] and [9] in detail. The spectrum of Fig. 7 shows the Raman measurement of a polystyrene film on a glass substrate. The graph shows several Raman modes intrinsic to polystyrene (*220, 620, 759, 793, 1001* and *1031* cm^{-1}). All three measurements include the LO phonon mode of silicon at *520* cm^{-1} from the substrate. The intensity of this Si peak has a maximum in the third measurement where the

beam passes the sphere surface at the rim and the light is reflected directly from the substrate. The broad peak at around $220\ cm^{-1}$ with a long tail was further analysed. The peak is actually composed of the LO phonon mode (166 cm^{-1}) of CdTe and a Raman mode ($220\ cm^{-1}$) of polystyrene. The Lorentzian fit of both single peaks is shown in Fig. 9 (dashed lines). The combined peak shows, that as a result of the strong interaction between the vibrational states of the nanocrystals and the optical resonant modes of the microcavity, it was possible to observe Raman scattering from a CdTe QD layer of less than *5 nm* on the sphere surface. The optical feedback inside the microsphere strongly increases the probability of Raman scattering. When the laser was focused at the rim of the microsphere, resulting in an enhancement of the evanescent field coupling of the Gaussian beam, the whispering gallery resonances of the microcavity became visible as a ripple structure. In comparison to the measurements shown in Fig. 4 and Fig. 6, the pump intensity was lowered to $P = 2mW$ so that the photoluminescence from the nanocrystals did not dominate the Raman scattering. However the spectrum induced by Raman scattering is superimposed on the photoluminescence of the CdTe nanocrystals. The conclusions for the first series of measurements confirm our predictions, that the high-Q microcavity strongly enhances electronic or vibrational excitation processes due to the coupling to the optical resonances in the microcavity. By changing the intensity and coupling efficiency, Raman scattering

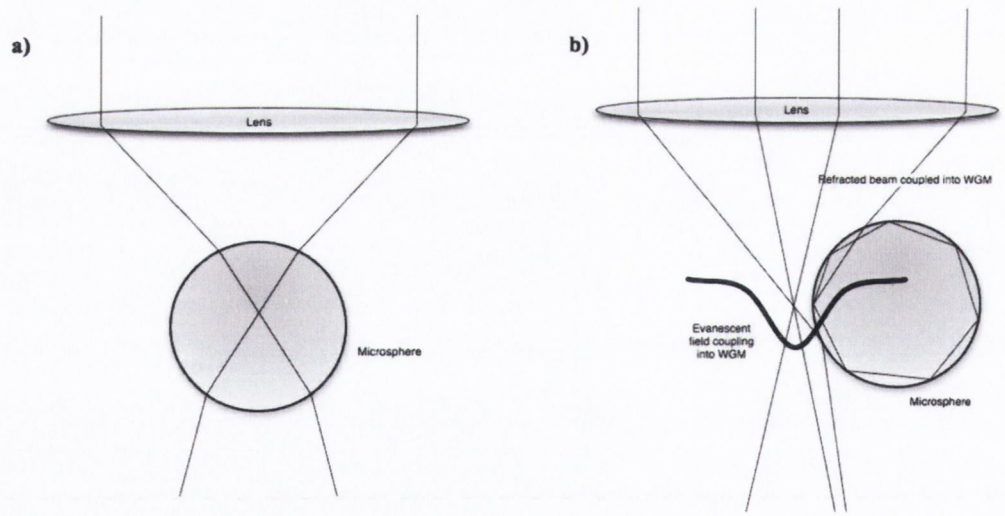

Figure 8. *a) On-axis focus of laser beam, light is refracted through the microsphere. b) Off-axis focus of laser beam. Evanescent coupling and coupling through refraction.*

and photoluminescence was observed. In particular, a strong anti-Stokes PL emission was detected. Varying the coupling efficiency by changing the excitation position and varying the intensity of the laser allowed observation of Raman scattering from the microcavity material and a monolayer CdTe nanocrystals as well as photoluminescence from the nanocrystals at the same time. The CdTe LO phonon mode showed strong enhancement of weak Raman scattering due to the optical feedback in the microcavity as well as strong enhancement of the up-conversion process for anti-Stokes photoluminescence of the CdTe nanocrystals during off- resonance excitation.

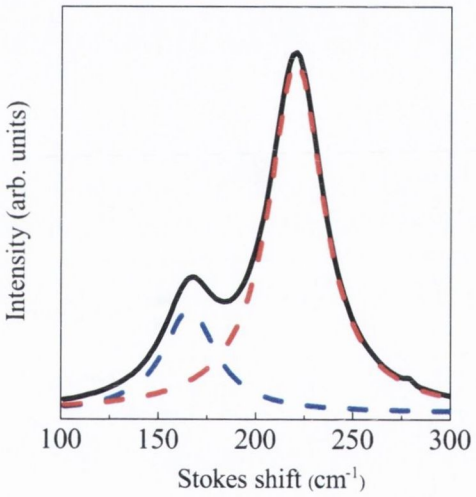

***Figure** 9. Lorentzian fit of CdTe LO phonon peak (blue) and PS Raman peak (red).*

4.3 Resonance mode identification

The optical resonances in a microsphere are determined by their polarisation (TE or TM), the angular mode number ℓ, the radial mode number n (mode order) and the azimuthal mode number m. To identify the resonances in the PL spectrum of our *70 μm* sphere samples, we applied an approximation formula which is valid for large spheres. The requirement is a large size parameter $x >> 1$ and a large angular mode number $\ell >> 1$. The asymptotic equation used is taken from a publication by Schiller and Byer in 1991 [10]. The PL spectrum indicates the existence of higher order modes (modes with higher radial mode number) in the form of smaller and partly overlapping peaks. We focused on the identification of resonances with mode order $n = 1$, which have the highest intensities in the spectrum. The asymptotic equation is given by

$$nx_{l,n} = \ell + \frac{1}{2} - \zeta_n \left(\frac{\ell + 1/2}{2} \right)^{1/3} - \frac{np}{\sqrt{n^2 - 1}} + \frac{3\zeta_n^2}{2^{2/3} 10(\ell + 1/2)^{1/3}} - \frac{n^3 p(2p^2/3 - 1)\zeta_n}{2^{1/3}(n^2 - 1)^{3/2}(\ell + 1/2)^{2/3}}. \qquad (4.4)$$

The spectral resonance position is given as the size parameter $x_{\ell,n}$. The refractive index of the sphere is n, the polarisation is expressed by $p = 1$ for TE modes and $p = 1/n$ for TM polarised modes and ζ_n is the root of the Airy function of the order n. The wavelength of the resonances is $\lambda_{\ell,n} = 2\pi r / x_{\ell,n}$, where r is the sphere radius. With this equation, we clearly identified the first order TE and TM modes in the PL spectrum. The graphs in Fig. 10 show the calculated and measured TE and TM modes wavelengths as a function of the angular mode number. The gaps within the graphs are due to the Si TO Raman mode, which dominated several resonances, and the region of the excitation laser line, blanked out by a plasma notch filter. The plots show that the optical resonances could be identified by the angular mode number without utilising the numerical approach of the Mie calculations, which requires a large computational effort in comparison with the analytical approximation approach. Identifying the resonances is fundamental for further studies and calculation, e. g. for optimal coupling to external fibre optics, for optimised evanescent

field excitation or for comparisons to parameters obtained with the Mie scattering theory (maximum Q-factor, etc.).

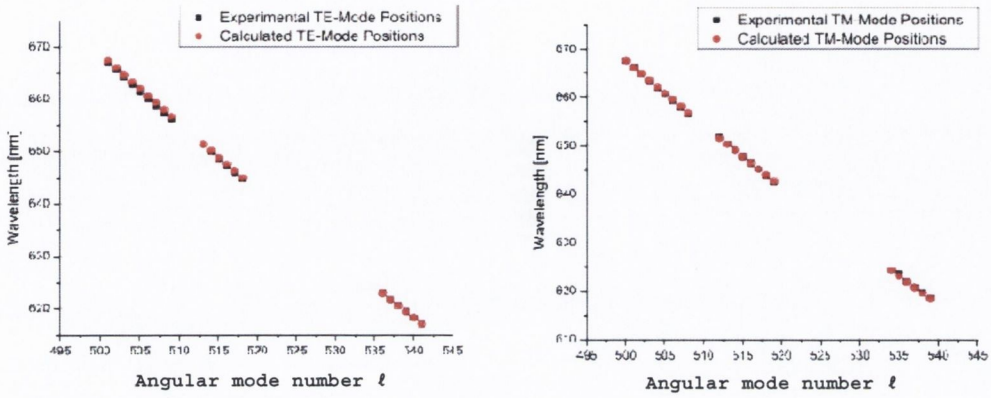

Figure 10. *Identified first order TE and TM resonances in the PL spectrum in regards of the angular mode number ℓ.*

4.4 Spectral shift and intensity decay of resonances during continuous excitation

In this section, the photostability of the nanocrystal-microcavity system during excitation over a longer time period is discussed. The observation of characteristic changes is distinguished between the effect of laser radiation on the CdTe colloidal nanocrystal layer and the effect on the dielectric microcavity. The laser excitation and the resulting heating of the samples affect both the nanocrystals and the sphere. While the heat mainly induces changes in the microcavity, the high photon intensity causes specific changes in the photoluminescence intensity of the nanocrystals due to chemical and electronic interaction induced by the laser beam. The stability of colloidal nanocrystals is an important matter for applications based on colloidal nanocrystals. It requires detailed studies of the photoluminescence properties when the nanocrystals are used in different environments. Typically, photodegradation is observed when colloidal nanocrystals are exposed to

intensive laser light, resulting in a quenching of the photoluminescence intensity. Up to the present time, the mechanisms behind the photoluminescence quenching are not fully understood. In the experimental investigation, the coated microspheres were continuously excited for a time period of 18 minutes, a PL spectrum was taken about every 30 seconds. The HeNe laser with an output power of *3 mW* was used as the excitation source. Two different data series were taken for the microsphere samples. The first data set was taken during excitation with a laser output power of *3 mW*, the second one with an output power of *0.3 mW*, lowered with a neutral density filter (*100%* and *10%* transmission). The samples are the same *70 μm* polystyrene microspheres coated with one monolayer of CdTe nanocrystals on a silicon substrate as in the previous measurements. The experiment was carried out by placing the sphere sample on the Si-substrate into the micro-PL machine. The laser was focused with the 100x objective on the sphere and the sample was illuminated for 18 minutes while a PL spectrum was taken about every 30 seconds. To analyse the decay in PL intensity of the CdTe nanocrystals, we integrated the intensity over the whole spectral range for each taken PL spectrum. That provides the overall photoluminescence intensity of the scattered light from the microsphere over the whole time period every 30 seconds. The plots in Fig. 11 and Fig. 12 show the integrated intensity for the time period, the sphere was excited

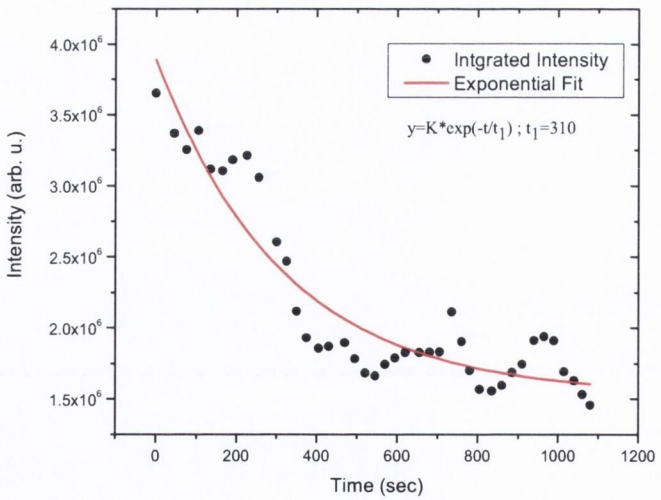

Figure 11. *Decay of integrated intensity over time at 0.3 mW HeNe laser output power.*

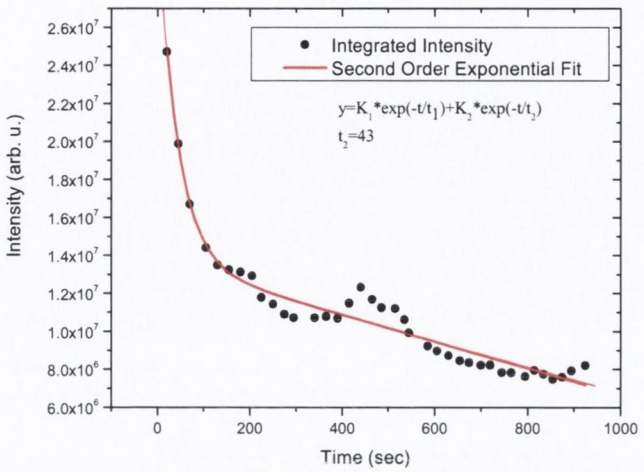

Figure 12. *Decay of integrated intensity over time at 3 mW HeNe laser output power.*

continuously. The laser output power for the measurement series in Fig. 11 is *0.3 mW* and for the series in Fig. 12, *3 mW*. The graph in Fig. 11 clearly shows a slower decay at *0.3 mW* in the PL intensity compared to the decay at *3 mW* in Fig. 12. At higher laser output power, the decay is fast within the first few minutes, and then continues by a slower, almost linear decrease in the overall intensity. A unique characteristic in the decay process is the fluctuation in the intensity gradient which is more pronounced in the low intensity measurement. Firstly it was noted, that the photodegradation shows an intensity dependency. The PL intensity dropped by half of the initial value until around $t = 400$ seconds in the *0.3 mW* measurement, while the drop took around $t = 100$ seconds in the *3 mW* measurement. The experimental curves were fitted with exponential functions to determine the time constant for the decay process. Very similar observations were found in [11] where photo-oxidation of colloidal CdSe and CdSe/ZnS embedded in polymer thin films was systematically studied. The multi-exponential intensity decay was observed with time constants of the shortest exponential decay term in the orders of *10* seconds (experimental results: *29 s, 34 s, 49 s*). Furthermore, the time constants of the multi-exponential decays are in the orders of *10 s, 100 s,* and *1000 s,* respectively. This is in agreement with our observations. The intensity quenching is attributed to photo-oxidation under the O_2 atmosphere which is assumed to be an irreversible process. In [12], the

photostability of thiol-capped CdTe nanocrystals is investigated in living cells. Again, the intensity decay times under continuous irradiation are in the order of *10* seconds. The photo-bleaching is also attributed to the photo-oxidation process due to the O_2 atmosphere. It was also shown in [12] that the decay time does not only depend on the intensity but on the local concentration of the nanocrystals. Another publication [13] verifies photo-oxidation of PbSe and PbSe/PbS nanocrystals in an oxygen atmosphere with time constants of the exponential decay in the same order (15 seconds). We can conclude from the experimental results and the published literature on this subject, that a relatively slow irreversible photo-oxidation of the CdTe nanocrystal layer on the sphere surface takes place in an oxygen atmosphere. Photoluminescence quenching due to charged excitons can be ruled out, as this process occurs on a much shorter timescale.

In the published work, the fluctuation in the intensity gradient was not reported. The gradient suggests a periodic variation of intensity superimposed on the exponential decay. The modulation of the exponential decay suggests a periodic recovery of the nanocrystal photoluminescence. To investigate the periodic intensity fluctuations in Fig. 11, the exponential background was subtracted (Fig. 13). The four peaks including the second peak which appears very weak show a periodicity of about t = 253 seconds. Periodic PL

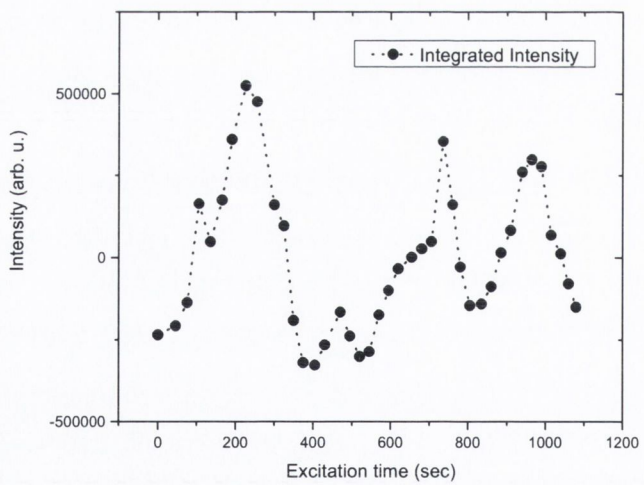

***Figure 13**. Fluctuation of integrated intensity over time without exponential decay background.*

recovery on such a large time scale has not been reported yet to our knowledge. A possible mechanism to explain the periodic behaviour is related to surface defects on the

nanocrystals. Surface defects are energetically located just below the first electronic transition level in the bandgap. During excitation, the nanocrystals can be charged by electrons trapped on the surface defects. The localised separation of the electron-hole pair within the nanocrystal causes an electric field in between the separated charge carriers. The following two processes are suggested to cause luminescence quenching. On the one hand, the electric field strongly reduces excitation of new electrons located within the electric field of an electron-hole pair. On the other hand, in case that an electron is excited within the electric field, the electron is moved in the field and separated from the hole. The energy that the electron gains in the field is larger than the confinement energy so that the probability is very high that the electron is lifted into the surrounding matrix. Both processes reduce the radiative recombination rate and lead to a quenching of the photoluminescence. Due to the gradual heating of the sphere during continuous excitation, the trapped electrons are released by thermal energy. Discharging the nanocrystals results in a recovery of the photoluminescence until the point is reached where the new charge carriers are trapped in the surface defect states. This process repeats itself periodically during excitation. Higher laser intensity results in a higher sample temperature which causes faster de-trapping of carriers and a weaker intensity fluctuation process, which is in agreement with our observation of a decay at 3 mW laser output power in Fig. 12 with less pronounced intensity recovery.

The following analysis discusses the change of the WGM spectrum during long time excitation with the laser source. The experiment reveals potential problems when the excited microsphere is not temperature stabilized. The tightly focused laser beam heats the sample to a point where it considerably affects the mode structure. However, the characteristic change due to heating can be useful for potential applications which benefit from this thermal effect, for example for frequency tuning of resonance modes in fibre optics communications when the microcavity is applied as switch or add/drop filter.

The free spectral range between the resonant modes depends on the refractive index of the sphere and the surrounding medium as well as the radius of the microsphere. Changes of the WGM mode structure can be induced by a change of these parameters. The free spectral range in a large microsphere depends mainly on the size of the sphere. The mode spacing $\Delta\lambda$ of two adjacent modes λ_n and λ_{n+1} with the same polarization can be approximated by the equation [14]

$$\Delta\lambda = \frac{\lambda^2 \arctan\sqrt{m^2 - 1}}{\pi d\sqrt{m^2 - 1}}, \tag{4.5}$$

where m is the refractive index and d the diameter of the microsphere. This equation is valid for mode orders $\ell >> 1$ and size parameters $x >> 1$, as well as $x/\ell < 1$. Our $70\ \mu m$ spheres satisfy these conditions. Due to the size of the sphere, the free spectral range of the resonances is quite small, resulting in a high number of resonances within the measured PL spectrum. Furthermore, the PL measurements taken about every 30 seconds within the time frame of up to 18 minutes produced a vast amount of data. To study changes of the resonances in the PL spectrum during the excitation period, a fast method to analyse the individual spectra was required. A common procedure to investigate periodic datasets is the Fast Fourier Transform (FFT), where any complex signal can be decomposed into its frequency components. This applies conveniently to our resonance spectrum when we analyse the spacing of the WGMs. The periodicity of the resonances, corresponding to the free spectral range can be revealed by the frequency spectrum of the FFT. The unit of this spectrum can be interpreted as resonances per nm. To derive the resonance mode spacing, the reciprocal value of the designated peak in the frequency spectrum is taken which corresponds to nm per resonances or free spectral range. The PL spectrum was divided into two parts, the Fourier transform was carried out for each part separately. The division of the spectra is carried out, because the spacing between the modes is not constant over the whole spectral range. The mode spacing is wavelength dependent due to the resonance characteristics of the microcavity, whereas the dependency diminishes with an increased sphere size. The resonance spacing also shows a spectral dependency according to the dispersion of the refractive index of the sphere material. As a result of the spectral dependency of the spacing, the Fourier transform only provides an averaged free spectral range, depending on the spectral width of the region which is chosen for the FFT transform. To reduce the averaging of the free spectral range to a minimum, the spectrum was divided into two parts.

The first Fourier transform was carried out within the spectral region between *640 nm* and *655 nm*, the second one between *655 nm* and *670 nm*. As discussed above, the peaks in the frequency domain spectrum correspond to periodicities in the spectrum. In the resonance spectrum of our measurements, the transform shows the inverse spacing of the WGMs

averaged over the range. Four PL spectra are evenly picked out of the timeframe (after 1 minute, 6 minutes, 12 minutes and 18 minutes) of the excitation time period and the Fourier transform is determined (Fig. 14, 15). The PL intensity spectrum plotted versus the wavelength λ in *nm* units results in a frequency spectrum with nm^{-1} units. The peak positions in the Fourier spectrum give the inverse value of regular spacing in the WGM spectrum in nm^{-1}. The first peak in the Fourier graph belongs to the spacing between the modes of the same polarisation, either TE or TM. As the spacing between two TE modes is almost the same as for the TM mode spacing, only one single peak is observable in the Fourier spectrum. The double peak at around $1.5\ nm^{-1}$ is attributed to the spacing between modes of different polarisation. Either TE or TM mode with the same mode order n or the spacing between a TE and TM mode with a mode order n and $n+1$, respectively. The first peak of the *0.3 mW* output power measurement for the first part of the PL spectrum is at 0.794 nm^{-1} which corresponds to a mode spacing of $\Delta\lambda=1.260\ nm$. Calculations based on Eq. 4.5 gave a theoretical value *of* $\Delta\lambda=1.305\ nm$. A wavelength of $\lambda=644.5\ nm$ was chosen for the calculation, which is the value in the middle of the PL spectrum. For the second part of the PL spectrum, the peak is at $0.793\ nm^{-1}$ which corresponds to a spacing of $\Delta\lambda=1.389\ nm$. The calculated value is $\Delta\lambda=1.380\ nm$ for $\lambda=662.5\ nm$. Both values are in good agreement with the measurements considering, that the Fourier transform produces an averaged spacing over the measured spectrum. The slightly decreased spacing in the red spectrum of the two regions is evident through the quadratic wavelength dependence given in the equation. Apart from the first peak and the second double peak in the Fourier spectrum, there are several peaks corresponding to smaller spaced modes. These modes are assigned to higher order optical resonances in the spectrum. In regards to the spectral changes of the modes during continuous excitation, the four Fourier plots reveal that the spacing is constant over time within the accuracy given of the analysis due to spectral averaging. However, the accuracy is limited because the spacing is only an average of all the modes within the range of the PL spectrum of the transform. For a more accurate analysis, seven resonant modes from the PL spectrum were selected and the distance to the adjacent mode was determined as a function of excitation time. The analysis shows a very small total decrease in spacing within the excitation time frame of $\Delta\lambda=0.003\ nm$ for all seven resonant mode pairs. The small decrease in the free spectral range is not revealed in the Fourier transform due to the limited resolution. Nevertheless, the Fourier spectrum

offers a convenient method to quickly evaluate the free spectral range of the WGMs in a dense PL resonance spectrum of large spherical resonators.

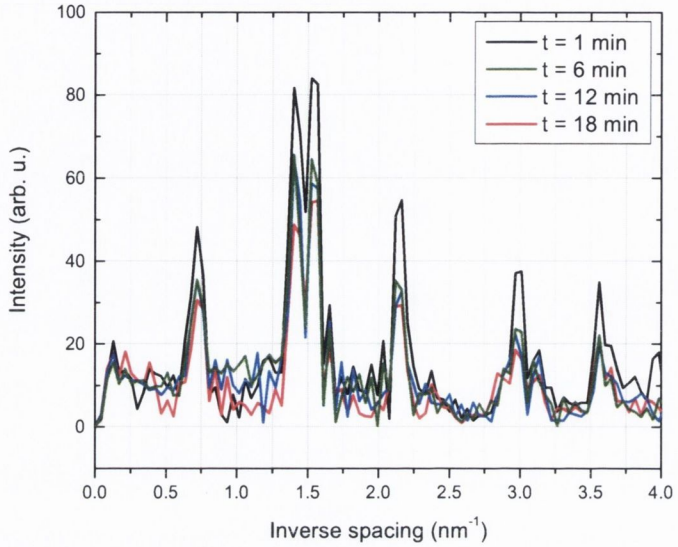

Figure 14. *Fourier spectrum of the first half of the photoluminescence spectrum at 10% laser intensity for four measurements taken during excitation.*

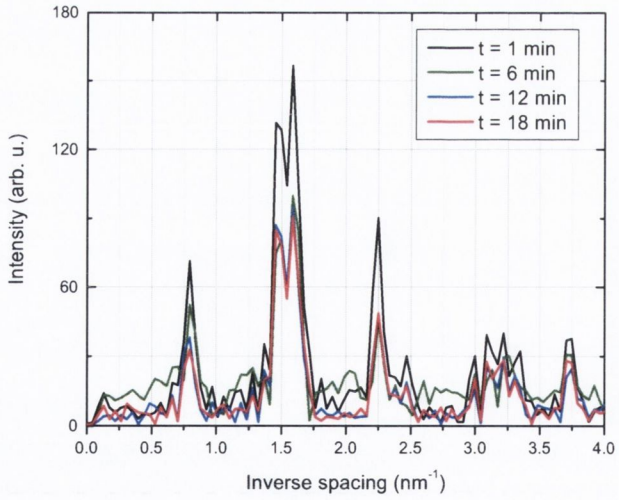

Figure 15. *Fourier spectrum of the second half of the photoluminescence spectrum at 10% laser intensity for four measurements taken during excitation.*

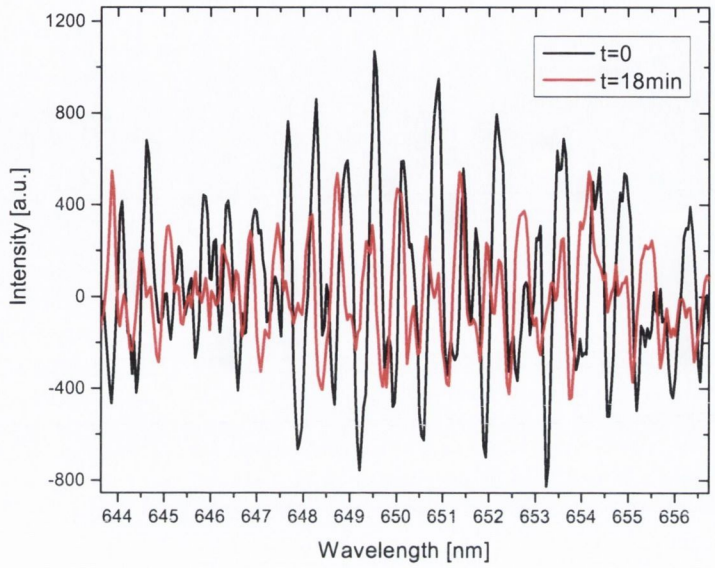

Figure 16. *PL spectra of 70 μm spheres at the beginning of the continuous excitation (black line) and after 18 minutes of excitation (red line) at 3 mW laser output power.*

Apart from the PL intensity decrease, the effect of continuous excitation on the spectral position of the resonant modes was studied. The resonances are characteristic of the size of the microcavity, the refractive index of the microcavity material and the medium. Any changes of these three parameters result in a shift of the resonance frequencies. To evaluate changes during excitation, the first PL spectrum taken at the beginning of the excitation period and the last PL spectrum in the measurement series with *3 mW* excitation power were plotted in a graph shown in Fig. 16. The optical resonances in the spectrum revealed a blue shift during the excitation period. To characterise the wavelength shift of the optical resonances, the wavelengths of two particular WGMs were plotted versus the excitation time. The first resonant mode was selected from the lower end of the measured spectrum, while the other resonant mode was picked from the higher end of the spectrum. The two graphs in Fig. 17 show the shift of the two actual resonant modes over the excitation time period. The spectrum was taken at the reduced power setting of *0.3 mW*. The two plots in

Fig. 18 show the measurement at *3 mW* laser output power. The step-like gradient of the graphs originates from both the resolution limit of the spectrometer encountered in this measurement and the time steps, as the spectrum was taken about every 30 seconds. Following the linear fit line along the data points show a linear blue shift of the particular resonance mode tracked during excitation with the HeNe laser. The slope of the linear fit represents the shifting speed of the mode in nm/seconds. At *0.3 mW* output power, the modes shifted with a velocity of $v = -7.496\ 10^{-4}$ *nm/sec* for the first mode and $v = -7.572\ 10^{-4}$ *nm/sec* for the second mode, respectively.

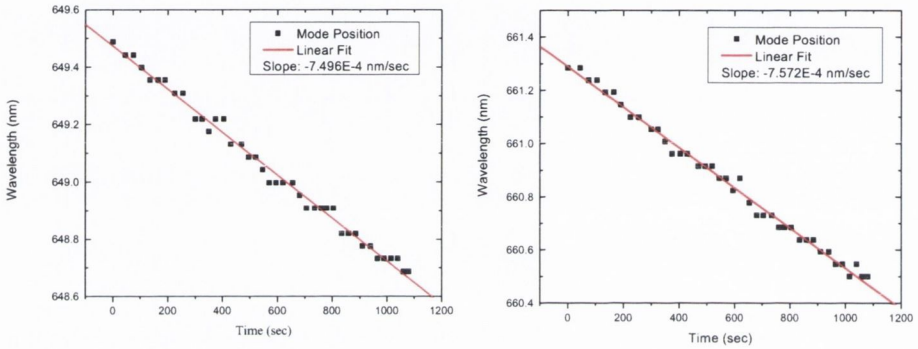

Figure 17. *Wavelengths of resonance modes plotted versus the excitation time at continuous laser excitation at 0.3 mW laser output power.*

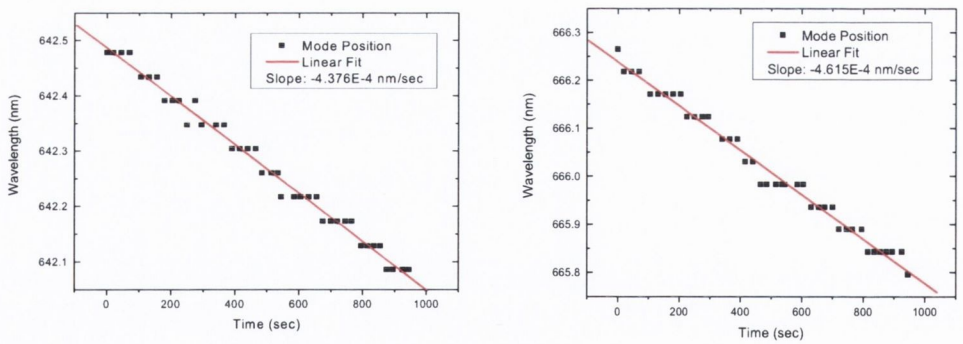

Figure 18. *Wavelengths of resonance modes plotted versus the excitation time at continuous laser excitation at 3 mW laser output power.*

The overall wavelength shift for both modes is $\Delta\lambda = 0.80\ nm$ and $\Delta\lambda = 0.78\ nm$. The shifting speed for the *3 mW* power measurement is $v = -4.376\ 10^{-4}\ nm/sec$ and $v = -4.615\ 10^{-4}\ nm/sec$ and the overall shift is $\Delta\lambda = 0.47\ nm$ and $\Delta\lambda = 0.39\ nm$. Thus, the overall shift is about twice as large in the *0.3 mW* excitation series as in the *3 mW* excitation series. Surprisingly, the shifting speed of the resonant modes in the *0.3 mW* measurement is almost twice as high as in the *3 mW* measurement. It is also slightly slower towards the shorter wavelengths region at the same excitation power due to the refractive index dispersion of the polystyrene microsphere. The resonance shift is induced by either a refractive index change due to temperature change or a thermal size expansion of the microsphere. Expansion of the microsphere due to heating produces a red-shift of the modes while contraction causes a blue-shift in the resonant mode spectrum. Due to the fact that the polystyrene microsphere expands with increasing temperature, the blue shift could not be explained by thermal expansion of the sphere. Otherwise, the blue shift is probably induced by a refractive index change of the polystyrene sphere and the polyelectrolyte layer on the surface. Nevertheless, the mode shift can be induced by a superposition of the increased radius and the refractive index change [15, 16]. In [17], a change of the shifting direction was observed during excitation due to the overlap of a red and a blue shifting process. The blue-shift at the beginning caused by thermal contraction of the SiO_2 microsphere reversed to a red-shift when organic material was deposited on the surface which corresponds to an increase of the effective sphere radius. A blue shift of the resonances can be induced by the heating of the polystyrene sphere due to the laser when the thermo optical coefficient of the sphere material is negative. The induced drift must then compensate the red-shift caused by the sphere expansion. The thermo-optical coefficient describes the relative change of the refractive index over the relative temperature change of the material. A negative coefficient means that the refractive index decreases with increasing temperature. The Mie-scattering calculations reveal that the resonance modes experience a blue-shift when the refractive index decreases. Polymers such as melamine formaldehyde or polyelectrolyte multi-layers belong to the materials with negative thermo-optical coefficient. The thermo optical coefficient for polymers is found in the range of

$$\frac{dn}{dT} \approx -1 \cdot 10^{-4} to - 3 \cdot 10^{-4} K^{-1}. \tag{4.6}$$

The negative coefficient induces a blue shift in the spectrum with increasing temperature, which is in agreement with our observations. A more quantitative treatment of the temperature-induced shift follows in chapter 5. Although this observation requires more detailed studies, it shows potential for microsphere sensing investigations. The slope of the graph, which corresponds to the shifting speed of the modes, could be a new variable parameter to sense the sphere environment or deposition material on the surface with high sensitivity. Up to now, only the wavelength shift was considered as the variable for potential microsphere sensor applications. The shifting speed of the optical modes during continuous excitation could provide a new parameter for microsphere sensors to increase the sensitivity or give additional dynamic information about the sensed environment or material deposited on the sphere surface. A variation of the shifting speed detected during the monitoring process could provide information of changes in the material density of the sensored medium. The active CdTe layer on the sphere surface can be beneficial for a microsphere sensor application with regards to the excitation source. Due to the broad luminescence of the nanocrystals, a tuning of the excitation laser would not be necessary anymore when the nanocrystal emission is sufficient for the mode shift detection. A passive microsphere sensor requires tuning of the excitation laser over the optical resonance frequency to detect any changes. Using active microsphere sensors could potentially reduce the costs and reduce the complexity of the system.

4.5 Conclusions

Photoluminescence and Raman measurements carried out on *70 μm* polystyrene microspheres coated with a monolayer of CdTe nanocrystals have shown a strong enhancement of interaction between the optical resonances (WGMs) in the microsphere and the CdTe nanocrystals on the sphere surface. Raman scattering from a CdTe nanocrystal mono layer was observed due to strong enhancement of the Raman signal. We also measured strong photoluminescence in Stokes- and especially in anti-Stokes region, pointing out the observation of a highly efficient anti-Stokes up-conversion of electrons. It was demonstrated that a variation of the coupling efficiency results in either a strong Raman signal or a strong photoluminescence signal from the excited nanocrystals. Characterisation of the optical resonances by means of approximation formulae and a Fourier transform technique allowed us to identify the modes and analyse the spectrum during continuous long-time excitation of the microsphere-emitter. We applied a Fourier transform for a quick identification of the free spectral range of the resonances in a dense WGM spectrum. The observed linear blue shift of the resonances during continuous excitation indicates possibilities for further analyses and studies for a potential implementation as a new active microsphere-emitter sensor. The linear mode shift also demonstrates the possibility of continuous tuning of the optical resonances.

References

[1] D. A. Long, and MacGraw-Hill, "Raman spectroscopy", New York, Chap. 4.3.7 (1977).

[2] K.I. Rusakov, A.A. Gladyshchuk, Yu.P. Rakovich, J.F. Donegan, S.A. Filonovich, M.J.M. Gomes, D.V. Talapin, A.L. Rogach, A. Eychmueller, Opt. Spectros. 94 (6), 921–925 (2003).

[3] X. Wang, W.W. Yu, J. Zhang, J. Aldana, X. Peng, M. Xiao, Phys. Rev. B 68, 125318 (2003).

[4] Y. P. Rakovich, S. A. Filonovich, M. J. M. Gomes, J. F. Donegan, D. V. Talapin, A. L. Rogach, A. Eychmueller, Phys. Stat. Sol. (b) 229 (1), 2002.

[5] Y. P. Rakovich, J. F. Donegan, N. Gaponik, A. L. Rogach, Appl. Phys. Lett. 83 (13), 2003.

[6] Petr. Chylek, Jiyu Zhan, J. Opt. Soc. Am. A 6, 1846 (1989).

[7] Yu. P. Rakovich, L. Yang, E. M. McCabe, J. F. Donegan, T. Perova, A. Moore, N. Gaponik, A. Rogach, Semicond. Sci. Technol. 18, 914 (2003).

[8] J. A. Lock, J. Opt. Soc. Am. A 15 (12), 2986 (1998).

[9] A. Serpenguezel, S. Arnold, G. Griffel, and J. A. Lock, J. Opt. Soc. Am. B 14 (4), 790 (1997).

[10] S. Schiller, and R. L. Byer, Opt. Lett. 16 (15), 1138 (1991).

[11] A. Y. Nazzal, X. Wang, L. Qu, W. Yu, Y. Wang, X. Peng, and M. Xiao, "Environmental effects on photoluminescence of highly luminescent CdSe and CdSe/ZnS core/shell nanocrystals in polymer thin films", J. Phys. Chem. B **108,** 5507 (2004).

[12] J. Ma, J.-Y. Chen, J. Guo, C. C. Wang, W. L. Yang, L. Xu, and P. N. Wang, "Photostability of thiol-capped CdTe quantum dots in living cells: the effect of photo-oxidation", Nanotechnol. **17**, 2083 (2006).

[13] J. W. Stouwdam, J. Shan, F. C. J. M. van Veggel, A. G. Pattantyus-Abraham, J. F. Young, and M. Raudsepp, "Photostability of colloidal PbSe

and PbSe/PbS core/shell nanocrystals in solution and in the solid state", J. Phys. Chem. C **111**, 1086 (2007).

[14] P. Chylek, "Resonance structure of Mie scattering: distance between resonances"J. Opt. Soc. Am. A 7 (9), 1609 (1990).

[15] S. Arnold, M. Khoshsima, I. Teraoka, S. Holler, F. Vollmer, Optics Lett. 28, 272 (2003).

[16] F. Vollmer, S. Arnold, D. Braun, I. Teraoka, A. Libchaber, Biophysical Journal 85, 1974 (2003).

[17] F. Vollmer, D. Braun, A. Libchaber, M. Khoshsima, I. Teraoka, and S. Arnold, Appl. Phys. Lett. 80 (21), 4057 (2002).

Chapter 5

Radiation pressure induced mode splitting in a spherical microcavity with an elastic shell

5.1 Introduction

The radiation pressure created by a focused laser beam can be used to trap, levitate and manipulate micro- or nanometer-sized dielectric particles and biological cells [1-2]. Although photons are massless particles, they can transfer their momentum to the particle. The strong gradient of the electro-magnetic field intensity in the region of the beam waist gives rise to the so-called gradient force, which when working against the gravitational force provides a method for optical binding and manipulation of ultra-fine particles and mesoscopic systems. In addition, a beam of light can exert sufficient radiation pressure to move a microstructured object along the direction of the beam propagation under the effect of the scattering force. This radiation-pressure-induced opto-mechanical interaction shows great promise for a variety of applications in the field of optically actuated micro-optical-electromechanical systems (MOEMS) [3-4], laser cooling [5], spectrum analysis [6], optical information processing [4,6] and quantum informatics [5].

This chapter presents new results on the mode manipulation by radiation pressure in a micro-scale optical cavity with a several nanometer thick shell. In this approach, we utilise small spherical microcavity structures whose modes are highly sensitive to changes of the refractive index of the sphere itself [7-8] or to the environment in close proximity to the sphere surface [9-10]. WGMs also show remarkable sensitivity to deformation which allows fine tuning of the WGM's spectral position and Q-factor [11, 12]. Motivated by

recent studies of the elastic properties of PE multilayer [13], we applied a layer-by-layer deposition approach (see chapter 3) to deposit a thin PE elastic shell on the surface of melamine formaldehyde microspheres. In our approach, the trapping of the microsphere in an optical tweezing setup was achieved with a tightly focused cw laser beam when the microsphere-emitter was placed on a glass substrate. Due to a strong difference in elastic properties of MF and the PE multilayer film [13], the radiation-pressure-induced deformation of the PE shell is the crucial factor controlling the WGM structure in the micro-PL spectra of the microcavity. The PE shell deformability was increased through contact of the shell with a salt-containing solution, which changes the mechanical properties of the PE multilayer (see chapter 3). We have chosen spheres with a diameter of 3 μm for our experiments. These spheres possess a large free spectral range between resonant WGM peaks that allows accurate identification of the polarisation and mode number of WGMs. The mode linewidth or quality factor Q is relatively unaltered by effects such as absorption by the CdTe nanocrystal monolayer [15]. We investigated the possibility of controlling the splitting of the WGM resonances in the nanocrystal-microcavity system by radiation pressure. The experimental approach of an all-optical microcavity deformation presented here should lay the groundwork for application of WGMs in spherical microcavities with an elastic shell for photonic applications. A mathematical model for fitting the resonance mode shape was developed, which verified the peak shape broadening and splitting as a result of the lifting of the azimuthal mode degeneracy.

5.2 Radiation pressure theory

Since the invention of the laser, moving and trapping of small particles with diameters from several nanometres into the millimetre regime raised more and more interest in physics due to the high intensities achievable with a tightly focused beam. Microscope objectives with high numerical aperture (N.A.) around 1 and greater can create a strongly focused Gaussian beam profile, providing an ideal source for optical trapping. Laser trapping was discovered experimentally by Ashkin et al. [16] for the first time.

The basic principle behind optical trapping is the momentum transfer between the object and the incident photon. A photon carries linear momentum $\vec{P} = \hbar\vec{k}$. When the photon is reflected or refracted at an interface between two media, the photon changes direction. This change corresponds to a change of the linear momentum of the photon. Due to the principle of conservation of momentum, the loss of the photon momentum is transferred to the interacting object. A small force F is therefore exerted on the particle corresponding to the momentum change ΔP over time Δt as given in the relation

$$F = \frac{\Delta P}{\Delta t}. \tag{5.1}$$

The applied force related to dielectric transparent spheres is divided into two components. The scattering force F_{scat}, caused by the light reflected on the sphere surface and the gradient force F_{grad}, originating from the momentum transfer of the photons refracted into the sphere. The scattering force points into the beam direction, pushing the sphere along the path of the beam. The direction of the gradient force depends on the focus position of the laser beam along the beam path (Fig. 1). It either points into the beam direction or in the opposite way. The gradient force also draws the sphere into the beam centre, due to the intensity gradient in the radial direction of the beam profile. When a laser is tightly focused on a sphere, the two forces along with the gravity force moves a loose sphere to an equilibrium point close the focus of the beam. The strength of the gradient force is proportional to the intensity gradient of the laser beam and therefore directly related to the N.A. of the

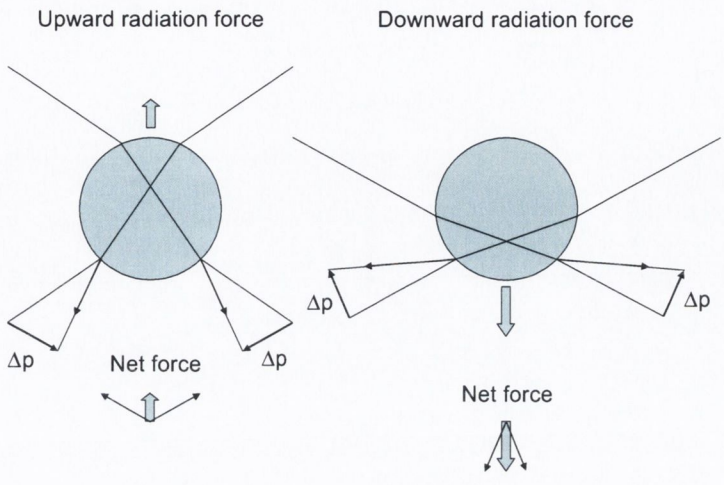

Figure 1. *Reverse and forward radiation pressure as a result of the gradient force. The momentum change Δp of the refracted beam is transferred to the particle.*

microscope objective which is used to focus the beam. The scattering force is proportional to the intensity of the laser beam. A higher photon density causes higher radiation pressure. Consequently, the strength of the scattering force shows a linear relationship with the laser intensity. It also depends on the position of the focus as the radiated surface area where the photons are reflected changes with the sphere position within the beam.

According to the size of the particle compared to the wavelength, the mathematical model to calculate the forces is either based on the Rayleigh scattering, where the particle size is assumed to be considerably smaller than the wavelength, or the Mie scattering where the particle size is comparable or bigger than the wavelength of the interacting light. The theoretical description of radiation force for the Mie regime is based on the Lorenz-Mie theory, which discusses the scattering of light by a spherical particle irradiated by a plane electromagnetic wave. To apply the formalism to a Gaussian shaped laser beam, an extension for the Lorenz-Mie theory was developed, called the generalised Lorenz-Mie theory (GLMT). The GLMT is valid for tightly focused laser beams, whose intensity profile does not correspond to a plane wave any more. Various beam shapes can be used in association with the Mie scattering for more accurate scattering models. An applicable approximation for a laser beam focused through a high N.A. microscope objective is a

Gaussian-shaped intensity gradient. The general equation for the radiation pressure cross section C_{pr} is defined as

$$C_{pr} = C_{ext} - C_{sca} < \cos\theta >, \quad ,$$

where C_{ext} and C_{sca} are the extinction and scattering cross sections, respectively. The asymmetry parameter $< \cos\theta >$ is the average cosine of the scattering angle. The above equation is derived by considering the momentum transfer of a stream of photons, incident on the spherical particle on an effective area dependent on the scattering angle [17]. Based on the GLMT, the radiation pressure cross section is given by [18]

$$\begin{aligned} C_{pr} &= \frac{\lambda^2}{2\pi}\sum_{n=1}^{\infty}\frac{2n+1}{n(n+1)}|g_n|^2\,\mathrm{Re}\left[a_n + b_n - 2a_n b_n^*\right] \\ &+ \frac{n(n+2)}{n+1}\mathrm{Re}\left[g_n g_{n+1}^*(a_n + b_n + a_{n+1}^* + b_{n+1}^* - 2a_n a_{n+1}^* - 2b_n b_{n+1}^*)\right] \end{aligned} \tag{5.2}$$

In this equation, g_n is the beam shape coefficient and a_n and b_n are the Mie scattering coefficients. The beam shape coefficient g_n specifies the beam type. It characterises a beam which differs from a simple plane wave. The variables with the superscript '*' represent the conjugate complex values. The actual radiation force is expressed by

$$F = \frac{2P}{c\pi\omega_0^2}C_{pr}, \tag{5.3}$$

where c is the speed of light, ω_0 the beam waist at the focus and P the output power of the laser. Four models exist to date to compute the beam shape coefficient for a Gaussian intensity gradient. The model of numerical evaluation of quadratures and the numerical evaluation of finite series [19], the localized approximation series [19-22] and the s-expansion method [22]. Among others, the localized approximation method permits fast and accurate computations for the evaluation of the beam coefficient. The beam shape for an on-axis Gaussian beam is given by [22]

$$g_n = \left(1 + i\,2s\frac{z_0}{\omega_0}\right)^{-1}\exp\left(ikz_0\right)\exp\left[\frac{-s^2(n-1)(n+2)}{1 + i\,2(sz_0/\omega_0)}\right], \tag{5.4}$$

where k is the wavenumber ($k = \frac{2\pi}{\lambda}$), z_0 the coordinate of the beam-waist centre, ω_0 the beam waist radius at the focus and s is a variable defined by $s = 1/k\omega_0$. Calculation of the Mie-coefficients is straight forward, as they are derived from the classical Lorenz-Mie theory, for example, discussed in [23] (see also chapter 2.4). We implemented a model for the radiation pressure based on this formalism with the software package Mathematica. The experimental parameters in this model are the size of the microsphere, the refractive index of the sphere material, the beam waist of the focus, and the output power and the wavelength of the laser beam. Assuming that the microsphere is excited perpendicular to the substrate from above in the vertical direction, the radiation force is calculated as a function of the focus position relative to the sphere centre along the z-axis. The radiation force scales linearly with the excitation power, as Eq. 5.3 shows. A high intensity gradient, corresponding to a high N.A. of the microscope objective results in an increased gradient force. The gradient force is responsible for lifting the sphere in the opposite direction of the laser beam path when focused vertically on the sphere placed on a plane substrate. The gradient force has to overcome the gravitational force due to the weight of the sphere. The electrostatic force between the sphere and the substrate is not negligible in our experimental setup where the spheres are placed on a glass or Si-substrate surrounded by air. The magnitude of the attraction depends on the charge of the sphere surface and the substrate itself. To completely lift the sphere from the surface, an initial force which overcomes the electrostatic attraction would be necessary, which is up to several times higher than the weight of a *3 μm* polymer sphere. Although we cannot lift the sphere completely with the available power and focussing arrangement, an upward force will cause a reduction of downward pressure on the sphere and a reduction of effects caused by the radiation pressure, such as deformation of the sphere or indentation of the substrate in case of elastic materials. Based on the formalism of the GLMT, we calculated the radiation force exerted on our *3 μm* spheres exposed to a focused Ar^+-ion laser beam at *488 nm* located in vertical direction perpendicular to the xy-plane of the plane substrate. The graphs in Fig. 2 shows the calculated radiation force versus the focus position relative to the sphere centre ($z = 0$). The focus moves on-axis along the z-direction through the sphere centre. Negative z-values correspond to a focus moving upwards, while positive z-values correspond to a

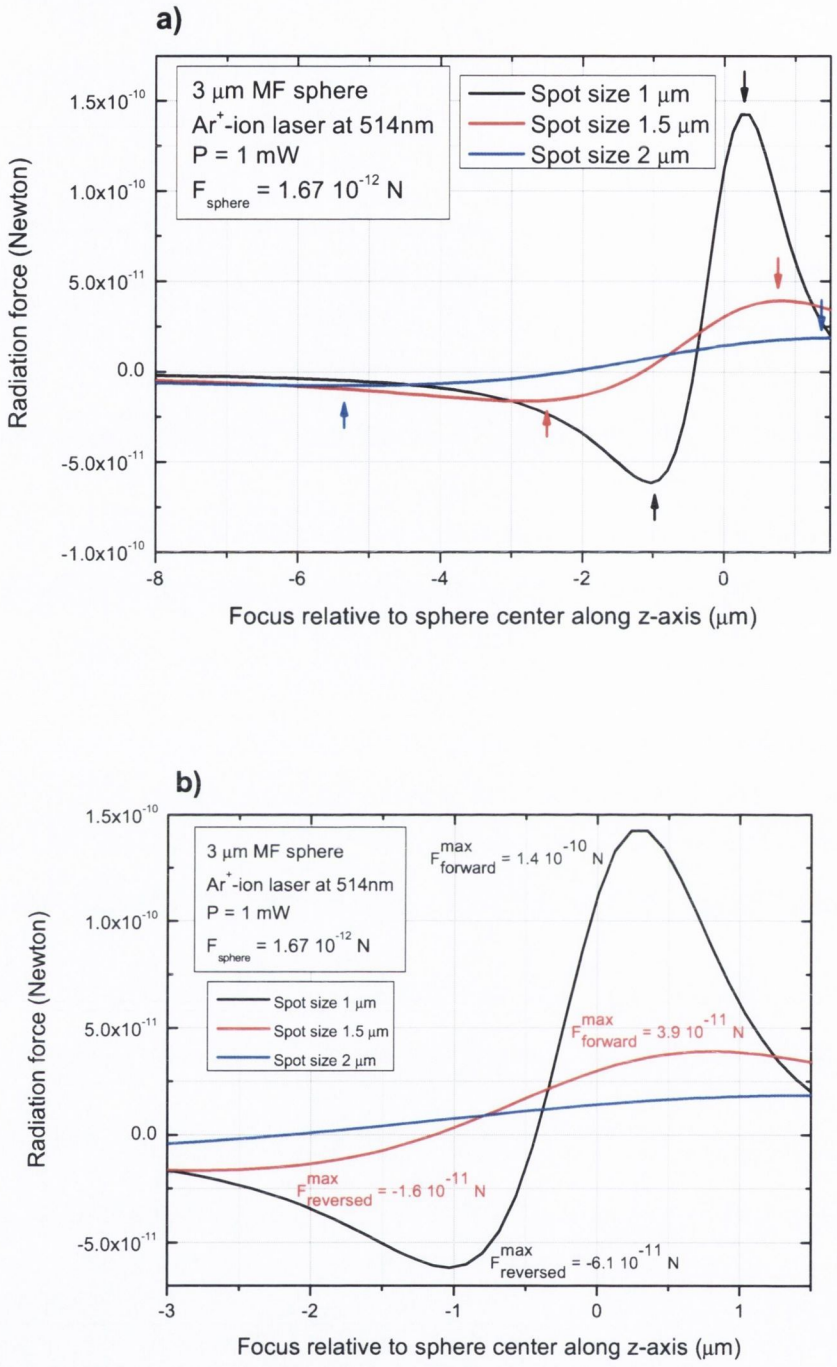

Figure 2. *Calculated radiation force as a function of the focus position along the z-axis. The sphere centre corresponds to z = 0. The calculation is carried out for a 3 μm sphere for 3 different spot sizes. Arrows in a) indicate the radiation force maxima, while the peak labels in b) give the magnitude of the maximum radiation force at the peak points.*

focus moving towards the substrate. As the radius of the sphere is *1.5 μm*, the substrate is located at $z = +1.5\ \mu m$. The radiation force scale on the y-axis of the graph shows positive and negative values. Negative radiation force represents an upward force in the opposite direction of the laser beam, while positive radiation force corresponds to a force in the beam direction. The graph demonstrates, that the focus position varies the balance between

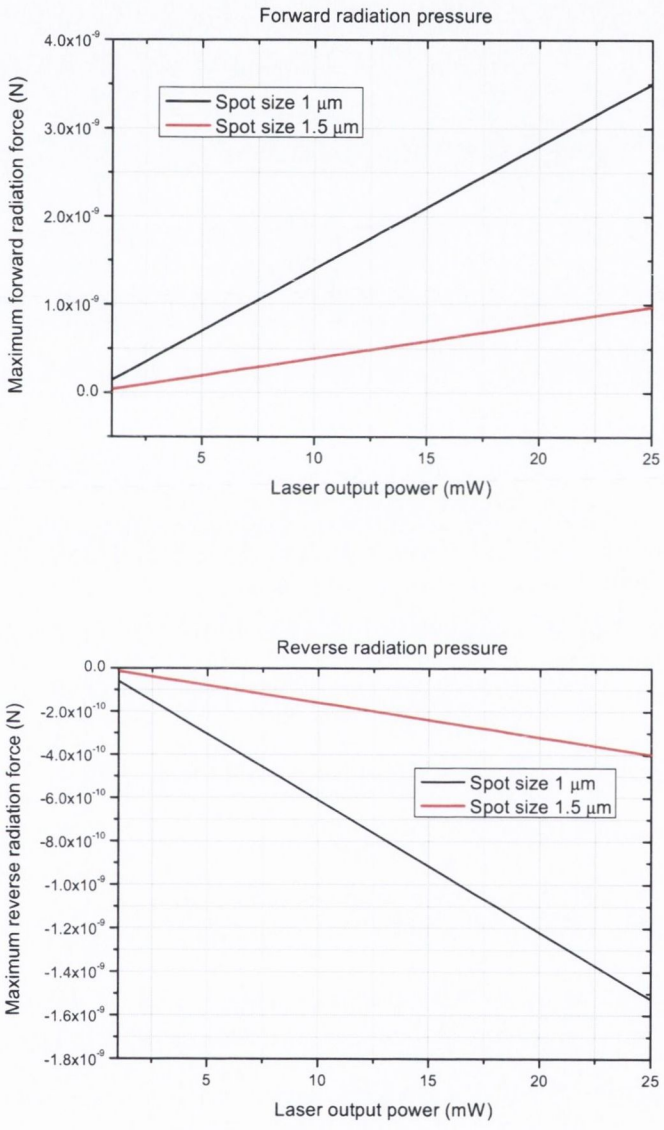

Figure 3. *Maximum forward and reverse radation pressure for 2 different spot sizes.*

the gradient force pulling the sphere in opposite beam direction and the scattering force, pushing the sphere into the direction of the laser beam. At the point of $F_{rad} = 0$, the two forces are in an equilibrium state. A loose microsphere would be trapped at this point within the focused beam. As our microspheres are placed on a substrate, no net radiation force is applied to the sphere when the focus is at this equilibrium point. Moving the focus further down towards the substrate causes a positive radiation force, while moving the focus from this point upwards causes a negative radiation force. The different graphs in Fig. 2 display the radiation force for different beam waists of the focused laser. The plots clearly demonstrate the strong dependency of the radiation force on the spot size. A decrease in spot size of the focused beam strongly increases the reverse as well as the forward directed radiation force exerted on the microsphere.

To estimate the radiation pressure, the spot size of the laser beam determined in our experimental setup during the experiment was taken for the calculations. To determine a optimum laser output power for the experiment, the weight of the *3 μm* melamine formaldehyde microsphere was calculated to about $F_{sphere} = 1.67\ pN$. To achieve a lifting effect, the reversed radiation force should be at least as high as the weight of the sphere $F_{rad} \geq F_{sphere}$. To determine the maximum forces at particular focus positions which can be applied to the sphere in both directions, the point of maximum reverse radiation force and the point of maximum forward radiation force for a spot size of *1.5 μm* and *1 μm* was determined from the graph (see arrows indication maxima in Fig. 2) and plotted as a function of the excitation power. Figure 3 shows the graphs of the maximum reversed and forward radiation force plotted as a function of the laser output power for the two different spot sizes. The theoretical calculations illustrate, that we can tune the direction of the radiation force by varying the focus position of the beam along the z-axis. This is achieved by changing the balance between the scattering force and the gradient force applied on the microsphere. When a focus position is selected, the applied magnitude of radiation force is tunable by the output power of the laser beam trap, which gives another degree of freedom for controlling the radiation force applied on the microsphere. Thus, we have two ways to control the radiation force. The theoretically required laser power depends on the size and the weight of the sphere. With the reversed radiation force, the weight of the sphere has to be overcome to reduce the pressure on the microsphere.

Adequate forward radiation pressure is required to deform the elastic shell to lift the azimuthal mode degeneracy induced by shape distortion of the microsphere with a soft-

shell. Due to absorption of the laser by the nanocrystals and the PE layer on the sphere surface, the real power which contributes to the radiation force is diminished. For a first-order estimation of the output power, the absorption was neglected because only one monolayer of CdTe nanocrystals was applied to the sphere surface. The calculation of maximum radiation force in the reversed and forward direction is carried out with the *488 nm* laser line of an Ar^+-ion laser. For radiation force in the beam direction a value of F_{rad} = *3.5 nN* for the *1 μm* spot size and F_{rad} = *1 nN* for the *1.5 μm* spot size can be achieved theoretically with a *25 mW* beam. A maximum reversed radiation force is determined to be F_{rad} = *1.5 nN* for the *1 μm* spot size and F_{rad} = *0.4 nN* for the *1.5 μm* beam waist with *25 mW* output power. The radiation force for both directions reaches the nano-Newton regime for the given laser power range and the selected sphere size of *3 μm*. While a certain power level is required to achieve the desired deformation and lifting effect, the intensity of the laser needs to be as low as possible at the same time to avoid fast degradation and thermal damage of the CdTe nanocrystals on the sphere surface. Irreversible thermal damage results in a quenching of the PL intensity and in the case of strong thermal damage a decrease of the *Q*-factor or a complete disintegration of the microsphere-emitter. The calculations in combination with the initial experiments were aimed to find a reasonable intensity regime for the microsphere-emitter samples where the shape distortion occurs with a resulting mode degeneracy lifting. Furthermore, the presented measurements will verify the focus-dependent and laser power dependent radiation force change which was observed by a characteristic change of the resonance mode shape and their spectral position.

5.3 Elasticity calculation of melamine formaldehyde spheres

To estimate the amount of power which is necessary to deform a MF microsphere of a particular size, calculations on the basis of the classical Hertz theory [24-27] were carried out. The theory provides solutions for the impact of elastic spheres and the resulting elastic deformation under normal contact force (P). The theory was also shown to be valid for contact between a sphere and elastic or rigid planar substrates for small deformations [24]. Our calculations aim at the evaluation of a potential deformation of the elastic MF microsphere in contact with a rigid substrate. In this experimental arrangement, the normal contact force corresponds to the radiation force applied by the tightly focused laser beam. The required parameters for the sphere are the Young's modulus E and Poisson's ratio ν of melamine formaldehyde. Young's modulus is a material property which is a measure for the elasticity of a material. It is the ratio of tensile stress to tensile strain at small distortions within the elastic limit and it can be determined experimentally. The unit of E is N/m^2. Poisson's ratio is given by the ratio of lateral strain to axial strain under the influence of axial tension. The ratio is dimensionless. For an estimation of the influence of radiation force on the MF sphere, the radiation force is defined as the normal contact load. The approximated representation of the radiation pressure deformation is a uniform pressure on the top of the sphere corresponding to the normal load force in the Hertz theory, pressing the sphere on the rigid substrate which causes an elastic deformation. The deformation of elastic microspheres is discussed in [24]. The equations based on the Hertz theory are taken from this publication. The plain strain modulus E' which is required for the calculations is given by

$$E' = \frac{E}{(1-\nu^2)} \quad . \tag{5.5}$$

During applied radiation pressure, the sphere centre approaches the solid substrate due to deformation of the sphere. The displacement of the sphere centre relative to the substrate is given by α_z. The relationship between contact force P and displacement α_z is given by

$$P = \frac{4}{3} R^{\frac{1}{2}} E' \alpha_z^{\frac{3}{2}} \quad . \tag{5.6}$$

Solving the equation to the displacement α_z results in

$$\alpha_z = \left(\frac{3}{4E'\sqrt{R}} \right)^{\frac{2}{3}} P^{\frac{2}{3}} \quad . \tag{5.7}$$

The displacement which corresponds to the deformation of the sphere axis in the polar direction shows a dependency to the power of *2/3* on the contact force *P*. The contact force is the radiation force in this experimental configuration. The following approximate data was determined from literature for melamine formaldehyde. Young's modulus is about $E = 6 \pm 2\ GPa$. Poisson's ratio is about $\nu_{MF} = 0.34$. The radius of the microsphere is $R = 1.5\ \mu m$. Using these values with Eq. 5.7 results in

$$\alpha_z = 1.7 \cdot 10^{-5} F_{rad}^{\frac{2}{3}}, \tag{5.8}$$

as the relationship of radius reduction and radiation pressure for a 3 μm melamine formaldehyde microsphere. The plot in Fig. 1 shows the deformation along the polar axis of the sphere depending on the radiation force in beam direction. For this plot, the maximum radiation force from the radiation pressure calculations was considered for a laser spot size of 1 micron. As shown in Fig. 2, the maximum forward radiation force *is* $F = 1.4\ 10^{-10}\ N$ at a focus position of $z = +0.3\ \mu m$. As the radiation force scales linearly with the laser output power, the sphere centre displacement can be described as a function of the laser output power. The graph in Fig. 4 shows the calculated sphere centre displacement which corresponds to the reduction of the sphere radius in polar direction perpendicular to the substrate. As the results indicate, the radiation force under these parameters is not enough to considerably deform the MF microsphere. The calculated deformation is in the pico-meter regime. To achieve deformation by optical radiation pressure, the calculation verifies, that a considerably softer elastic shell is required on the surface of the MF microsphere.

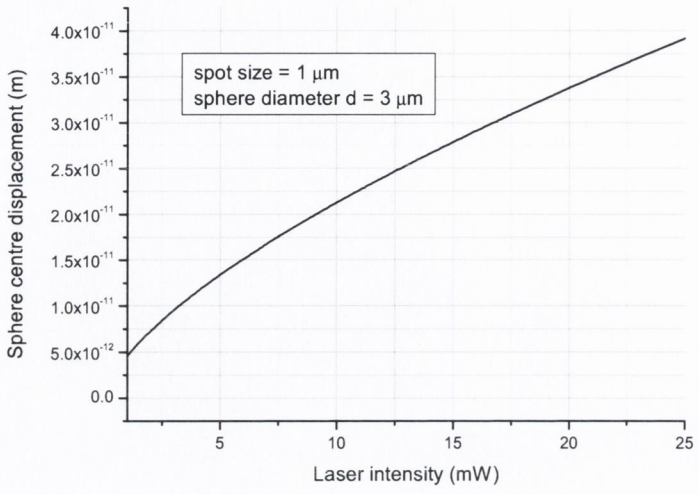

Figure 4. *Intensity-dependent sphere deformation in polar direction for a 3 μm MF sphere.*

5.4 Microsphere deformation and lifting of azimuthal mode degeneracy

For potential applications of microspheres in optical communications such as switches, add/drop filters or wavelength multiplexer, a frequency tuning mechanism for the optical resonances is desired when the resonances are utilised as channels in optical multiplexing. The resonance frequencies in microspheres are preselected mainly through the size of the sphere and the refractive index of the sphere material. Variations of these parameters make it possible to tune the WGMs within certain limits.

We adapted one particular method for our microsphere emitter, but with a new variation which was not subject of research in any work published to date. The idea is based on lifting the degeneracy of the azimuthal modes in a microsphere by all-optical shape distortion. The lifting of mode degeneracy can be caused by a deformation of the perfect spherical shape or through coupling of two microspheres into a photonic molecule [15]. The lifted degeneracy results in a splitting of the WGM resonances. Published work shows splitting and tuning of optical resonances due to strain deformation of a microsphere [12, 28]. Our novel approach is an all-optical deformation process. As spherical microcavities usually consist of a rigid material, the new method is based on depositing a soft shell onto the surface of the microsphere. The soft shell allows a distortion of the spherical shape of the microcavity by radiation pressure solely without any mechanical device to be in contact with the sphere. Radiation pressure is sufficient to deform the elastic shell, whereas deformation of the solid melamine formaldehyde sphere is not possible without mechanical strain. The relationship between sphere deformation and mode splitting was studied with the aim of controlled splitting of the optical resonances by radiation pressure. To apply a radiation force to the microsphere-emitter, the sphere was placed on a solid plane substrate and the laser excited the sample from a vertical position above the sphere. Forward radiation pressure pushed the sphere onto the substrate and consequently, the soft shell of the sphere which is in contact with the substrate is deformed. The light trapped inside the sphere is totally internal reflected at the boundary to the surrounding medium. Therefore, all modes which are situated in the distorted area of the sphere shell are affected. The fact that the deformation

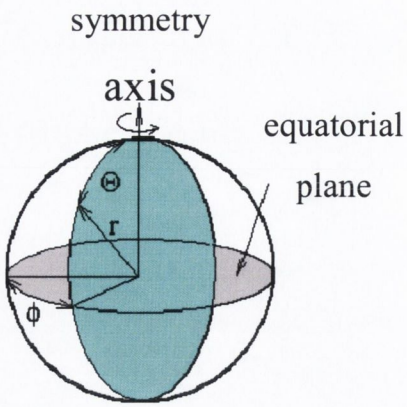

$$m = \ell \cos(\frac{\pi}{2} - \Theta)$$

Figure 5. *Defined angles in a microsphere to describe the location of the azimuthal resonance mode.*

is not uniform results in a more complex splitting than would be in a uniformly deformed microsphere. In this work, the effect of the non-uniform deformation was studied in relation to the resonance mode characteristics. In the following discussion, the consequences of oblate deformation of a sphere for the optical resonance characteristics in regards to the azimuthal mode degeneracy are presented. The WGMs are wavelength degenerate with respect to the azimuthal (m) modes due to the spherical symmetry of the microcavity. This means that orbits with various inclinations as shown in Fig. 5, described by various m-modes have the same pathlengths and consequently the same resonance wavelength. The cosine term assigns a particular inclination angle to each individual m - mode. The total number of azimuthal resonances depends on the angular mode number ℓ. The field distribution in the polar direction leads to an increase of azimuthal resonances with increasing ℓ. The modes are $2\ell + 1$ degenerate including the division into modes travelling in the opposite direction within the sphere. As there is no difference in the resonance frequency for modes travelling the same path in either clockwise or counter-clockwise direction, the degeneracy is reduced to $\ell + 1$ with m progressing from 0 to ℓ. The so-called fundamental mode $m = \ell$ is situated in the equatorial plane, the smallest azimuthal mode $m = 0$ is located perpendicular to the fundamental mode in the polar region as indicated in Fig. 6. Shape distortion breaks the azimuthal symmetry and results in a lifting of the degeneracy. In a deformed sphere, modes with various inclinations have different pathlengths and therefore, the spectral positions of m-modes are no longer equal

for all azimuthal modes. A single WGM peak in the spectrum of a perfect sphere is now split into a series of azimuthal resonances. In an oblate deformation, the sphere is elongated in the equatorial region which causes a red-shift of the azimuthal modes located in this region as shown in Fig. 7. The radius of the sphere in the polar region perpendicular to the equator is shortened and hence, the azimuthal modes in this region are blue-shifted with respect to the resonance wavelength of the undistorted sphere. In between these two points, the azimuthal modes travel along a circumference which decreases from the equator to the polar region resulting in a gradual shift of the azimuthal resonances. An analytic expression was derived by Perturbation theory in [29] for small shape distortions. The work is based on the first-order perturbation for the resonance frequencies in an open cavity system such as a spherical microcavity. The following equation provides an analytical expression for the frequency shifts and mode splitting for an oblate spheroid with small amplitude of distortion $e = (r_p - r_e)/a << 1$, where the polar and equatorial radii are r_p and r_e, respectively [29]:

$$\lambda_m(m,e) = \lambda_{l,n}\left\{1+\frac{e}{6}\left[1-\frac{3m^2}{l(l+1)}\right]\right\} \tag{5.9}$$

$\lambda_m(m, e)$ is the resonance wavelength of individual azimuthal mode depending on the ellipticity e and the azimuthal mode number m, $\lambda_{l,n}$ is the resonance wavelength for the undistorted sphere of radius a. The resonance wavelength of the lifted modes shows a square dependency on the azimuthal mode number m. Figure 7 is an illustration of the mode shift in the spectrum in relation to the deformation of the sphere radius. Increasing the deformation of the sphere leads to a stronger splitting and a higher free spectral range between the azimuthal modes, which increase quadratically with the mode number m. The

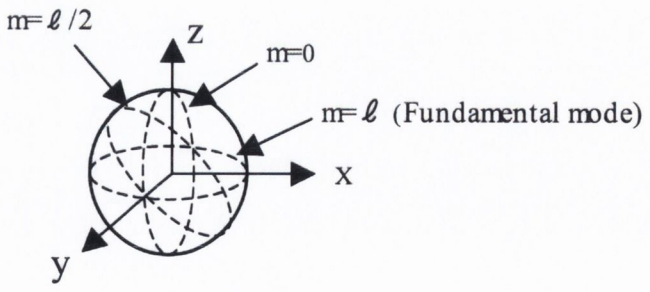

***Figure 6**. Spatial distribution of the azimuthal resonances in a perfect sphere.*

spacing between the modes is therefore not equal for all modes. This model refers to an oblate deformed spheroid particle. We initially approximate a uniform oblate distortion in the region where the soft shell of the sphere is compressed between the sphere core and the substrate. We expect that the modes in the undistorted region are not affected which is shown to be the case as discussed later in this chapter.

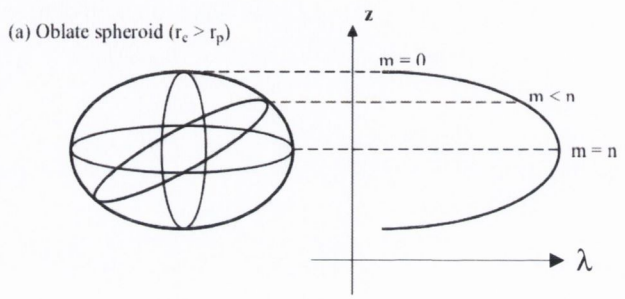

Figure 7. *Spatial distribution and wavelength shift of azimuthal resonances in an oblate spheroid.*

To realise a soft shell around the solid MF microsphere core, we applied PE multilayers on the surface as discussed chapter 3. The value of Young's modulus of PE LbL films (*100–200 MPa*) falls in the range characteristic for highly cross-linked rubber [14]. We achieved a reduction of solidity of the PE multi-layer by suspending the PE coated spheres into highly concentrated NaCl solution. A physically cross-linked network of PE molecules forms an elastic LbL shell on the surface of MF microspheres. As discussed in chapter 3, a chemical reaction decreases the number of cross links in the polymer which reduces the strength. Lower solidity requires less radiation force to deform the PE shell. In this new approach, an all-optical lifting of the mode degeneracy is intended in a controllable manner. In our experiments, we studied the possibility of revealing the azimuthal modes by radiation pressure controlled deformation of the soft PE shell. The experimental scheme is shown in Fig. 8. The microsphere is therefore placed on a solid substrate. Variation in the focus position along the z-axis either pushes the sphere on the substrate or lifts the sphere. As the electrostatic attraction to the substrate is highly dependent on the charge of the

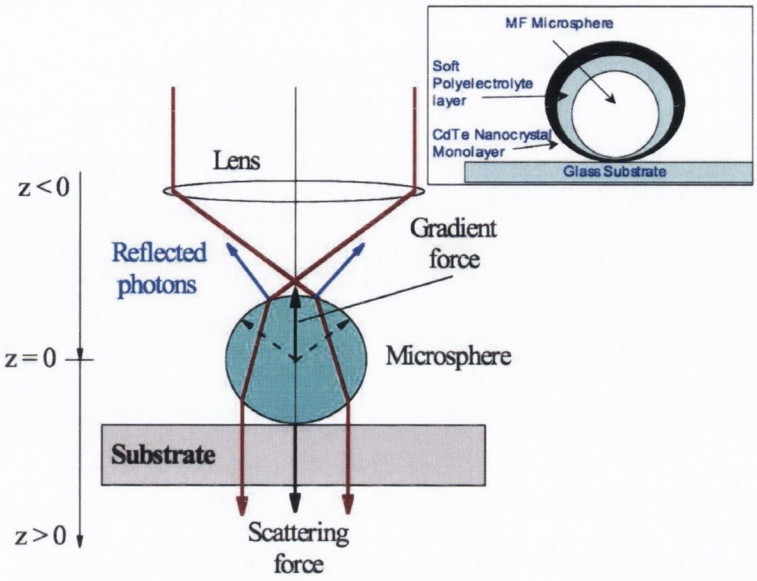

Figure 8. *Experimental scheme of the radiation pressure experiment.*

sphere surface and the substrate, complete lifting of the sphere from the substrate requires very high laser beam power which we cannot provide without instant damage to the microsphere-emitter. Nevertheless, we expect a reduction of downward pressure to a certain minimum where the sphere is pulled upwards, though it will still be in contact with the substrate. The upward radiation force causes an expansion of the compressed PE shell located between the sphere and the substrate due to a reduced pressure on the elastic shell within the distorted area. Consequently, it causes a decrease in the approximate oblate deformation. The inset in Fig. 8 provides a more detailed picture of the structural composition of the deformed PE shell under radiation pressure. The solid MF sphere core is surrounded by the soft PE multi-layer and one mono-layer of CdTe nanocrystals. Up to *12* PE single layers, corresponding to a shell thickness of about *15 nm*, are deposited on the surface of the sphere. The nanocrystal layer is the outermost layer (indicated in black in the inset graph of Fig. 8). The radiation pressure as well as the weight of the sphere deforms the soft shell where the sphere is in contact with the substrate. The upper area of the sphere is unaffected by the deformation. As illustrated in Fig. 7, azimuthal modes with low order numbers are located in the regime of deformation. Higher order modes are located towards the equator of the sphere. This leads to a frequency shift of the azimuthal modes located

around the distorted polar region, but not for the modes in the equatorial region. The solid MF core is not distorted as the calculations have shown in section 5.3. To analyse the mode characteristics, we take the PL spectrum of the light emitted from the microsphere under continuous radiation with an accurately positioned laser focus in the micro-PL setup. In the experiment, the variation of the output power as well as the variation of the focus position was investigated with respect to an observation of azimuthal mode splitting. The primary condition for optical trapping is a high intensity gradient of a laser beam, obtained by an objective with high numerical aperture (100x, N.A. = 0.9).

5.5 Radiation pressure dependence of focus position at constant laser intensity

Based on the calculated radiation force, we initiated a radiation force experiment with *3* μm MF spheres coated with *8* and *10* PE single- layers (*4* and *5* bi-layers), respectively and both coated with one monolayer of CdTe nanocrystals. The Renishaw micro-PL/micro-Raman machine was used to carry out the experiments. The setup offers a highly accurate positioning stage in the xyz-direction with *0.1* μm spatial resolution. The scattered light from the nanocrystals coupled into the sphere is collected through the microscope objective while the laser exerts radiation pressure on the sample. The advantage of this approach is the implementation of the same laser as excitation source for the nanocrystals and as the source for applying radiation force to the sample. This method lowers the complexity of such a setup, where no additional laser or mechanical equipment for shape distortion is required. The photo-induced emission from the nanocrystals allows us to detect the mode structure over a broad spectral range. No scanning with a laser is required to sample the resonance modes, which is a common practice in published work by other research groups to detect scattering from a passive microsphere-device. We therefore measure the dynamic response of the optical resonances to the applied radiation pressure under continuous excitation while we record the PL spectrum of the microsphere-emitter. The graphs in Fig. 9 show the spectra of a *4* PE bi-layer sample and a *5* PE bi-layer sample. In contrast to the *4* bi-layer sample, the *5* bi-layer sample is treated with a *7* molar NaCl solution for *5* days before the nanocrystal layer was applied on the surface. This reduces the solidity of the PE shell on the solid MF core as discussed in chapter 3. The PL spectra in Fig. 9 a) and b) were taken on the same sphere with a focus position of $z = -2.5$ μm, which is about *1* μm above the sphere and $z = +1.5$ μm (focus in the sphere centre) for the measurement in b). According to the calculated radiation force in relation to the focus position along the z-axis (Fig. 2), the laser beam causes an upward radiation force exerted on the sphere at a focus

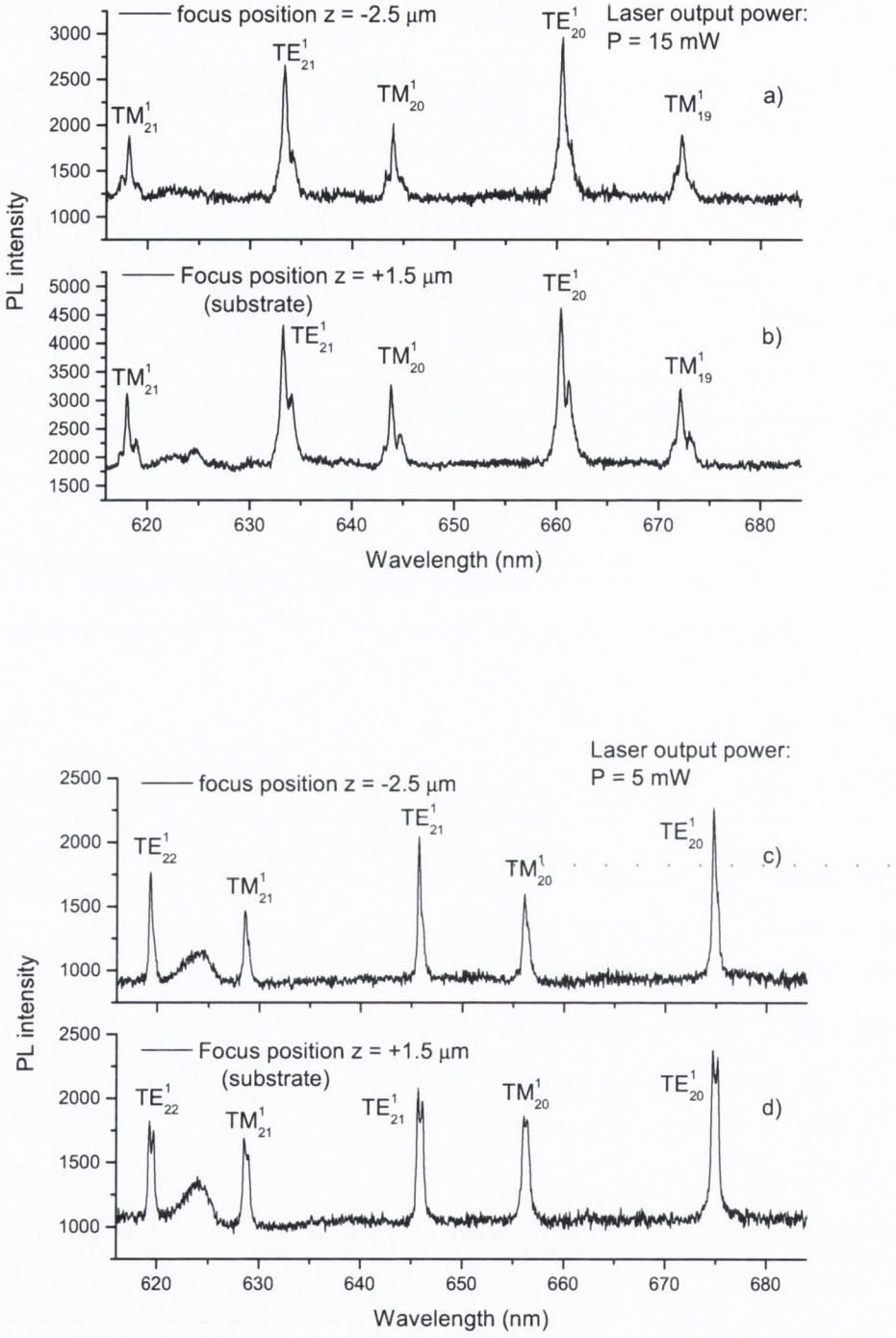

Figure 9. *PL spectra of microspheres while trapped in a cw laser beam under radiation pressure. (a) and (b) Same microsphere sample (4 bi-layers), excitation power P = 15 mW taken at different focus positions. (c) and (d) Another microsphere sample (5 bi-layers) modified with a salt solution and taken at considerably lower excitation power P = 5 mW, also at different focus positions.*

position of $z = -2.5\ \mu m$. For small microspheres, the position and polarization of the WGM can be easily determined by calculation of the scattering cross section or solving equations for the denominators of the scattering coefficients [19] of the Lorentz-Mie theory. Thus, the stronger peaks in Fig. 9 were identified as TE modes, whereas the smaller peaks observed in the micro-PL spectra are TM modes. The TE and TM resonances were identified by the angular mode number ℓ (subscript number) and the radial mode order n (superscript number) in the spectrum. The angular mode number is necessary to determine the spectral mode positions for each azimuthal mode individually (see Eq. 5.9). All peaks in the spectrum of Fig. 9 a) show a clear indication of peak broadening for both, TE and TM polarised modes. This broadening provides evidence that the PE shell of the sphere already experiences deformation. The radiation pressure at $z = -2.5\ \mu m$ is lifting the sphere according to the calculated radiation force. The experimental beam focus waist is about $1.5\ \mu m$. The theoretical analysis (Fig. 2) give a radiation force of about $F_{rad} = -1.6\ 10^{-11}\ N$ for $1\ mW$ beam intensity. Multiplied by 15 due to the linear scaling of the radiation force with power, the theoretical optimal radiation pressure is about $F_{rad} = -2.4\ 10^{-10}\ N$ at $15\ mW$ laser output power.

There are several physical effects which reduce the real radiation pressure exerted on the microsphere. At first, the absorption was neglected for the calculated radiation force. Absorption on the sphere surface reduces the gradient force which is a result of the light refracted into the sphere. Also the light coupled into the WGMs of the microcavity does not contribute to the gradient force. Optical interaction between the substrate and the microsphere can have an explicit effect on the focus-dependent radiation force [31]. Due to these non-ideal conditions, the sphere is not lifted sufficiently to decrease the deformation of the elastic PE shell completely. When focused on-axis on the substrate ($z = +1.5\ \mu m$), a second peak which is slightly red-shifted with respect to the original mode is now clearly observed (Fig. 9 b)). As the theoretical considerations predict, splitting towards the longer wavelengths is expected. This is in agreement with the resonances in the measured spectrum which show peaks with a red-shifted second peak arising within the broadened resonant modes. Due to a rearrangement of the azimuthal modes, a double-peak structure developed. Focusing on the substrate reverses the radiation force which now points into the beam direction. The modified mode-shape characteristic suggests that the downward pressure creates an increased deformation of the soft PE layer and consequently, an increased splitting of the modes in the distorted region of the microsphere. A perfect oblate

deformation would decrease the equatorial region in the sphere, causing a blue shift of the azimuthal modes within this region. The measurements show no visible indication of a shift of the peaks

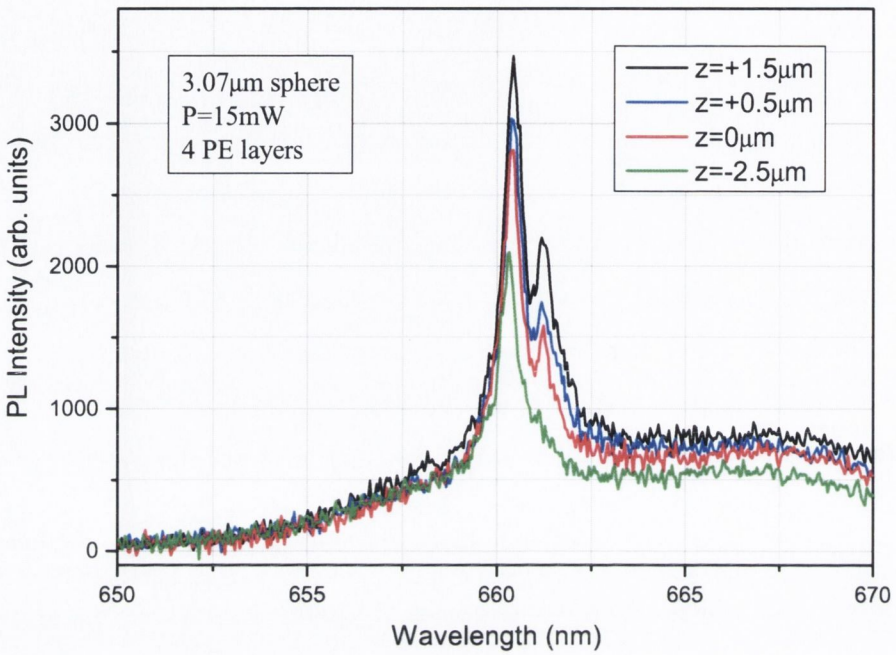

Figure 10. *TE mode of the PL spectrum in Fig. 8 b) for 4 different focus positions.*

towards shorter wavelengths. This is in agreement with the prediction, that the soft shell experienced no change around the equatorial region as the radiation. Radiation pressure induces compression of the PE shell in the region near the contact point with the substrate only. Though, the resonance frequencies of the equatorial modes remain unchanged. The double peak structure of the resonances that emerges when the radiation pressure in the beam direction is increased clearly supports our view of the shell distortion. A single TE mode selected from the spectrum in Fig. 9 b) is shown in the graph in Fig. 10. It shows 4 different measurements taken at 4 different focus positions to illustrate the gradual development of the peak shape under varying radiation pressure. The black curve corresponds to the double-peak resonance when the beam is focused on the substrate. At this point the theory predicts a forward radiation force, pressing the sphere towards the substrate. The blue curve which represents the measurement at $z = 0.5\ \mu m$, predicts a

reverse radiation force. The measurement still shows a peak broadened towards the red-shifted region. That means that the modes are still split due to deformation, although the radiation pressure is lifting the sphere. Two reasons for that have to be considered. On the one hand, the real spot size also possesses an elongated waist diameter along the z-axis, while the calculation only considers a lateral spot distribution. As a result, the laser beam refracted into the sphere in different depths can cause a slightly changed behaviour of the real radiation force in comparison with the calculations under perfect conditions. Therefore, a forward radiation force at $z = 0.5\ \mu m$ is still possible. On the other hand, interference caused between the substrate and the sphere when the focus is close to the substrate can modify the radiation force characteristics [31]. The resonance peak of the measurement with $z = 2.5\ \mu m$ shows a decreased broadening while the second red-shifted peak vanished completely. This is in agreement with the theoretical prediction, that a reverse radiation force lifts the sphere which leads to a reduced deformation of the PE shell in contact with the substrate and consequently a collapse of the azimuthal resonances.

The spectra shown in Fig. 9 c) and 9 d) were taken with the *5* bi-layer sphere. The PE layer is softened in a *7* molar NaCl solution before being coated with CdTe nanocrystals. Compared with the sphere used in the measurements of Fig. 9 a) and 9 b), this sphere has one additional bi-layer of PE and the whole PE shell is softer due to the NaCl treatment. The softening of the deformable PE shell in this measurement is clearly noticeable when considering the excitation power of the laser beam. The beam power was reduced from *15 mW* to *5 mW*. Nevertheless, the effect of radiation pressure on the WGM line-shape was found to be even more pronounced for the MF microsphere with *5* bi-layers of PE (Fig. 9 c) and 9 d)). The spectrum shows double-peaks with almost equal intensities. When the laser is focused on the substrate ($z = +1.5\ \mu m$), a second peak arises slightly red-shifted from the original peak in the same way as we observed in the PL spectrum of the previous microsphere-emitter sample. No further peak broadening is observed towards shorter wavelengths, in agreement with the undistorted equatorial modes which experience no frequency shift. As in the previous measurement, the double-peak structure developed when the focus was located on-axis on the substrate level, corresponding to radiation pressure in the beam direction. A qualitative comparison of the linewidth in the previous measurement with the *4* bi-layer sphere and the *5* bi-layer sphere measurements reveal a broader peak in the spectrum of the *4* bi-layer sample. This can be explained by the high laser intensity of *15 mW* in comparison with the *5 mW* in the measurements in Fig. 9 c) and

9 d). Although the elastic shell is softened for the measurements in Fig. 9 c) and d), the three times higher laser intensity probably produces a stronger deformation of the PE shell which results in a wider separation of the azimuthal modes noticeable as a peak broadening. The measurements at lower output power (Fig. 9 c) and d)) reveal a smaller linewidth but with a second red-shifted peak with almost the same intensity as the original peak. The shape of the resonance modes cannot clearly be correlated with the laser output power without a more detailed analysis of the shape in regards to the superposition of the azimuthal modes in the distorted spheroid. For further analysis, a model was developed to analyse the peak shape of the resonances in regards to a non-uniform distortion, which was considered when modelling the azimuthal mode distribution. Before discussing the resonance shape model, the intensity dependent mode splitting at constant focus position is discussed in the next section.

5.6 Radiation pressure as a function of laser intensity at constant focus position

When the focus position of the laser beam is kept constant, the balance between the scattering force and the gradient force is also fixed. That means that the force exerted on the sphere is either pointing in the beam direction or in the opposite direction of the laser beam, depending on the distribution of the ratio between the gradient force and the scattering force. The strength of the net force can still be tuned linearly by the output power of the excitation laser. As a further demonstration to verify the radiation pressure effect, we have studied the spectrum of a single sphere at a constant focal position $z = -1.7$ μm for two different laser beam intensities (Fig. 11). The first spectrum was taken at $P = 15$ mW laser output power, the second one at $P = 2.5$ mW. According to the calculations,

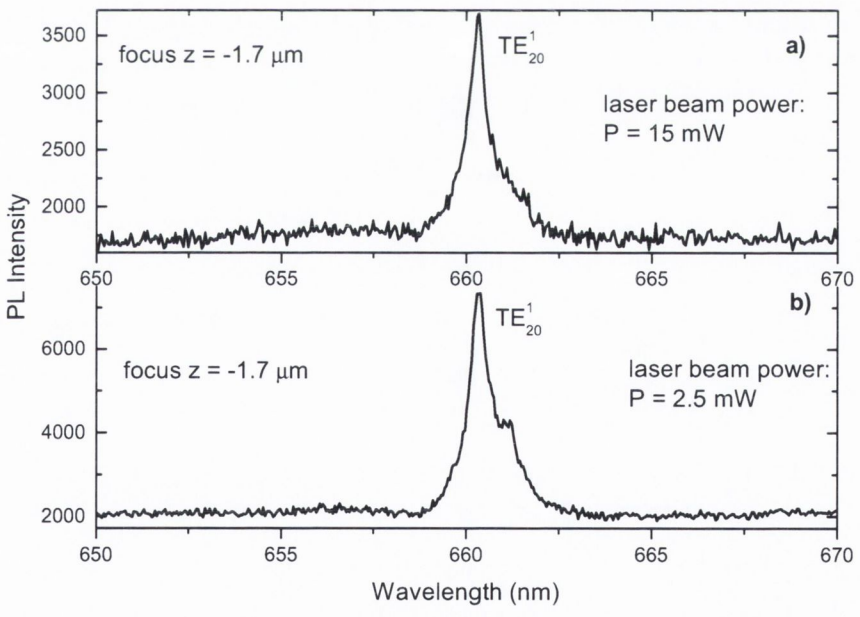

Figure 11. *TE resonance mode of a PL measurement at constant focus with varying laser output power.*

the radiation force is directed upwards in the opposite direction of the laser beam at a focus position of $z = -1.7\ \mu m$ (see Fig. 2). Under these experimental conditions an increase in radiation power causes an increase of the reverse radiation force. The tightly focused beam lifts the sphere further up which reduces the pressure on the soft shell and therefore reduces the deformation of the compressed region of the PE layer in contact with the solid substrate. As a result, the azimuthal splitting should be decreased in comparison with the lower laser output power. This effect is clearly visible in Fig. 11. The resonance peak at lower excitation power (Fig. 11 b)) developed an enhanced plateau towards longer wavelengths. This indicates an increased splitting due to the shifted azimuthal modes located in the distorted region of the microsphere. As demonstrated in Fig. 11 a), the resonance mode at *15 mW* output power shows a less pronounced red-shifted plateau, as a result of the reduced shell deformation by lifting the sphere.

Comparing this measurement with the measurement of the variation in focus position at constant laser output power, we observe less variation in the peak shape of the optical resonances. The effect of radiation force shows more impact on the resonance modes when tuning the focus position instead of the laser intensity. This behaviour is plausible when we consider the difference in how the two methods affect the balance between the gradient and the scattering radiation force. The variation of laser intensity only changes the magnitude of the radiation force exerted on the sphere while the balance between the gradient and the scattering force is changing the direction of the force which is balanced by the focus position. Therefore, the tuning of the focus along the z-axis produced a stronger variation in the shape of the resonance mode due to the rearrangement of the azimuthal modes by shape distortion. The variation in laser intensity at two different focus positions with gradually increased power is shown in Fig. 12 and Fig. 13. The intensity steps in the series of measurements illustrate the development of a plateau towards longer wavelengths when the output power is reduced and hence the sphere distortion is increased. When the laser is focused on the substrate within the sphere at $z = +1.5\ \mu m$, the radiation force is pushing the sphere

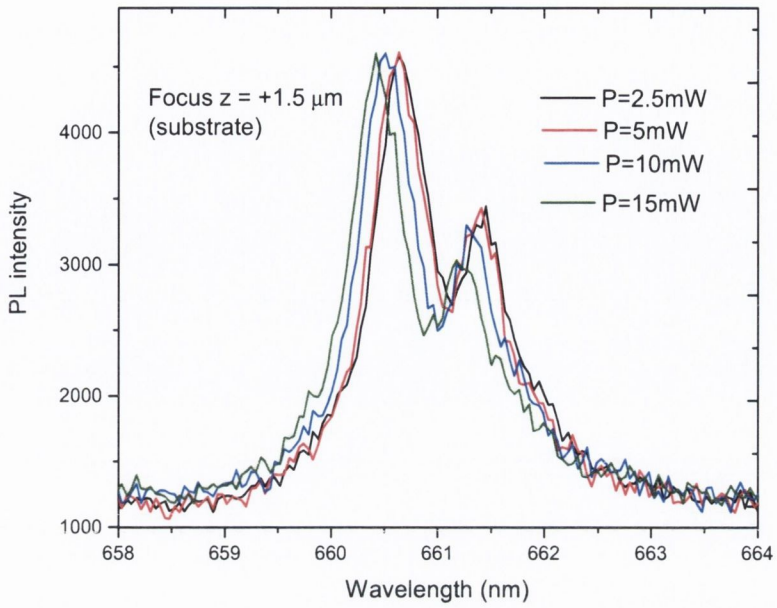

Figure 12. *TE mode of PL measurements at constant focus with variation in laser output power.*

downwards. The graphs in Fig. 12 corresponding to different laser intensities show, that the peak shape does not show considerable change with the variation of the output power of the laser. We attribute this observation to the fact, that the radiation force at this focal spot position with an initial output power of *2.5 mW* already induces a strong deformation of the soft PE shell to the elastic limit of the material. A further increase of the laser intensity which increases the radiation pressure on the sphere towards the substrate does not result in a stronger distortion of the PE shell. This measurement illustrates that a reasonable intensity range is required to modify the splitting of the azimuthal modes. It is also in agreement with our calculations that predict a forward radiation pressure when the laser is focused on the substrate. If the sphere was lifted at this focus position, the shape of the mode would change as in Fig. 11.

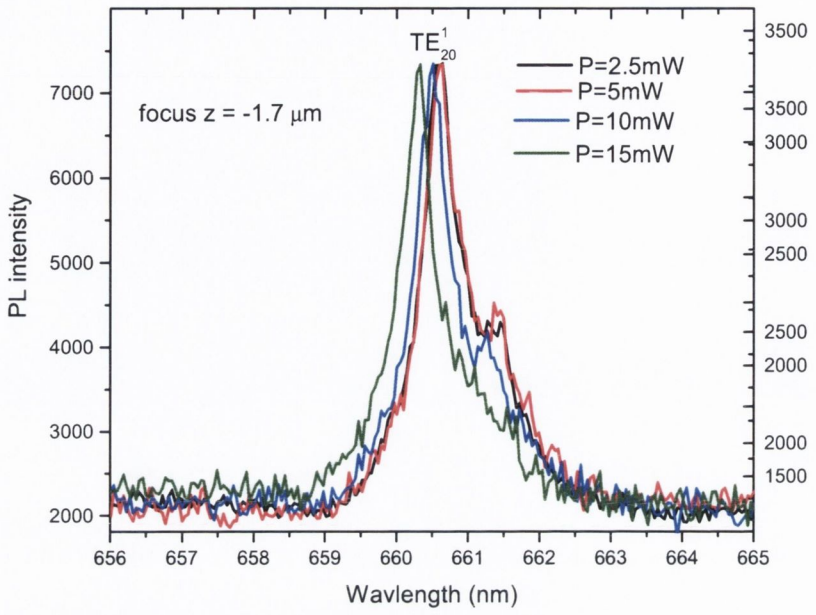

Figure 13. *TE mode of PL measurements at constant focus with variation in laser output power.*

For comparison with reversed radiation pressure, the plotted graphs in Fig. 13 correspond to a variation of the laser intensity at a focus position above the microsphere at $z = -1.7\ \mu m$. The plot shows the exact same resonance peak of the PL spectrum taken on the same microsphere sample. The focus was lifted to a region of reverse radiation force. The increase of the laser power from $P = 2.5\ mW$ to $P = 15\ mW$ demonstrate the gradual development of the red-shifted plateau composed by the split azimuthal peaks.

Apart from the modification of the peak-shape by radiation force, another effect of the irradiation on the resonances is clearly visible in the intensity dependent plots in Fig. 12 and Fig. 13. The resonances experience a blue-shift with increasing laser intensity. The mode shift is possibly caused by a heating effect of the microsphere during excitation with the laser. This particular behaviour is discussed in detail later in section 5.8. For now, the analysis of the peak shape characteristics due to radiation pressure is continued with the mathematical description of modelling the superposition of the azimuthal resonances in a deformed spheroid. This model gives more specific insight to the dependency between the

shape of the resonances and the magnitude of shape deformation. We developed a new model, which demonstrates the correlation between the double-peak structure of the resonances under radiation pressure and the number of azimuthal modes involved in the mode splitting caused by shape distortion of the PE shell. The mathematical model also indicates the extension of the shell distortion in polar direction by the determination of the inclination angle of the azimuthal resonances shifted by shell deformation.

5.7 Modelling of the whispering gallery mode shape

The analytical equation to determine the spectral position for each resonance mode with higher azimuthal order is given in Eq. 5.9. The free spectral range depends mainly on the ellipticity of the deformed spherical particle. The spectral positions of the modes arrange quadratically with the azimuthal mode order which results in a parabolic increase of the free spectral range. We developed our beam shape model on the basis of the analytical equation for the mode position of the perturbation theory for small changes. For the mode splitting, we assume a uniform deformation as a first-order approximation of the measurements. The individual WGMs will be represented by Lorentzian-shaped peaks. Each peak corresponds to an azimuthal mode. The Lorentzian mode is given by the function

$$F_{Lorentzian} = \frac{I \cdot \Delta\lambda_{FWHM}}{(\lambda - \lambda_m)^2 + \left(\frac{1}{2}\Delta\lambda_{FWHM}\right)^2} \quad , \tag{5.10}$$

where I is the amplitude of the peak, $\Delta\lambda_{FWHM}$ the linewidth and λ_m the wavelength of an individual azimuthal mode with the mode order m. The spectral position is determined with the equation (Eq. 5.9)

$$\lambda_m(m,e) = \lambda_{l,n}\left\{1 + \frac{e}{6}\left[1 - \frac{3m^2}{l(l+1)}\right]\right\} \quad . \tag{5.11}$$

The shape of a distorted spherical particle is then approximated by the superposition of the azimuthal modes replaced by a Lorentzian-shaped peak. That leads to the following equation

$$F(\lambda,m,e) = \sum_{m=0}^{l} \frac{I \cdot \Delta\lambda_{FWHM}}{(\lambda - \lambda_m)^2 + \left(\frac{1}{2}\Delta\lambda_{FWHM}\right)^2} \quad , \tag{5.12}$$

which represents the superposition of the splitted azimuthal mode in an oblate spheroid. The variables are the ellipticity e, the azimuthal mode number m and the individual

wavelength $\lambda_{l,n}$ of the degenerated resonance mode in a perfect spherical particle with angular mode number ℓ and radial mode order n. As our samples experience a deformation of the soft shell while the solid MF sphere core is not affected, this model is modified to cover the changed conditions. The PE shell on the sphere surface is deformed around the contact point with the solid substrate. The frequency shift of the azimuthal modes originates from the varying inclination of the beam path of each individual mode in the sphere when we consider the ray optics regime. The azimuthal modes in the polar region interact with the deformed shell regime which induces a mode shift. Modes with higher azimuthal mode order located near the equatorial region will not interact with the distorted region. Consequently, the resonances do not experience a shift but still remain at the degenerate resonance frequency in a perfect spherical shape. For this reason, the beam shape model was convolved with a Lorentzian peak with the resonance frequency of the undistorted sphere. Many of the azimuthal modes around the equator of the sphere experience no shift but still contribute a peak to the spectrum. The formula in Eq. 5.10 is therefore extended with another Lorentzian peak, leading to the equation

$$F(\lambda) = \frac{I_0 \cdot \Delta\lambda_{FWHM}}{(\lambda - \lambda_0)^2 + \left(\frac{1}{2}\Delta\lambda_{FWHM}\right)^2} + \sum_{m=0}^{l} \frac{I \cdot \Delta\lambda_{FWHM}}{(\lambda - \lambda_m)^2 + \left(\frac{1}{2}\Delta\lambda_{FWHM}\right)^2}. \qquad (5.13)$$

The first term in this formula corresponds to the degenerate resonance frequency λ_0 with the peak amplitude I_0. The second term is the sum of all azimuthal peaks due to distortion. In an oblate spheroid the increasing elasticity would split the degenerated resonance mode into a number of azimuthal peaks, while the original peak would vanish. Our model adds the original resonance frequency as a contribution to the non-uniformity. Two modes were chosen from the experimental data to fit the beam-shape model to the measured peak, taken under radiation pressure. The experimental and modelled peaks are shown in Fig. 14 and Fig. 15. The resonances are the TE_{20}^{1} mode of the spectrum in Fig. 9 b) and the TE_{21}^{1} mode of the spectrum in Fig. 9 d).

The linewidth of the resonances which was estimated to be $\Delta\lambda = 0.3\ nm$ ($Q \approx 2200$) and the original resonance wavelength λ_0 were taken from the experimental data to model the WGM line-shape. The linewidth was approximated from the peak at the reverse radiation pressure in Fig. 9 a) and Fig. 9 c). In a first order approximation, the linewidth of all

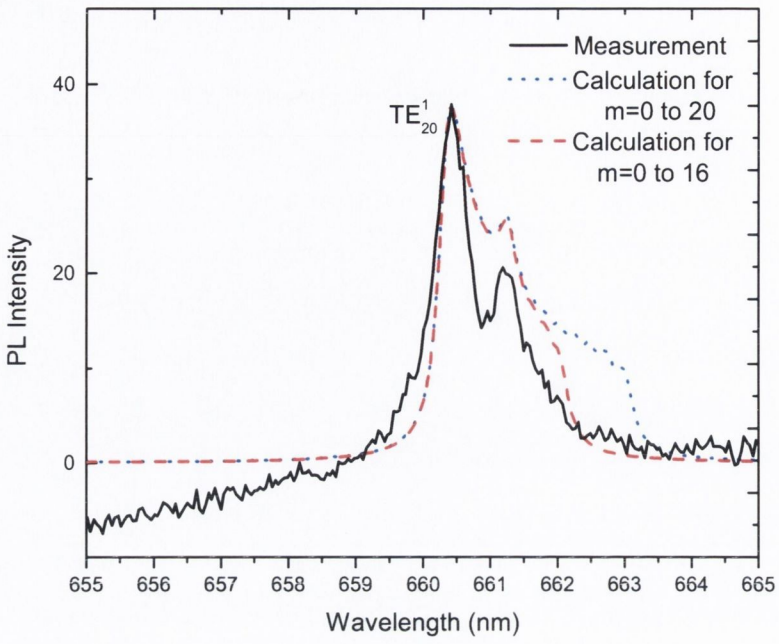

Figure 14. *Measured and modelled TE resonance mode.*

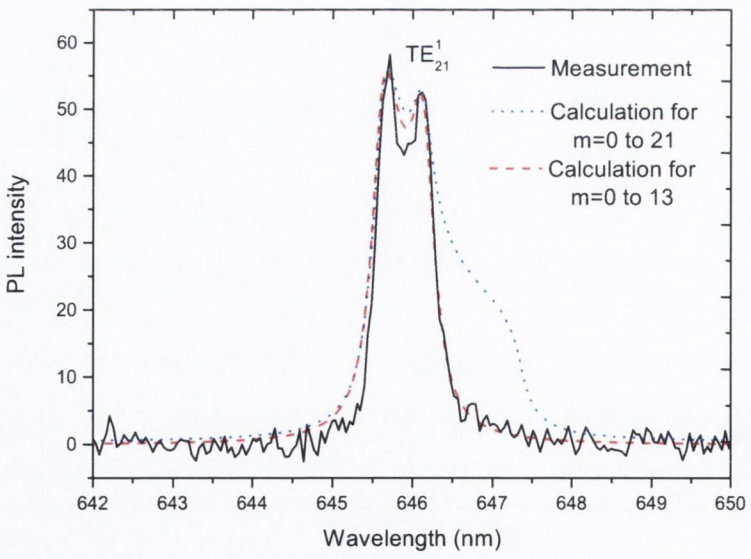

Figure 15. *Measured and modelled TE resonance mode.*

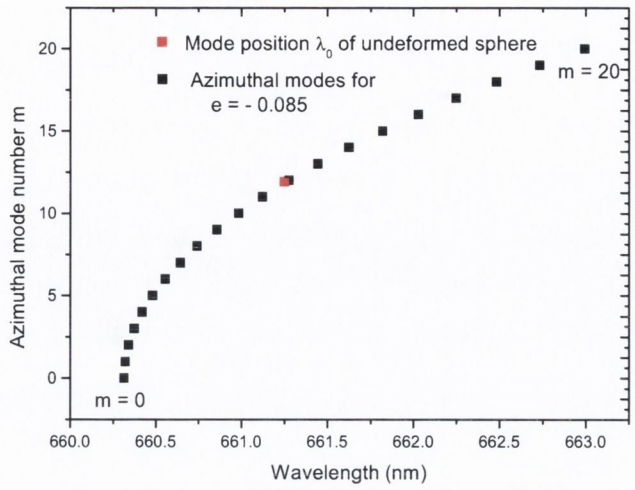

Figure 16. *Calculated azimuthal mode positions for the resonance peak in Fig. 14.*

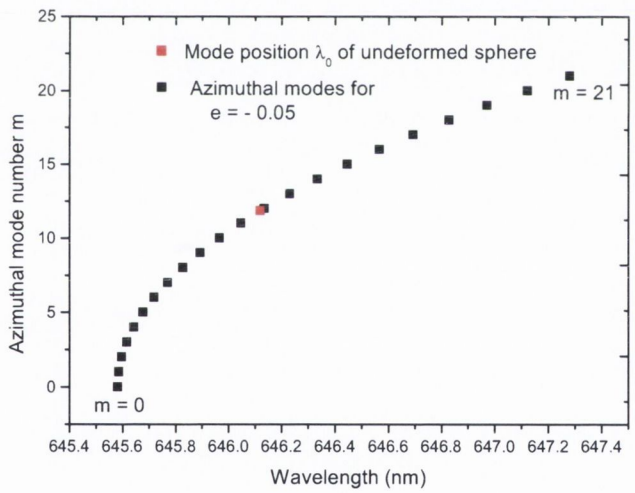

Figure 17. *Calculated azimuthal mode positions for the resonance peak in Fig. 15.*

azimuthal modes is considered to be the equal. The peak amplitude was also taken as equal for all azimuthal modes. Both graphs show the original measured peaks and the modelled peak consisting of a superposition of the azimuthal resonances with mode numbers from *0* to *m* as stated in the plot. The two modelled graphs in Fig. 14 show the mode fit for a

calculated superposition of the azimuthal modes $m = 0$ to 20 and $m = 0$ to 16 for the TE_{20}^{1} mode. The modelled graphs in Fig. 15 show the azimuthal modes $m = 0$ to 21 and $m = 0$ to 13 for the TE_{21}^{1} mode. The fit corresponds very well to the principle shape of the resonance mode. The double peak structure is indicated in the model as well as the tail towards the longer wavelengths. A plot which includes the azimuthal modes from 0 to 13 produces an almost perfect conformance with the experimental peak structure. The plateau which emerged from the higher order m-modes is not found in the experimental data. This result agrees very well with theoretical considerations in regards to the deformation characteristics of the soft PE shell. Modes with high azimuthal mode number m are located outside the distorted area close to the equatorial region of the sphere. The fact that these modes do not appear in the experimental data allows two interpretations. On the one hand, it can confirm, that there is no frequency shift of the azimuthal modes with high mode numbers as predicted in our theoretical discussion where we conclude, that there is no sphere distortion towards the equatorial region of the microsphere as expected when deformation only takes place in the elastic shell. On the other hand, the possibility exists, that we just do not excite the equatorial modes due to the tight focus and the free beam coupling in the centre of the sphere, although the sphere is distorted in the equatorial region. The free beam coupling technique with the tightly focused beam results in a strong focus dependency for the coupling efficiency of different azimuthal modes, because beams which are incident to the curved surface near the equatorial region of the sphere are more likely to be refracted through the sphere instead of coupled into the high azimuthal modes (Fig. 18). As this focus excitation configuration was not modelled yet in this work, it is an assumption based on ray optics. Due to our prior calculations of the stability of melamine formaldehyde spheres and the higher elasticity of the PE shell by several orders, we conclude that the equatorial region is not distorted and therefore, no higher azimuthal modes develop during excitation under radiation pressure. That means, that although the ray optics approach in Fig. 18 provides the possibility of focus dependent mode coupling, we can rule out the assumption, as the radiation pressure is not intense enough to deform the whole sphere.

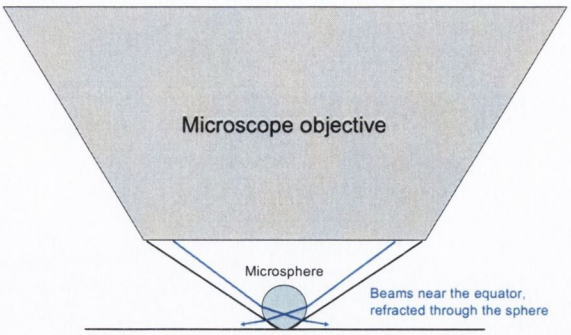

Figure 18. *Microsphere in a tightly focused laser beam. The focused light near the equatorial region is more likely to be refracted through the sphere, than coupled into the high m azimuthal modes.*

The line-shape fit in Fig. 14 also shows good agreement with the experimental peak. The azimuthal high m-modes plateau extends further into the red region in the calculation than in the measurement, also indicating an undistorted equatorial region of the sphere. As in the line-shape fit of the previous peak.

To describe how the modelled peak develops from the superposition of the Lorentzian peaks, the spectral positions of the azimuthal resonances for the two modelled peaks are plotted in Fig. 16 and Fig. 17. The azimuthal resonances are determined with Eq. 5.11. The red square in each graph corresponds to wavelength of the resonance mode λ_0 of the undistorted sphere. The wavelength plot for all azimuthal modes illustrates the m^2 - dependency of the resonances. With increasing m, the free spectral range between the modes increases quadratically. Each azimuthal mode in the model is represented by a Lorentzian peak. A plot of all individual Lorentzian peaks for the modelled resonances is shown in Fig. 19 and Fig. 20. The graphs show the overlapping modes. The Lorentzian peak in red corresponds to the unsplitted resonance mode of the perfect sphere. The superposition of all individual peaks results in the modelled peak shape in Fig. 14 and Fig. 15. The line-shape fit reveals a good qualitative agreement with the experimental data. That shows that the resonances are broadened by a lifting of the azimuthal mode degeneracy. A comparison of the measured peak with calculated peak shape suggests that the mode splitting is a result of a non-uniform deformation of the soft PE shell on the solid MF sphere core. The double-peak structure is formed by the overlapping azimuthal peaks

and the resonance peak of the original resonance mode of the undistorted sphere. The modified peak-shape model supports our theoretical approach to describe the double-peak. The model can be improved when the

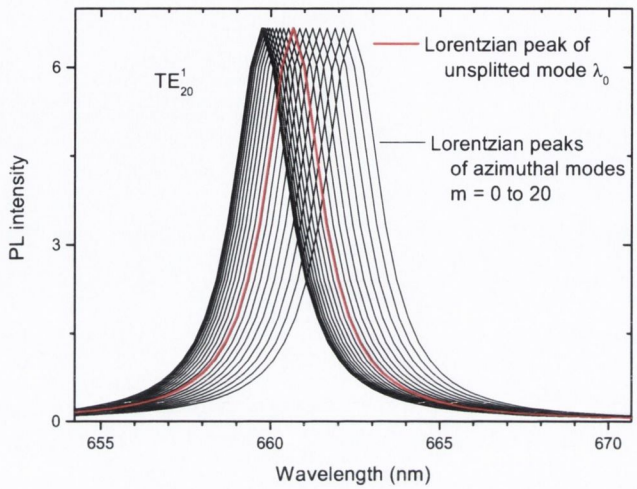

Figure 19. *Plot of all individual azimuthal modes which result in the modelled peak of Fig. 14. the red peak corresponds to the original unsplitted mode* λ_0.

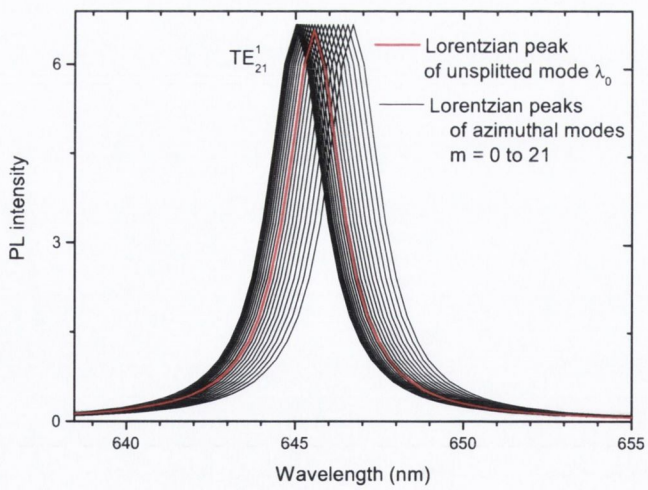

Figure 20. *Plot of all individual azimuthal modes which result in the modelled peak of Fig. 15. the red peak corresponds to the original unsplitted mode* λ_0.

following points for a more detailed characterisation are considered. Firstly, the linewidth and the intensity of each individual mode were assumed to be equal for all modes. Particularly the modes in the polar region which are in contact with the substrate and located in the distorted region will experience a decrease of intensity and Q-factor due to leaking losses into the substrate [30] and due to losses in the deformed region of the PE shell. On the basis of the simplified approach in the calculated peak-shape model, we did not expect a quantitative exact conformity with the experimental peak. However, the qualitative conformity supports our thesis very well. The line-shape analysis suggests a shell distortion and thereby an induced selective mode degeneracy lifting, causing a double-peak splitting of the overlapped modes. A PL wavelength scan with higher resolution would probably reveal more details in the mode shape structure. The identification of individual azimuthal resonances would allow us to gain a more detailed analysis in the dynamic distribution of the azimuthal modes in a deformed microcavity. The separation of the modes would allow the identification of the Q-factor reduction in the particular region of the sphere, where the modes are located. Modelling the exact number of azimuthal modes in the sphere which contribute to the peak broadening would also reveal the expansion of the shape distortion of the shell as we are able to identify the inclination angle of the individual modes by the azimuthal mode number (see Fig. 5) which would give us more information about the extent of deformation around the solid sphere core.

By means of the line-shape fit which is based on the variation of the ellipticity, we determined an approximate value for the ellipticity e. The derived value for the resonance in Fig. 14 is determined to be $e = -8.5 \cdot 10^{-3}$. For the line-shape fit in Fig. 15, the ellipticity was determined to be $e = -5.0 \cdot 10^{-3}$. This calculation suggests that the deformation of the PE shell in the measurement of Fig. 14 is slightly larger than in the second measurement. This is in agreement with the broader linewidth of the peaks in Fig. 14. The derivation of an absolute value for the deformed shell is rather difficult, as we cannot apply the formula for a perfect oblate spheroid deformation. The equation for the ellipicity e for a deformed spheroid is

$$e = \frac{r_p - r_e}{a} \quad . \tag{5.14}$$

The radius of the spheroid in the polar direction is r_p and in the equatorial direction r_e, the radius of the perfect sphere is a. The shell deformation in our experiment experiences no change in the equatorial radius, but in the polar radius in the region between the sphere centre and the substrate. So far, the ellipticity derived from the peak-shape fit provides a value to estimate a relative shape change in comparison to the original radius a. The ellipticity $e = - 8.5 \cdot 10^{-3}$ corresponds to a higher deformation than $e = - 5.0 \cdot 10^{-3}$. This is a reasonable result as the laser intensity in the first measurement is 3 times higher than in the second. In the following section, the observed blue-shift of the resonance spectrum at intensity tuning of the excitation laser is discussed. While the variation of the focus position does not influence the absolute wavelength position of the WGMs in the spectrum, we have to account for the resonance shift when tuning the laser intensity due to the temperature gradient of the sphere material.

5.8 Temperature-induced blue-shift of Whispering Gallery Modes

In our measurement series, we frequently observed a blue shift of the resonance spectrum with increased laser output power. The effect of long time exposure of our microsphere-emitter to the laser light was already studied in section 4.4. Changes in the resonance frequency in this time frame suggest a thermal effect of the microsphere resonator. Increased laser power results in heating of the sphere due to the small focal size on the particle. Temperature tuning is a common method for frequency tuning of diode lasers. The experiments carried out with the microsphere-emitter show the potential of controlled tunablity of the WGMs across the spectrum within a limited range, which depends on the maximum applicable temperature. In our measurement series, we studied the spectral tuning range of microsphere-emitter with different PE layer thickness. The laser intensity was varied and the relative mode shift was observed under cw laser excitation. The analysis shows initial results in regards to mode tuning with laser heating of the microcavity for a potential microsphere laser. The following table and the following graphs summarise the observed tuning effect on our samples. The table in Fig. 21 shows the maximum relative blue shift $\Delta\lambda$ of two individual modes selected from the blue end and the red end of the PL spectrum. The spectra were taken at varying laser intensities corresponding to a temperature change of the microcavity.

The relative mode shift $\Delta\lambda$ is determined by the wavelength position difference of a particular mode measured at two laser intensities. The blue-shift was observed with the *3* bi-layer, the *5* bi-layer and the *6* bi-layer samples on silicon substrate. An additional measurement was carried out with a *6* bi-layer sphere on a gold mirror substrate. The

Mode shift Δλ Blue End of Spectrum	Mode shift Δλ Red End of Spectrum
6 PE layer samples on Si-substrate	
Excitation power : 0.1 mW → 10 mW	
Δλ = 1.52 nm	Δλ = 1.64 nm
10 PE layer samples on Si-substrate	
Excitation power : 1 mW → 15 mW	
Δλ = 1.26 nm	Δλ = 1.53 nm
12 PE layer samples on Si-substrate	
Excitation power : 1.5 mW → 15 mW	
Δλ = 1.42 nm	Δλ = 1.55 nm
12 PE layer samples on goldmirror-substrate	
Excitation power : 2 mW → 10 mW	
Δλ = 7.64 nm	Δλ = 7.85 nm

Figure 21. *Table of blue-shifted modes measured with microspheres of different PE layer thickness.*

relative shift of $\Delta\lambda$ in the left column of the table is determined for a mode taken from the blue end of the spectrum while the right column shows the relative mode shift of an optical mode chosen from the red end of the spectrum. As the start and the target laser output power is not exactly the same for all measurements, an accurate systematic analysis was not possible. The tendency of the blue-shift in each of the measurements leads to the conclusion that the shifted distance is approximately equal for all three microsphere samples with different PE layer thickness when the experiment was carried out on the Si-substrate. That leads to the conclusion that the blue-shift is independent of the PE layer thickness. The measurement on the gold mirror reveals a considerably higher mode shift in comparison with the shift on the Si-substrate. The reflectivity of the gold mirror is several times higher than the Si-substrate. Due to that fact, a higher fraction of the light is reflected back into the sphere which causes a higher temperature increase of the sphere material. The three plots in Fig. 22 show the relative shift of the individual modes from the red end and the blue end of the spectrum versus the

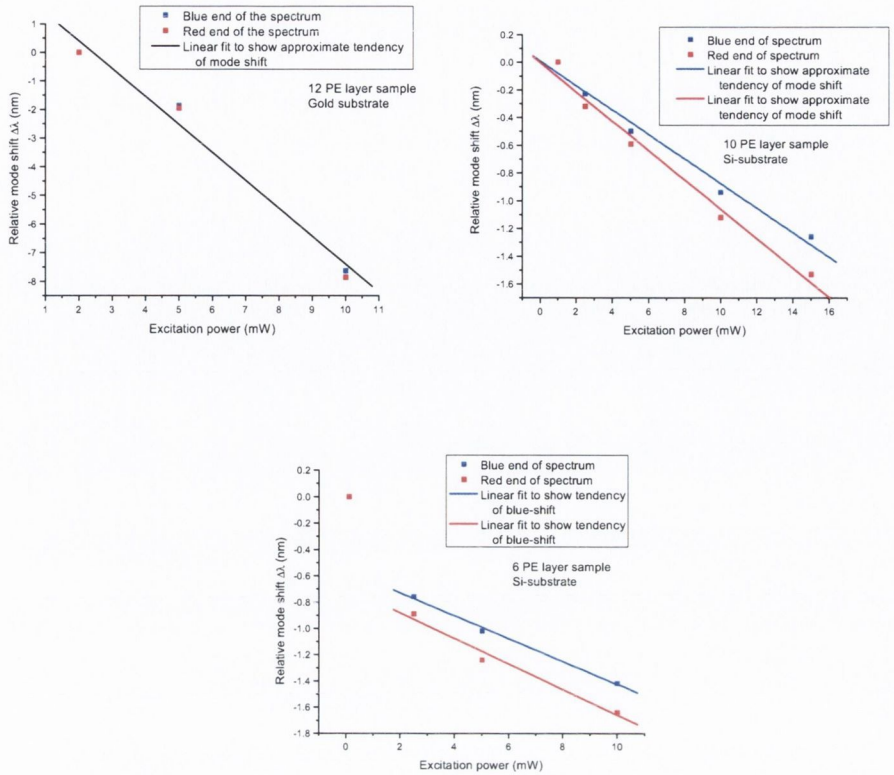

Figure 22. *Mode shift of resonances from the blue and the red end of the measured PL spectrum as a function of the excitation power of the laser.*

laser output power. The experimental data only provides limited number measurements for an excitation power dependent resonance shift. Nevertheless, the linear fit lines show a tendency for the blue shift of the resonances. The slope of the fit lines provides a value for the shift per mW when a linear shift is considered. The interesting result in this study is the highly increased tunablility range when using a gold mirror as a substrate. Further studies in regards to the blue shift could reveal potential implementation for photonic molecule coupling. To achieve strong coupling between a pair of spheres with different sizes, a tuning of the resonances of one sphere could by applied to get into the regime of efficient mode coupling with the second sphere. Even the tuning of the anti-bonding and bonding modes in the strong coupling regime is possible with

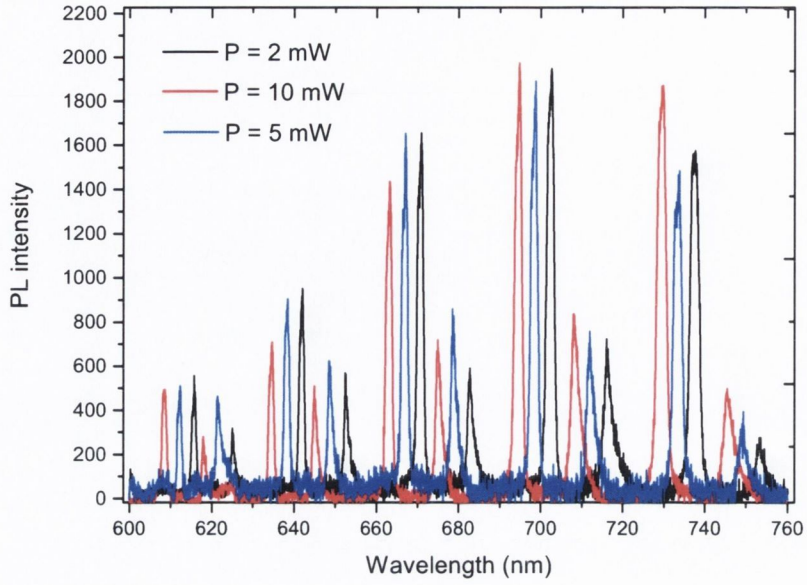

Figure 23. *Blue-shift of resonances in a 3 micron sphere placed on a gold mirror substrate.*

temperature-induced fine tuning of the optical resonances of one sphere. The PL spectra in Fig. 23 show an example of excitation-induced temperature tuning of a *3 μm* sphere on the gold mirror substrate. The first measurement was carried out at $P = 2\ mW$ excitation power of the Ar^{+}-ion laser. When the laser intensity was increased to *10 mW*, all WGMs experience a blue shift (red curve). In the last step, the intensity was reduced to *5 mW*, which results in a red-shift back towards the original resonance frequencies due to a temperature reduction. The resonance modes are shifted by more than *7 nm* when the intensity was increased to *10 mW* on the gold mirror substrate. The strong resonance shift has its origin in the negative thermo-optical coefficient of the polymer multilayer. The laser beam intensity induces a heating of the sphere and in particular the multilayer on the surface. As the resonances are very sensitive to changes of the refractive index, the blue-shift is assigned to the temperature-dependent refractive index change of the material. Due to the lack of exact values for the thermo-optical coefficient of polyelectrolyte multilayers in the literature, an exact determination of the temperature increase is not possible. A rough estimation can be carried out to verify, that the blue-shift is caused by the change of the

refractive index due to a variation in temperature. A temperature-induced shift of the absorption peak of a multilayer polymer coated side polished fibre is demonstrated in [32]. The experimentally observed blue-shift is about *20 nm* when the temperature was increased from $9.7\,^{\circ}C$ to *42 ℃*. The approximate thermo-optical coefficient for polymers is in the range of $10^{-4}\,K^{-1}$. As stated in [33], the value for rubbery polymers is typically larger than $-3 \cdot 10^{-4}\,K^{-1}$. The calculation to estimate the temperature rise is carried out with $dn/dT = -3 \cdot 10^{-4}\,K^{-1}$ as a minimum absolute value. The linear dependency of the temperature increase ΔT to the refractive index change Δn is given by

$$\Delta T = \Delta n \cdot \frac{dT}{dn} \quad . \tag{5.15}$$

The relative refractive index change Δn was determined from the blueshift with the Mie-scattering programme. The refractive index was fitted until the calculated resonance frequency matched with the shifted frequency. The relative refractive index change is $\Delta n = -0.021$. The corresponding value for the relative temperature increase *is* $\Delta T = 70\,℃$ when the laser intensity was increased from *2 mW* to *10 mW*. We estimate this as a maximum increase of temperature. A larger absolute value for the thermo-optical coefficient results in a lower temperature rise. This rough estimation for the temperature which induced the blue-shift of the resonance spectrum is considered as a reasonable verification that the shift is caused by the refractive index change of the polymer layer.

5.9 Optical switch based on radiation pressure

Based on the shape distortion of the microsphere by radiation pressure, the principle behind an optical switch based on microspheres coated with a soft PE shell is demonstrated in this section. The measurements show an optical switching process between two modes of a split WGM peak. The measurement also demonstrates fine tuning of the optical mode frequency by varying the laser intensity and therefore, the sphere temperature. The novel characteristic of this method is the ability to tune and switch the modes by changing the radiation pressure exerted on the microsphere. This was carried out with the excitation laser, no additional device such an external heat source or a mechanical device for applying mechanical strain is required. The experimental results are a proof of concept, as the PL emission is in the visible region rather than around *1.5 μm* where data transmission in an optical fibre would occur. The radiation pressure effect for these microsphere samples is already discussed in detail in the previous section. The measurements discussed here demonstrate an optical switch based on the new approach of a deformation of the soft PE shell by radiation pressure and the temperature tuning ability. The sample which was used in this experiment is the *3 μm* MF sphere coated with *10* layers (*5* bi-layers) of PE and one monolayer of CdTe nanocrystals. The PE shell was softened in a *7* molar NaCl solution for 5 days prior to the final coating of the nanocrystal layer. The *514 nm* line of the Ar^+-ion laser was used for excitation in the setup. The measurements were carried out with the micro-PL setup. The spheres were placed on a microscope glass slide and the output power was set to *25 mW*. The intensity variation was obtained by neutral density filters.

The laser is focused on the substrate in the centre of the sphere. The three graphs in Fig. 24 demonstrate the blue shift of the resonance mode with increasing temperature when the laser power was set to *0.25 mW* corresponding to *1%* intensity, *2.5 mW (10%)* and *6.25 mW (25%)*. The minor shift of the mode allows only fine tuning. As a result of the intensity change, the linewidth of the larger main peak does not change but peak structure slightly changes towards shorter wavelengths under the increasing power. A high degree

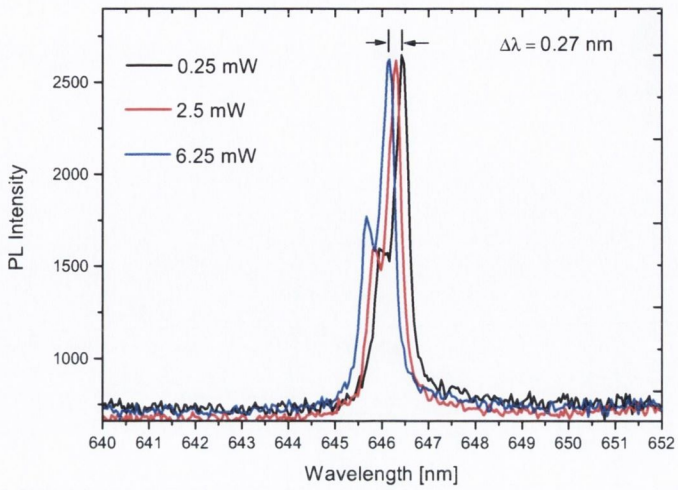

Figure 24. *Resonance mode tuning by the variation of the laser intensity.*

of elastic deformation of the PE shell is already achieved at low power (*0.25 mW*) due to the softened layer. Although the intensity is strongly increased, the shape broadening is fairly small, which suggests that the elastic limit and thus the deformation limit of the PE shell is reached already at low excitation intensity. The reason for the fact, that the left peak has a lower intensity than the right peaks is given by the change of the substrate from Si to glass. On glass, considerably more light is leaking from the modes into the substrate. Therefore, the peak corresponding to the undistorted mode in the equatorial region has now a higher intensity than the distorted azimuthal modes near the substrate. Increasing the output power from *0.25 mW* to *6.25 mW* induced a blue-shift of the resonance peak by $\Delta\lambda = 0.27$ *nm*. The following variation causes switching within the double-peak structure of the resonance mode induced by a change of the focus position. The three graphs in Fig. 25 show the split peak under varying radiation pressure, switched by the focus position. The measurement of the blue peak was taken when the beam was focused on the substrate ($z = +1.5$ *μm)* which corresponds to a radiation force in the beam direction. The intensity of the emission is concentrated to the longer wavelength end of the peak. Changing the focus to a position near the sphere centre ($z = -0.5$ *μm)* induces an equal intensity distribution to both peaks of the double-peak structure of the resonance mode. This position corresponds to a radiation force in opposite direction of the beam. When the focus is further lifted to the region of a maximum reversed radiation force ($z = -2.5$ *μm)*, the peak shape shows a

distribution as shown in the red curve in Fig. 25. The intensity is concentrated on the shorter wavelength side of the peak. The shape in the two opposite configurations can be regarded as two channels or two states of an optical switch. The red graph represents channel 1 and the blue

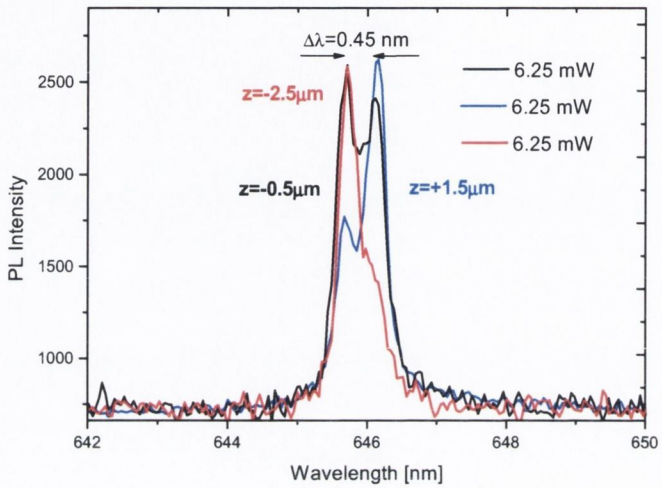

Figure 25. *Two-channel optical switch realised by a variation of the focus position and consequently, the radiation pressure.*

graph channel 2. Switching to both channels simultaneously is achieved under radiation pressure at $z = -0.5\ \mu m$, represented by the black graph. In dense wavelength division multiplexing (DWDM) the commercially used channel spacing is 50 GHz which corresponds to a free spectral range of $\Delta\lambda = 0.8\ nm$. The next generation in optical data communications provides a channel spacing of 100 GHz which is $\Delta\lambda = 0.4\ nm$. The two peaks in the measurement as supposed channels are separated by $\Delta\lambda = 0.45\ nm$, which corresponds to a channel spacing near the 100 GHz technology. This experiment demonstrates a potential application for microspheres with a soft elastic shell, deformed by radiation pressure. The experiment shows the ability for controlled azimuthal mode splitting by radiation pressure without applying mechanical strain.

5.10 Conclusions

The effect of controlled radiation pressure on an active spherical microcavity with a soft elastic shell was investigated by measuring the photoluminescence emission from the CdTe nanocrystals coupled into the resonance modes of the microsphere. The focus dependent radiation pressure was calculated for the x-axis dependency in vertical direction. The variation of radiation pressure exerted on the sphere by changing the focus position induced a shape distortion of the optical resonances. A model was developed to demonstrate the correlation between the deformation of the spherical shape, in particular the deformation of the soft elastic shell on the sphere surface, and the shape distortion of the optical resonances. It was concluded that the mode shape changes as a result of the lifting of the azimuthal mode degeneracy. This was verified by the model which fit very well to the experimental data. An example for a potential application as an optical switch was demonstrated. It was also shown, that the microsphere with the elastic PE shell is very sensitive to temperature changes, which result in a large spectral shift of the optical resonances. A rough estimation for the temperature change was carried out.

References

[1] A. Ashkin, "History of optical trapping and manipulation of small-neutral particle, atoms, and molecules," IEEE J. Quantum Electron. **6**, 841-856 (2000).

[2] J. E. Molloy, and M. J. Padgett, "Lights, action: optical tweezers," Contemp. Phys. **43**, 241-258 (2002).

[3] Robert C. Gauthier, R. Niall Tait, Howard Mende, and Chris Pawlowicz, "Optical selection, manipulation, trapping and activation of a microgear structure for applications in micro-optical- electromechanical systems," Appl. Opt. **40**, 930-937 (2001).

[4] M. Sulfridge, Taher Saif, N. Miller, and K. O'Hara, "Optical actuation of a bistable MEMS," J. Microelectromech. Syst. **11**, 574 (2002).

[5] C. Höhberger Metzger, and K. Karrai, "Cavity cooling of a microlever," Nature **432**, 1002 (2004).

[6] D. Dragoman, and M. Dragoman, "Optical actuation of micromechanical tunneling structures with applications in spectrum analysis and optical computing," Appl. Opt. **38**, 6773 (1999).

[7] I. Teraoka, and S. Arnold, "Enhancing the sensitivity of a whispering-gallery mode microsphere sensor by a high-refractive-index surface layer," J. Opt. Soc. Am. B **23**, 1434 (2006).

[8] I. Teraoka, and S. Arnold, "Theory of resonance shifts in TE and TM whispering gallery modes by nonradial perturbations for sensing applications," J. Opt. Soc. Am. B **23**, 1381 (2006).

[9] S. Arnold, M. Khoshsima, I. Teraoka, S. Holler, and F. Vollmer, "Shift of whispering-gallery modes in microspheres by protein adsorption," Opt. Lett. **28**, 272 (2003).

[10] I. Teraoka, S. Arnold, and F. Vollmer, "Perturbation approach to resonance shifts of whispering- gallery modes in a dielectric microsphere as a probe of a surrounding medium," J. Opt. Soc. Am. B **20**, 1937 (2003).

[11] H.-M. Tzeng, M. B. Long, R. K. Chang, and P. W. Barber, "Laser-induced shape distortions of flowing droplets deduced from morphology-dependent resonances in fluorescence spectra," Opt. Lett. **10**, 209 (1985).

[12] V. S. Ilchenko, P. S. Volikov, V. L. Velichansky, F. Treussart, V. Lefèvre-Seguin, J. -M. Raimond, and S. Haroche. "Strain-tunable high-Q optical microsphere resonator," Opt. Commun. **145**, 86 (1998).

[13] V. V. Lulevich, D. Andrienko, and O. I. Vinogradova, "Elasticity of polyelectrolyte multilayer microcapsules," J. Chem. Phys. **120**, 3822 (2004).

[14] O. V. Lebedeva, B. – S. Kim, K. Vasilev, and O. I. Vinogradova, "Salt softening of polyelectrolyte multilayer microcapsules," J. Colloid Interface Sci. **284**, 455 (2005).

[15] Y. P. Rakovich, J. F. Donegan, M. Gerlach, A. L. Bradley, T. M. Connolly, J. J. Boland, N. Gaponik, and A. L.Rogach, "Fine structure of coupled optical modes in photonic molecules," Phys. Rev. A **70**, 051801-1-051801-4 (2004).

[16] A. Ashkin, J. M. Dziedzic, J. E. Bjorkholm, and S. Chu, "Observation of a single-beam gradient force optical trap for dielectric particles," Opt. Lett. **11**, 288 (1986).

[17] Bohren, C.F. and Huffman, D.R., "Absorption and Scattering of Light by Small Particles", Wiley, New York, 1983.

[18] G. Gouesbet, G. Grehan, and B. Maheu "Scattering of a Gaussian beam by a Mie scatter center using a Bromwich formalism", J. Optics (Paris) **16**, 83 (1985).

[19] G. Gouesbet, G. Grehan, and B. Maheu , "Computations of the g_n coefficients in the generalized Lorenz-Mie theory using three different methods", Appl. Opt. **27**, 4874 (1988).

[20] G. Gouesbet, G. Grehan, and B. Maheu , "Scattering of laser beams by Mie scatter centers: numerical results using a localized approximation" , Appl. Opt. **25**, 3539 (1986).

[21] G. Gouesbet, G. Grehan, and B. Maheu, "Localized interpretation to compute all the coefficients g_{nm} in the generalized Lorenz-Mie theory", J. Opt. Soc. Am. A **7** , 998 (1990).

[22] K. F. Ren, G. Grehan, and G. Gouesbet, "Prediction of reverse radiation pressure by generalized Lorenz-Mie theory," Appl. Opt. **35**, 2702 (1996).

[23] R. K. Chang, and A. J. Campillo, "Optical Processes in Microcavities", World Scientific Pub Co Inc, (1996).

[24] K. K. Liu, D. R. Williams, and B. J. Briscoe, "The large deformation of a single micro-elastomeric sphere", J. Phys. D: Appl. Phys. **31**, 294 (1998).

[25] E. W. Deeg, "New algorithms for calculating Hertzian stresses, deformations, and contact zone parameters", AMP J. Technol. **2**, 14 (1992).

[26] L. Vu-Quoc, and X. Zhang, "An elastoplastic contact force-displacement model in the normal direction: displacement-driven version", Proc. R. Soc. Lond. A **455**, 4013 (1999).

[27] T.-C. Fu, and D. B. Bogy, "Analysis of stresses induced by dynamic load head-disk contacts", J. of Tribology **122**, 233 (2000).

[28] W. von Klitzing; R. Long, V. S. Ilchenko, J. Hare, V. Lefevre-Seguin, "Tunable whispering gallery modes for spectroscopy and CQED experiments", New journal of physics **3**, 14 (2001).

[29] H. M. Lai, P. T. Leung, K. Young, P. W. Barber, and S. C. Hill, "Time-independent perturbation for leaking electromagnetic modes in open systems with application to resonances in microdroplets" Phys. Rev. A **41**, 5187 (1990).

[30] H. Ishikawa, H. Tamaru, K. Miyano, "Microsphere resonators strongly coupled to a plane dielectric substrate: coupling via the optical near field", J. Opt. Soc. Am. A **17**, 802 (2002).

[31] W. Inami, Y. Kawata, "Photon force analysis for a spherical particle near a substrate illuminated by a tightly focused laser beam", J. Appl. Phys. **94**, 2183 (2003).

[32] S. W. James, R. P. Tatam, "Fibre optic sensors with nano-structured coatings", J. Opt. A: Pure Appl. Opt. **8**, S430 (2006).

[33] Z. Zhang, P. Zhao, P. Lin, and F. Sun, "Thermo-optic coefficient of polymers for optical waveguide applications", Polymer **47**, 4893 (2006).

Chapter 6

Resonance mode coupling in a bi-sphere system

6.1 Introduction

The experimental work studying the optical characteristics of the nanocrystal-microsphere emitter in this thesis was related to single microspheres so far. The evanescent component of the optical resonances which surround the microsphere allow coherent coupling of spherical microcavities when the spheres are in close proximity to each other. Extending the ideas of the linear combination of atomic orbitals method to the classical wave case, it was recently suggested that Mie resonances of single spherical microcavity play the same role as the atomic orbitals in the electronic case and the spatial distributions of whispering gallery modes can be described by analogy with the orbitals in a hydrogen atom [1]. The electro-magnetic fields confined in microsphere are given by [2]

$$\mathbf{E}_{TE} = j_n(nkr)Y_l^m(\theta,\phi), \tag{6.1}$$

for modes having no radial components of the electric field (transverse electric or TE modes) and

$$\mathbf{E}_{TM} = \nabla \times j_n(nkr)Y_l^m(\theta,\phi), \tag{6.2}$$

for the transverse magnetic (TM) modes (no radial component of the magnetic field).

Here $Y_l^m(\theta,\phi)$ are the vector spherical harmonics given in spherical polar, $j_n(n_r kr)$ represents the spherical Bessel function, where $k = 2\pi/\lambda$ is the wavenumber, n_r is the refractive index of the sphere and λ is the free space wavelength.

On the other hand, the wave functions Ψ_{slm} for the electron confined in the hydrogen atom are given by [3]

$$\Psi_{slm} = R_{sl}(r)\mathrm{Y}_{lm}(\theta,\phi), \tag{6.3}$$

where $R_{sl}(r)$ is known as the Laguerre polynomials. The eigenfunctions (6.1), (6.2) and (6.3) are very similar and their spatial distributions are characterized by the three integer *s*, *l* and *m* (for hydrogen atom) and *l*, *n* and *m* (for microspheres), which correspond to total angular, radial and the azimuthal quantum numbers, respectively. Based on all above similarities this approach has enabled small dielectric spheres to be considered as "photonic atoms" [1, 4]. However, unlike energy states of electrons in the atom, photonic states in spherical microcavities are not localized due to finite storage time (τ) of photons in the resonant mode. This "photon lifetime" is controlled by *Q* factor of WGM and therefore can be limited by diffractive losses, absorption, gain, shape deformation or refractive index inhomogeneity [3]. As a result, the resonant internal field of a spherical cavity is not completely confined to the interior of the microparticle. Depending on the size of the microsphere, the evanescent field can extend into the surroundings up to a couple of micrometers. It was recently recognized that the partial delocalization of Mie resonance states is of great importance because it suggests a possibility for coherent coupling between WGMs of two adjacent spherical particles with closely matched sizes. Such a system of coherently coupled photonic atoms may be called a "photonic molecule" (PM) [5] and can be employed in order to manipulate photons in the micrometer length scale. In analogy to the formation of molecular electronic orbits, the tight binding approximation provides two combinations for the electromagnetic field in a system of interacting microspheres: bonding (BN) and anti-bonding (ABN) state [5-8]. Experimentally, the coupling of the photon modes of individual microspheres in the PM can cause a narrow resonance of a photonic atom to split into two modes of lower *Q*-factor [6]. This phenomenon has been demonstrated in a system of two square, photonic dots coupled by a narrow channel [5] in a dye-stained bi-sphere system [7, 9, 10], in photonic dots doped by CdSe nanocrystals [11] and in chains of polymer-blend microparticles [12]. However recent theoretical considerations [8] and experimental studies [13, 14] reveal a complex internal distribution of density of photonic states of PM originating from lifting of degeneracy of PM modes with respect to the azimuthal index.

6.2 Coherent coupling

Theoretical considerations [6,8] show that the intersphere coupling is expected to be maximum for the pair of modes whose orbitals include the contact point between the microspheres and lie in the same plane [7]. In order to achieve intermode coupling, the bi-sphere system was excited at the contact point between the two spheres. A polystyrene substrate containing a three-dimensionally ordered array of pores of ~ 1 μm in size prepared through a thermocapillary convection [16] was utilized to maintain the high Q-factor and to reduce the leakage of light into the substrate to a minimum. For that purpose, the spheres were placed on the pores resulting in a small contact area restricted to the rim of the pore (see Fig. 1). The ordered structures are formed by evaporating solutions of

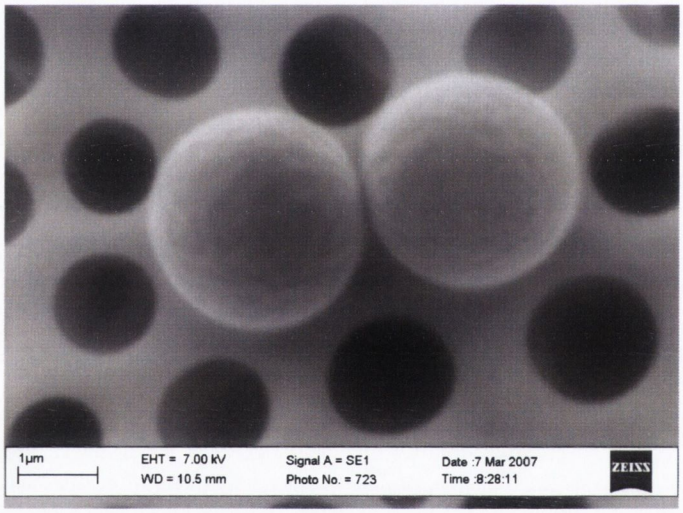

Figure 1. *SEM picture of a bi-sphere placed on the polystyrene pore substrate. The spheres are located on the pores to reduce the contact with substrate and consequently the leakage of light which quenches the Q-factor.*

polystyrene in a volatile solvent, in the presence of moisture with forced airflow across the solution surface. A hexagonally packed array of holes (microwells) then forms on the surface of the polymer. A high *Q*-factor is required to achieve highly efficient coherent coupling. In addition to the pore substrate we utilized Rhodamine B dye coated microspheres instead of spheres coated with CdTe nanocrystals. The dye layer on the sphere surface does not reduce the Q-factor as much as a microsphere coated with

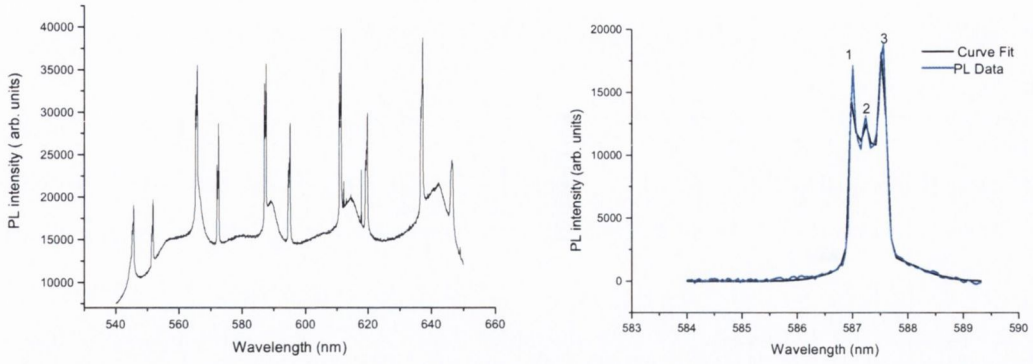

Fig. 2. left: *PL measurement of a WGM spectrum of a single sphere on a polystyrene substrate.* ***right:*** *Lorentzian curve fit of a single peak from the spectrum.*

multilayers of PE and a monolayer of CdTe. Initial measurements were carried out on a single sphere with a diameter of 3 μm to determine the *Q*-factor of the resonances when excited in the micro-PL setup. The microsphere was placed on a polystyrene substrate and excited with the *457 nm* line of the Ar^+-laser at *2.5 mW*. The WGM spectrum revealed narrow resonances, each of them were split into 3 peaks. As these samples were not coated with an elastic PE shell, the splitting is probably caused by azimuthal splitting due to mode coupling into the substrate. The polystyrene surface of the substrate is rather soft so that the sphere can cause an indentation where it is placed on the substrate. As discussed in [17], the azimuthal mode degeneracy is lifted when the sphere is in contact with a dielectric substrate by the coupled azimuthal modes. The linewidth and the Q-factor of the splitted peaks were determined by a Lorentzian fit as shown in Fig. 2. The original measurement is shown in the graph on the left hand side, while the graph on the right hand side shows a particular resonance peak, split into 3 peaks, and the Lorentzian fit. The

	Peak 1	Peak 2	Peak 3
Peak Position (nm)	587.545	587.237	587.001
Linewidth (nm)	0.136	0.332	0.087
Q-factor	4320	1768	6747

Fig. 3. *Calculated peak position, linewidth and Q-factor from the Lorentzian fit.*

linewidth and the Q-factor determined from the Lorentzian fit are shown in the table in Fig. 3. The highest Q is given by $Q = 6747$ which is determined from the third peak. The maximum theoretical Q-factor for a perfect sphere is calculated with the Mie-scattering programme. The linewidth is calculated from the imaginary parts of the Mie-scattering coefficients a_n and b_n. The imaginary part arises from the leakage of the modes into the surrounding. The theoretical Q-factor is only limited by the radiative losses due to the curvature of the microsphere. The maximum theoretical Q-factor was calculated to $Q = 14500$, which corresponds to a linewidth of $\Delta\lambda = 0.044\ nm$. A value of $Q = 6747$ is exceptionally high for a measured Q-factor of a $3\ \mu m$ sphere coupled with a free space laser beam. This is clearly a result of the pore substrate to reduce the contact area of the sphere with the substrate and the dye coating as a contribution to maintain the high-Q factor. Figure 4 shows the TE and TM resonances in the PL spectra of a bi-sphere located on a pore substrate (see Fig. 1). Figure 4 a) shows the spectrum of the weakly coupled

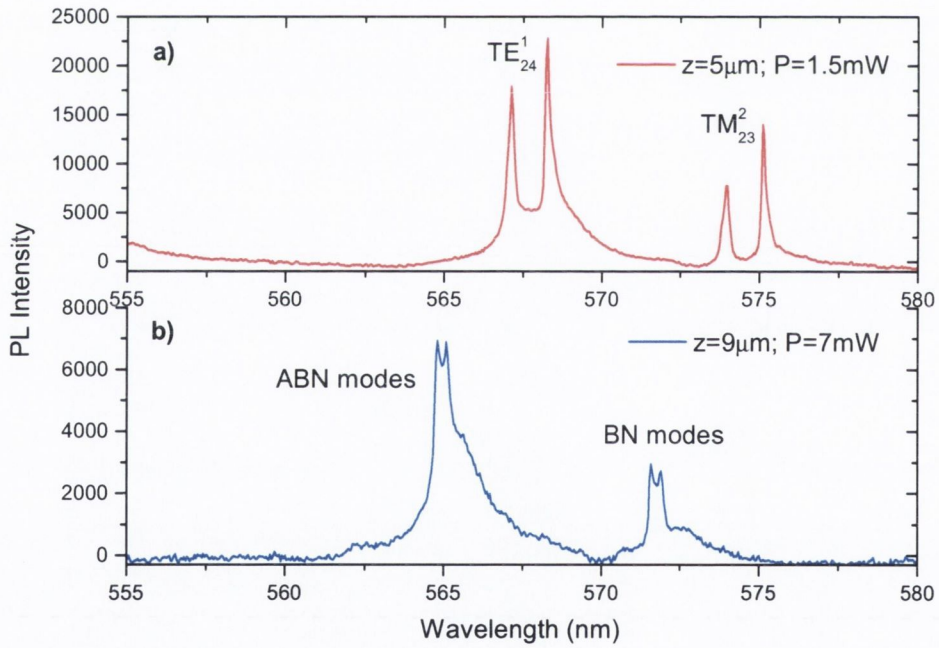

Figure 4. *a) Separated TE and TM peaks of both spheres due to size difference under weak coupling conditions. b) ANB and BN modes under strong coherent coupling.*
The z-value state the relative focus position above the substrate.

sphere pair. The focus is positioned *5 μm* above the substrate at the contact point between the spheres. The laser output power of the Ar^+-ion laser at *457 nm* is *1.5 mW*. The TE and TM modes of each sphere are well separated although the size difference of the two spheres is of only *6 nm*.

Figure 4 b) shows the modes under strong coherent coupling condition. Therefore, the intensity was increased to *7 mW* and the focus was moved up to *9 μm* above the substrate. In this experiment, strong coupling was achieved by increasing the focus distance from the photonic molecule. When the focus is located very close to the spheres, only a small fraction of the light is coupled into the WGMs. Strong coupling does not occur under these conditions. Due to the divergence of the tightly focused beam, the illumination conditions change when the focus position is lifted. The whole bi-sphere structure is excited, including all azimuthal modes, which results in strong coherent coupling. The originally uncoupled modes vanish completely and split into anti-bonding (ABN) and bonding (BN) modes [5]. The ABN and BN modes reveal a double peak structure caused by the separated TE peaks of each sphere due to the size difference. The fact that the uncoupled modes disappear completely indicates the extremely high coupling efficiency. The measurement is in very good qualitative agreement with the calculated spectrum presented by another group in [5] (see Figure 3 in this publication). The authors calculated the spectrum of a coupled bi-sphere for slightly smaller spheres of *2.4 μm* diameter based on the semianalytical MMP technique with systematic variation of dipole position, frequency, and orientation. Their results show that the original peak is split into BN and ABN modes shifted to the left and right in the spectrum relative to the original position. The difference with our measurement is that the calculation is based on spheres of identical sizes so that the modes overlap each other and the BN and ABN do not show the double peak. The strong coupled modes in our measurements in Fig. 4 b) reveal exceptionally well pronounced BN and ABN modes. In terms of cooperative scattering theory [6], the observed ABN and BN modes originate from the removal of the WGM degeneracy with respect to the *m* index. The line shape of the satellite lines reflects the energy distribution among the coupled modes, because modes with different combinations of *m* can contribute to the PL spectra. The observation of broader ABN and BN peaks reflects the decrease of the quality factor of the PM when compared with that of a single sphere presumably due to the interaction with more dissipative modes of lower *n* [7].

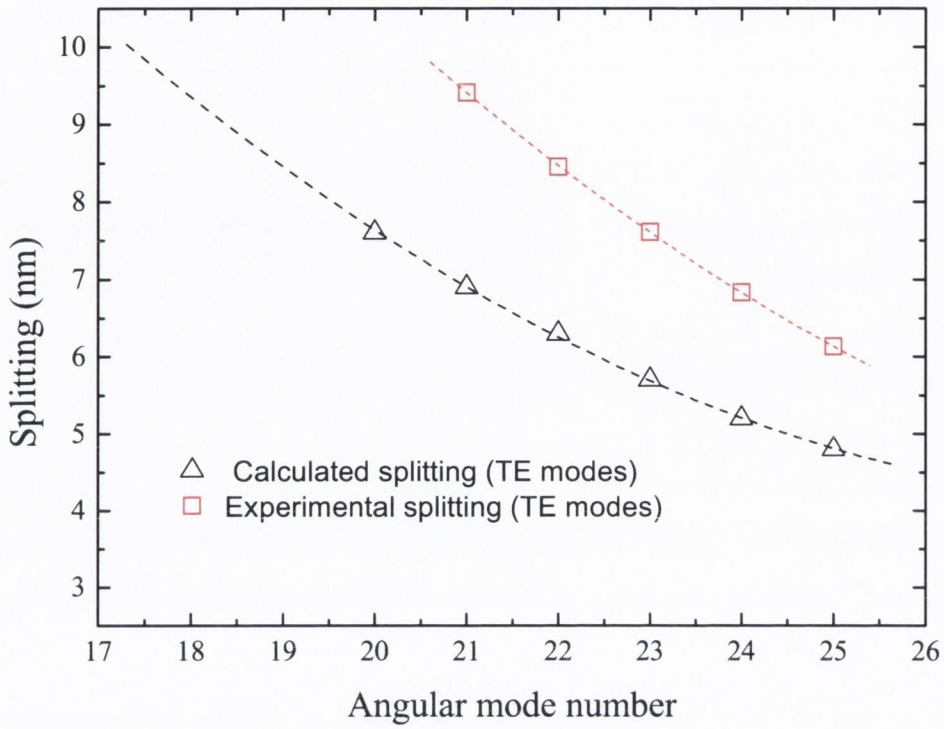

Figure 5. *Theoretical and experimental spacing between BN and ABN modes as a function of the angular mode number.*

The high PL efficiency of the dye and the coupling of electronic transitions of the dye to the resonances of the PM allow us to detect the BN and ABN branches in a wide spectral region from *540 to 660 nm*. This allows the possibility of estimating the magnitude of spectral spacing between bonding and anti-bonding branches as a function of angular mode number for comparison with theoretical calculations (Fig. 5). In order to calculate the BN/ABN splitting we adopted the maximum term approximation (MTA) of the single-mode tight-binding (SMTB) method [8]. For simplicity in our simulations we have considered only the case of identical spheres with WGM having radial quantum number $n = 1$, taking into account only the interaction between WGM of the same l. For a given WGM polarization, the value of the splitting between the BN and ABN modes of the PM can be obtained from

$$\Delta x_m = 2\Gamma_l \left| A_{l,m}(x_l) \right| \tag{6.4}$$

where $x_l = 2\pi R/\lambda_l$ is the size parameter of a resonance with mode number l, λ_l is the corresponding resonant wavelength, Γ_l is the width of mode l in a single sphere, which can be calculated within Mie-theory. For a given radius of single spheres a, the coefficient $A_{l,m}(x_l)$ can be calculated as

$$A_{l,m}(x_l) = -2\ell(-1)^{l+m} h_{2l}^{(1)}(k_0 Z) \times \sqrt{\frac{2l}{\pi(l+m)(l-m)}} \times \frac{l^{2l}}{(l+m)^{l+m}(l-m)^{l-m}}, \tag{6.5}$$

where $k_0 = x_n/a$ is the wavenumber, Z is the characteristic length [8], and the spherical Hankel function of the first can be estimated from

$$h_{2n}^{(1)}(k_0 Z) \cong -i \frac{\exp[(2n+1/2)(\alpha - \tanh\alpha)]}{(n+1/2)\sqrt{\sec h\alpha \tanh\alpha}}; \tag{6.6}$$

Here, α is defined by $k_0 Z = (2\ell+1/2)/\cosh\alpha$. The positions of the m-resonances were estimated as $x_m = x \pm \Delta x_m/2$.

Applying these equations we can see that the modelled data, presented in Fig. 5 displays behaviour which is in good agreement with the experimental data. From the micro-PL spectra of the PM we have found a decrease in splitting between BN and ABN branches value with increasing ℓ, with TE modes splitting being always higher than that of TM modes. Remarkably, the theory predicts the same behaviour. Although the maximum term approximation underestimates the splitting (Fig. 5), it is clear that this approach provides a good qualitative guide for the analysis of a variety of phenomena observed in PM. It is worth noting that observed disagreement between calculated and experimental values for the PM mode splitting may also have its origin in the fact that the magnitudes of splitting were estimated as a spectral distance between maxima of ABN and BN peaks. However detailed consideration of coherent mode coupling in PMs using SMTB approach shows that in fact the BN and ABN branches consist of a number of very narrow peaks, which are due to the presence of $m \neq \pm 1$ components [8]. The total number of these sharp peaks, originating from a certain mode ℓ, is governed by the actual degeneracy of the Mie resonances which in the approach of the normal mode concept is $\ell + 1$. (Due to the dependence of the mode coupling on the orbital plane orientation, the interaction is limited

between modes of only the same m, no degeneracy is removed between m and $-m$ and the new degeneracy of PM modes is now $\ell + 1$ with m running from 0 to ℓ) [8]. In our calculations within the SMTB model we estimated the splitting as a spectral distance between outer peaks assigned to modes with $m = \pm 1$, which do not correspond to the maximum of envelope of PM modes and therefore this may cause discrepancy between estimated and observed values of the mode splitting, particularly because the spheres have a size difference of $6\ nm$ and a spectral separation of $\Delta\lambda = 1.16\ nm$.

6.3 Weak coupling and optical switching

In contrast to strong coupling where the coupled modes are shifted and the line-shape is considerably broadened due to coupling losses, weak coupling between two spheres are characterised by sharp peaks with no significant broadening. There are no bonding and anti-bonding modes observed in the spectrum of the PL emission. The microsphere samples in this experiments were our CdTe nanocrystal coated microspheres. Excitation of resonances in the coupled spheres at different positions affects the coupling efficiency between the resonators [21]. By changing the excitation position, a mode switching was demonstrated in the bi-sphere system. Excitation of either both spheres or only one sphere at the time provides a method to add or drop channels and switch channels on or off. The resonance modes could represent the optical channels in a fibre network. The channels are separated by the free spectral range of the optical modes which strongly depends on the size of the microsphere. The experimental results demonstrate a simple optical switch based on the coupling efficiency controlled by the excitation position. Focusing the light on one of the bi-spheres excites the resonance modes in this sphere, while either a fraction of the light or almost no light is coupled into the second sphere. The PL emission from the nanocrystal layer on the sphere surface is coupled into the sphere and all resonances within the spectral emission range of the nanocrystals are excited. Exciting both spheres at the same time doubles the number of modes in the spectrum when the modes of each sphere are separated due to the size difference of the spheres. Optical switching was discussed and experimentally realised by different groups in recent years. A thermo-optical switch was demonstrated in [18], implemented with a polymer coated silica microsphere. Polarisation

switching in a microsphere by an applied external magnetic field is proposed in [19]. An all-optical switching device is discussed and demonstrated in [20] based on a microsphere coated or made out of non-linear optical material coupled to a planar Si-waveguide. Switching is achieved by the non-linear response of the material when excited at different intensities.

MF spheres with a diameter of *3 μm* and coated with one monolayer of CdTe nanocrystals were used for this experiment. A pair of sphere was placed on a Si-substrate and excited at three different positions (see Fig. 6). It strongly depends on the excitation position, in which modes the light is coupled efficiently. The spheres on the substrate are in contact with each other. Changing the separation distance between the spheres would induce a variation in coupling efficiency. Separation dependent coupling was studied for example in [15].

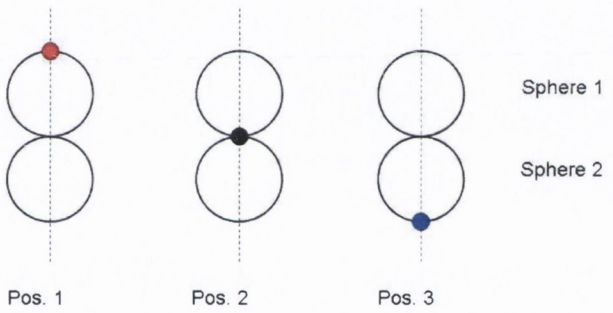

Figure 6. *Excitation spots for experimental channel switching in a bi-sphere system: top edge of sphere 1 (red spot), in between sphere 1 and sphere 2 (black spot) and bottom edge of sphere 2 (blue spot).*

The illustration in Fig. 6 shows the three excitation positions on the bi-sphere from a top view. The sphere system is either excited at the contact point between both spheres or at

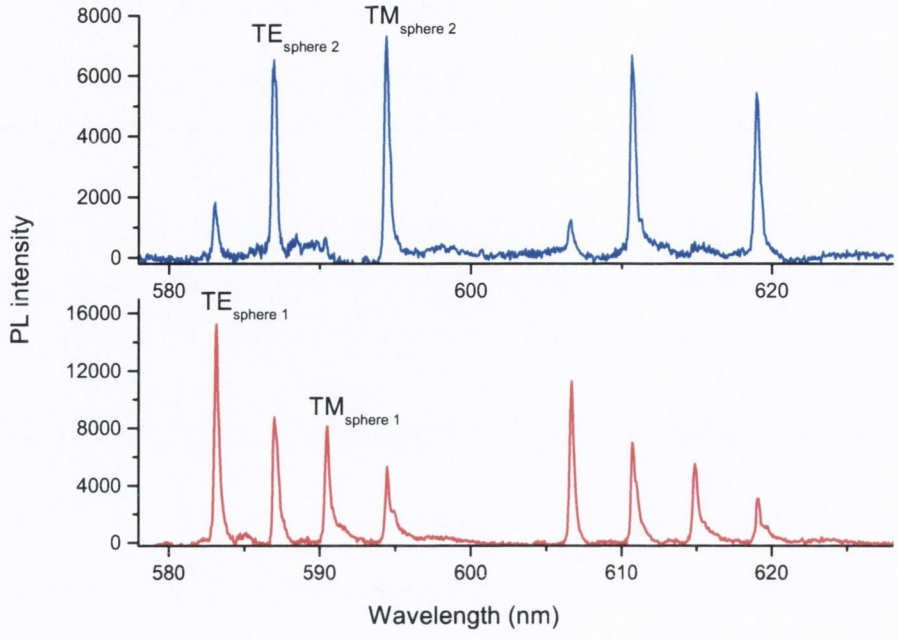

Figure 7. *PL spectra of two measurements of a bi-sphere system. The excitation position is indicated in Fig. 6. Position 3 in the upper graph (blue graph) and position 1 in the bottom graph (red graph).*

the edge of each sphere along the axis through the coupled system. The spheres are excited in the vertical direction to the substrate in the micro-PL setup. The first switching experiment shows the coupling of a bi-sphere system where the size difference of the spheres which determines the resonance positions in the spectrum result in an almost equal spacing between the TE and TM modes of both spheres. Excitation was carried out according to position 1 and position 3 in Fig. 6. The PL spectra of both measurements are shown in Fig. 7. When excited at the bottom edge of sphere 2 (blue graph), there is almost no light coupled to sphere 1, only very weak coupling into the TE mode of the first sphere is observable as a small peak. It is in contrast to the excitation of the top edge of sphere 1. Coupling from the excited sphere 1 into the sphere 2 is highly efficient. About 50% of the light is coupled into the second sphere as the intensity of the resonance peaks indicate. It is not clear in this measurement why the coupling efficiency is not equal in both

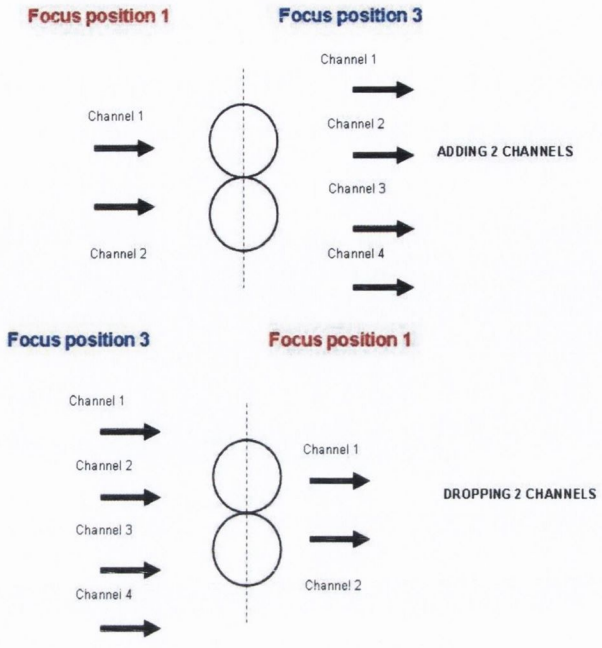

Figure 8. *Principle application of the optical switch. The spectra are shown in Fig. 7. According to the focus position, the bi-sphere systems works as a add/drop filter.*

measurements. It is expected that the coupling efficiency is equal in both directions which is either coupling from sphere 1 into sphere 2 or coupling from sphere 2 into sphere 1. A possible explanation is that the tightly focused beam acts as an optical trap and unintentionally separated the spheres when focused in position 3, whereas the separation did not happen when focused at position 1 which could be caused by inhomogeneous surface defects on the substrate.

To apply the optical switching effect to optical communications, Fig. 8 illustrates the principle of such an application in an optical network. The maximum number of channels is 4, as the TE and TM mode of each sphere which are closest together are chosen as a group. When the laser is focused at position 1, the optical signal is coupled into 2 channels which correspond to the excited TE and TM mode of sphere 2. Changing the laser to position 3, results in the excitation of 4 modes within the group. The signal is coupled into the TE and TM mode of each sphere. The laser excites the modes in sphere 1 directly. The light is then coupled into the second sphere. Consequently, two channels are added to the group. As there is no strong interaction between the modes of both spheres the mode position and the linewidth does not change and no mode splitting occurs under the

condition of weak coupling. The following two measurements demonstrate coupling of a bi-sphere system when the coupling efficiency from one sphere into the other one is very weak (Fig. 9 and 10). Therefore, only optical resonances are excited in the sphere where the laser is focused on. Excitation at the contact point between the spheres couples the light into both spheres. Excitation was carried out at all three coupling positions according to Fig. 6. We can consider two modes which are closest to each other, either TE or TM, as a group. Thus, switching occurs between two channels. The upper graph demonstrates coupling into both channels, the graph in the middle shows the condition when on channel is switched off and the bottom graph shows the switching of the signal to the other channel (Fig. 9 and Fig. 10). The two measurements clearly show the possibility of tuning the channel spacing and the spacing between the groups of resonances by the size of the microspheres. The spacings between the groups of resonances is specified by the size of the spheres. The small size-variation between both spheres specifies the spacing between the two channels in a group which consists of a TE or TM mode of each sphere. The size difference of the bi-sphere system in Fig. 10 is higher than in the system in Fig. 9. The difference in the diameter for the spheres in Fig. 9 is *10 nm*, while the difference in the diameter for the spheres in Fig. 10 is *24 nm*. Almost identical sphere diameters would allow a very narrow wavelength separation, necessary in a DWDM optical network in 50 GHz or 100 GHz technology. But at the same time, the probability of strong coupling between the resonances of both spheres would strongly increase. By changing the excitation position, weak coupling can still be achieved. However this would require excitation of both spheres separately as demonstrated in [21]. The principle technique for applying the bi-sphere system as a switch in optical communications is shown in Fig. 11. The two resonances which are the closest to each other are taken as the two optical channels (channel 1 and channel 2). The optical switch of the bi-sphere system can couple the signal into either both channels or only one of the channels, depending on the focus position. When the beam is focused at the contact point between the two spheres, the light is coupled into the resonance modes of both spheres, corresponding to both channels. By switching between excitation position 1 and 3, the signal can be switched between the two channels. These two measurements show that coupling between the two spheres is very weak so that only the modes in the excited spheres are observed in the spectrum. The evanescent field outside the sphere suggests that a reasonable coupling is expected. As mentioned above, the possible reason for the weak coupling is the radiation

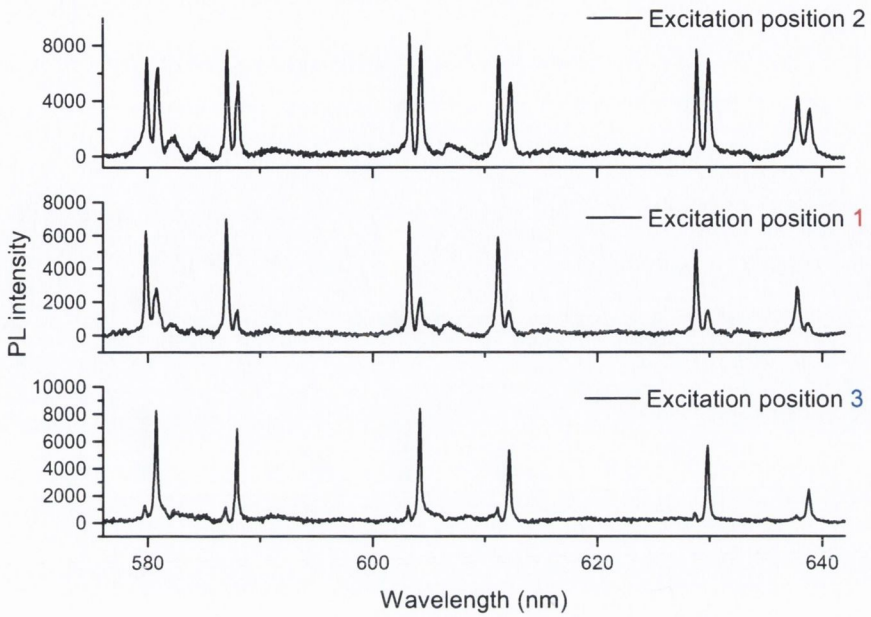

Figure 9. *PL spectra of a bi-sphere system, excited at 3 different positions according to Fig. 6. The diameter difference between the two spheres is 10 nm.*

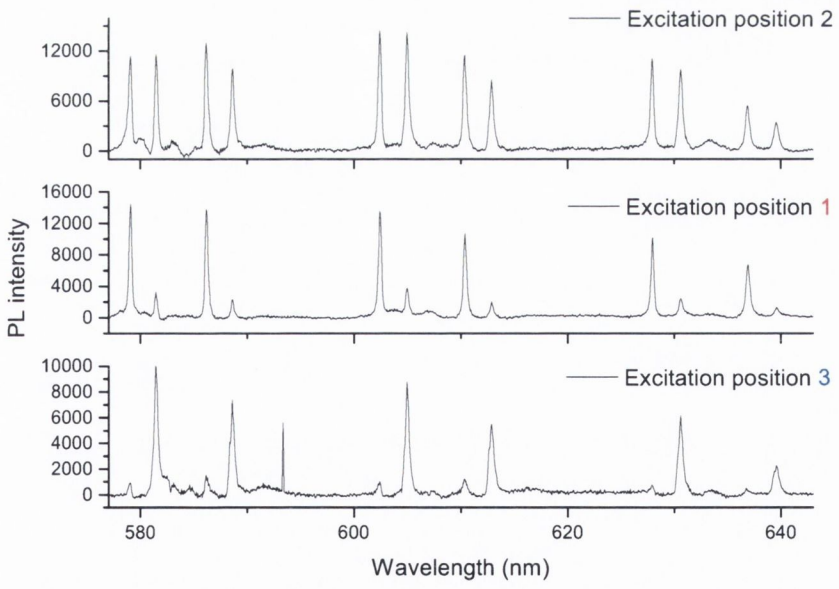

Figure 10. *PL spectra of a bi-sphere system, excited at 3 different positions according to Fig. 6. The diameter difference between the two spheres is 24 nm.*

force of the tightly focused laser beam which decreases the coupling efficiency by slightly separating the spheres as the particle is always pulled into the beam centre. The PL emission from the nanocrystal layer on the sphere surface excites the modes over a broad spectral range. This provides a large number of optical channels, depending on the size of the spheres in the coupled system. The apparent practical limitations of this kind of switch are the coupling of light into and out of the sphere to an optical fibre. The experimental setup collects the scattered light from the bi-sphere system in a 90 degree angle at free space. An optical switch application would require an efficient coupling device, preferably an evanescent wave coupler. Another practical issue is that the channel switching requires physical movement of the laser spot. This is carried out by a mechanical system. This switching process would definitely be the limiting factor in switching speed for the application. The optical switching experiment discussed in chapter 5.9 does not require changing the focus in lateral direction, However it requires a refocusing along the z-axis. When the free beam coupling in the demonstrated experiments are replaced by tapered-fibre couplers, channel switching would be possible without a change of the focus position, but it would be necessary to change the coupling of the laser signal between the three tapered fibres, similar to a microsphere-based add-drop device discussed in [22]. In

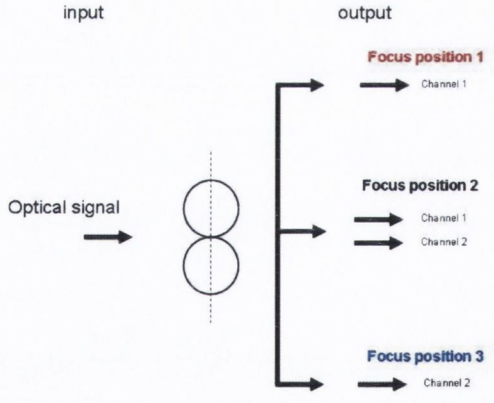

Figure 11. *Schematic configuration of an optical switch based on a weakly coupled bi-sphere (Fig. 9 and 10). Depending on the focus position according to Fig. 6, the signal is coupled into either both optical channels or one single channel.*

conclusion, weak coupling of spheres provides the ability to switch between high-Q resonances which make them potential candidates for optical switches and add-drop filters in optical communications. To achieve high switching speeds, appropriate switching of the coupling position is required.

6.4 Conclusions

Intersphere coupling of the optical modes in a bi-sphere system was demonstrated with two *3 μm* microspheres in contact with each other. The spheres were excited in the micro-PL setup in different excitation configurations. Thereby, the coupling efficiency was varied. Coherent coupling in the bi-sphere shows very well pronounced splitting of the coupled optical resonances into bonding and anti-bonding modes. The difference in size of the spheres was only *6 nm*. To reduce the leakage of the modes in contact with the substrate, a polystyrene pore array was utilized which was specifically adapted to the sphere size. The spheres were placed on the rim of the pores, reducing the contact area with the sphere. Weak coupling in the bi-sphere system demonstrated optical switching by varying the excitation position of the laser focus. The weak coupling showed intersphere evanescent coupling where light from one sphere was transferred into the other one without coherent coupling of the optical resonances. Potential separation of the spheres by the optical tweezing effect was suggested due to changing coupling performance when the bi-sphere was excited at the very left or right end of the system. Potential optical switching and the restrictions of this approach were discussed.

References

[1] E. Lidorikis, M.M. Sigalas, E.N. Economou, C.M. Soukoulis, "Tight-binding parametrization for photonic band gap materials", Phys. Rev. Lett., **81**, 1405 (1998).

[2] R.K. Chang, A.J. Campillo, *Optical Processes in Microcavities*, World Scientific, Singapore, 1996.

[3] P. Eisberg, R. Resnick, *Quantum Physics of Atoms, Molecules, Solids, Nuclei and Particles*, Wiley, New York, 1985.

[4] S. Arnold, J. Comunale, W.B. Whitten, J.M. Ramsey, K.A. Fuller, "Room-temperature microparticle-based persistent hole-burning spectroscopy", J. Opt. Soc. Am. B, 9, 819 (1992).

[5] M. Bayer, T. Gutbrod, J.P. Reithmaier, A. Forchel, T.L. Reinecke, P.A. Knipp, A.A. Dremin, V.D. Kulakovskii, "Optical modes in photonic molecules", Phys. Rev. Lett., **81**, 2582 (1998).

[6] K.A. Fuller, "Optical Resonances and Two-Sphere Systems", Appl. Opt., **30**, 4716 (1991).

[7] T. Mukaiyama, K. Takeda, H. Miyazaki, Y. Jimba, M. Kuwata-Gonokami, "Tight-Binding Photonic Molecule Modes of Resonant Bispheres", Phys. Rev. Lett., **82**, 4623 (1999).

[8] H. Miyazaki, Y. Jimba, "Ab initio tight-binding description of morphology-dependent resonance in a bisphere", Phys. Rev. B, **62**, 7976 (2000).

[9] S. Arnold, A. Ghaemi, P. Hendrie, K.A. Fuller, "Morphological resonances detected from a cluster of two microspheres", Opt. Lett., **19**, 156 (1994).

[10] Y. Hara, T. Mukaiyama, K. Takeda, M. Kuwata-Gonokami, "Photonic molecule lasing", Opt. Lett., **28**, 2437-2439, 2003.

[11] B.M. Möller, U. Woggon, M.V. Artemyev, R. Wannemacher, "Photonic molecules doped with semiconductor nanocrystals", Phys. Rev. B, **70**, 115323-1 (2004).

[12] M.D. Barnes, S.M. Mahurin, A. Mehta, B.G. Sumpter, D.W. Noid, "Three-dimensional photonic "molecules" from sequentially attached polymer-blend microparticles", Phys. Rev. Lett., **88**, 015508/1 (2002).

[13] Y.P. Rakovich, M. Gerlach, A.L. Bradley, J.F. Donegan, T.M. Connolly, J.J. Boland, M.A. Przyjalgowski, A. Ryder, N. Gaponik, A.L. Rogach, "Confined optical modes in small photonic molecules with semiconductor nanocrystals", J. Appl. Phys., **96**, 6761 (2004).

[14] Y.P. Rakovich, J.F. Donegan, M. Gerlach, A.L. Bradley, T.M. Connolly, J.J. Boland, N. Gaponik, A.L. Rogach, "Fine structure of coupled optical modes in photonic molecules", Phys. Rev. A, **70**, 051801(R)-1 (2004).

[15] S. P. Ashili, and V. N. Astratov, "The effect of inter-cavity separation on optical coupling in dielectric bispheres", Opt. Exp. **14**, 9460 (2006).

[16] M. Srinivasarao, D. Collings, A. Philips, S. Patel, "Three-dimensionally ordered array of air bubbles in a polymer film", Science, **292**, 79 (2001).

[17] H. Ishikawa, H. Tamaru, and K. Miyano, "Microsphere resonators strongly coupled to a plane dielectric substrate: coupling via the optical rear field", J. Opt. Soc. Am. A **17**, 802 (2000).

[18] H. C. Tapalin, J.-P. Laine, and P. A. Lane, "Thermooptical switches using coated microsphere resonators", IEEE Photon. Technol. Lett. **14**, 1118 (2002).

[19] A. Yu. Smirnov, S. N. Rashkeev, and A. M. Zagoskin, "Polarization switching in optical microsphere resonators", Appl. Phys. Lett. **80**, 3503 (2002).

[20] F. C. Blom, D. R. van Dijk, H. J. W. M. Hoekstra, A. Driessen, and Th. J. A. Popma, "Experimental study of integrated-optics microcavity resonators: Towards an all-optical switching device", Appl. Phys. Lett. **71**, 747 (1997).

[21] B. M. Moeller, U. Woggon, M. V. Artemyev, R. Wannemacher, "Photonic molecules doped with semiconductor nanocrystals", Phys. Rev. B **70**, 115323 (2004).

[22] M. Cai, G. Hunziger, and Kerry Vahala, "Fiber-optics add-drop device based on a silica microsphere-whispering gallery mode system", IEEE Photon. Technol. Lett. **11**, 686 (1999).

Chapter 7

Conclusions and outlook

7.1 Conclusions

Active spherical microcavities coated with semiconductor nanocrystals show great potential in photonics as building blocks for new applications in linear and non-linear optics and in other branches of science and technology. Small microspheres made of highly transparent material with a high refractive index possess extremely high Q-factors due to the long lifetime of the photons in the microcavity which are trapped by total internal reflection. Active microspheres are studied for sensor applications, low-threshold microsphere laser, optical switches and waveguides, and fundamental physics experiments, such as CQED and photonic molecule studies. The composite nanocrystal-microcavity system investigated in this thesis consists of a dielectric microsphere (polystyrene or melamine formaldehyde) coated with a soft elastic PE shell and one monolayer of CdTe nanocrystals. The nanocrystal emission is highly tuneable through the particle size. CdTe nanocrystals can be produced for emission in the spectral region between around *510 nm* and *730 nm*. A thin PE layer is required on the sphere surface for the deposition of nanocrystals. The PE multilayers and the nanocrystals are bound to the surface by an electrostatic attraction. In order to produce a novel active microsphere emitter, the PE layer was increased to several nanometers (about *15 nm* maximum thickness) and additionally softened by a chemical treatment with NaCl which increased the elasticity of the shell. Samples with different shell thickness were produced. Furthermore, Rhodamine B dye coated microspheres without a PE layer were used for parts of the experimental work. The spectra were taken in the optical region with a commercial micro-PL/micro-Raman setup.

A HeNe laser (*632.8 nm*) and an Ar^+-ion laser (*457 nm*, *488 nm*, and *514 nm*) were used to excite the samples.

In chapter 4, a single microsphere was optically characterised by excitation below and above the first electronic transition of the CdTe nanocrystals which were deposited on the sphere surface. Strong photoluminescence was observed at on-resonance excitation and a remarkably high PL signal at off-resonance excitation when excited with the HeNe laser, attributed to a highly efficient phonon-assisted up-conversion process. An LO-Raman mode of CdTe as well as Raman modes from the polystyrene sphere was observed in the spectrum, demonstrating the strong enhancement of photoluminescence and Raman scattering due to the optical feedback, induced by the multiple recirculation of the light which was trapped within the microsphere. The whispering gallery mode spectrum revealed a periodic intensity fluctuation of the modes due to an interference effect in the microsphere. Based on earlier theoretical work, a rough estimation of the refractive index of the coated microsphere was made derived from the interference periodicity. The samples were excited for 18 minutes under continuous excitation with the laser beam to study changes in the photoluminescence intensity and changes of the whispering gallery modes. A spectrum was taken every 30 seconds during excitation. The long exposure time revealed an exponential decay of photoluminescence from the nanocrystals, probably due to an irreversible photo-oxidation process. A periodic recovery superimposed to the exponential decay was observed which is attributed to charging effect of electronic trap levels in the nanocrystals. A FFT was carried out on the PL spectra of the measurement series to detect changes in the free spectral range of the resonances. A blue shift of the whispering gallery modes was observed during continuous excitation. The spectral shift was attributed to a refractive index change due to heating of the sample. The shift showed a linear dependence with excitation time.

In chapter 5, the microsphere samples with a several nanometer thick PE shell additionally softened by a chemical treatment was utilized for a novel experiment in an optical trap. The top layer of the PE shell was coated with the CdTe nanocrystals. Radiation pressure exerted on the microsphere emitter was controlled by the position of the focus along the z-axis in vertical direction. The focus dependent radiation force was first calculated. The variation of radiation pressure applied a downward or upward force on the microsphere due to optical trapping in the laser beam. The elastic shell of the sample was deformed by radiation pressure and the changes in the whispering gallery mode spectrum

induced by the soft shell deformation was analysed with an mathematical model based on azimuthal mode splitting in a spherical microcavity due to deformation. The model fit very well with the experimental data. The deformation of an elastic shell deposited on an active microcavity is a new approach which is not reported elsewhere yet. Up to now, deformation of microspheres was achieved by applying mechanical stress. The experiment reported in this thesis is the first attempt for a shape distortion of a solid microcavity by radiation force. This chapter also provides an optical switching experiment based on the optically-induced deformation technique. Furthermore, spectral blue-shift of the whispering gallery modes within a range of several nanometers in wavelength was observed due to a heating effect of the microcavity. The shift showed a clear dependency on the laser intensity. A rough estimation for the temperature increase of the sample was carried out based on data found in the literature. The only publication of a wavelength shift over several nanometers is reported to be observed in Rhodamine B doped waterdroplets. The modes were tuned by droplet size control in a humidity chamber. The setup is bulky and more complex in comparison to our experiment.

In chapter 6, intersphere coupling in a bi-sphere system was studied depending on the excitation position. A polystyrene pore substrate was utilized to align the bi-sphere system in a stable configuration with minimal contact between the substrate and the sphere to avoid a reduction of the Q-factor. Highly efficient coherent coupling in a bi-sphere system consisting of Rhodamine B dye coated microspheres with a diameter of *3 μm* was observed. The difference in size between both spheres was *6 nm*. The coupled optical resonances split into bonding and anti-bonding modes comparable to energy level splitting in a hydrogen molecule. The weak intersphere coupling was studied at different excitation configurations. Switching between resonances depending in the focus position was demonstrated as an example for a potential application in optical communications as an optical switch or add-drop filter. The technical limits for this approach are discussed. Depending on the applied method, mainly the switching of the excitation position is the limiting factor for switching speed between optical channels. In conclusion, this thesis provides new data about optical characterisation of a novel active microcavity with potential for further research in different fields of application. A novel method for azimuthal mode splitting based on deformation of an elastic shell applied on a spherical microcavity was presented. The new approach was the deformation achieved solely by radiation pressure.

7.2 Outlook

The novel nanocrystal coated microsphere emitter show great potential for photonic applications and fundamental science due to their combined unique properties of spherical microcavities and semiconductor nanocrystals. The fabrication process is a straight forward and little cost-intensive. Applications based on this micro-emitter would require photostable nanocrystals with constant photoluminescence efficiency. A solution to the problem of photo-oxidation is necessary as our measurements reveal strong photoluminescence decay in an oxygen atmosphere. In a sealed atmosphere, the nanocrystals provide the advantage of high quantum efficiency at room temperature which makes them suitable for laser applications. Further studies could aim at low-threshold lasing when applying an efficient method to couple the light into and out of the system. Evanescent coupling is the most promising way for high efficiencies. Further studies towards sensor application would be of interest due to the high sensitivity of the whispering gallery modes to changes of the refractive index of the sphere material, the material deposited on the sphere surface and the surrounding medium. The wide temperature-induced shift of the optical resonances also shows potential for sensor applications such as temperature sensors for confined spaces or localised temperature measurements in the micrometer region with high sensitivity. The large spectral shift shows great potential for experiments where spectrally wide tuning ability is important. For example in the field of optical coupling of microcavities, the proper sphere size is usually required for optimal mode frequency selection. Thermal mode tuning opens the possibility for tuning to the desired frequency to optimise optical coupling. A sensor application which might be worth further studies was proposed in chapter 4. Monitoring the shifting speed of the resonances in-situ over time might provide real time information of changes in the surrounding medium sensed by the active microcavity. The strong enhancement of light-matter interaction due to the optical feedback in the microcavity suggests new experiments in linear and non-linear optics. Different materials could be deposited on the sphere surface to study effects such as two-photon absorption, four-wave mixing or higher-harmonics generation. Experiments in optoelectronics based on coated microspheres could greatly benefit from the enhancement due to the optical feedback. The

novel soft shell microsphere emitter could be utilized as a potential stress sensor, either for mechanical strain or more interesting, as a radiation pressure sensor. Improving the radiation-pressure controlled azimuthal mode splitting caused by shell deformation could be potentially applicable for various experiments, such as optical switching, or controlled coherent coupling of azimuthal modes in photonic molecules. As strong coherent coupling is already demonstrated between two active microspheres in this thesis, further work is in progress, where multi-sphere coupling is studied. Symmetric photonic molecules consisting of more than 2 microspheres have potential capabilities to realise strong directional emission generated by coupled modes or photonic nanojets. By tuning the gap size between the coupled spheres, a considerable lowering of the laser threshold and an extreme enhancement of the Q-factor is predicted in theory. Further experimental work which takes advantage of the elastic shell on the microspheres is possible. For example, the elastic layer suggests experiments to study micro-oscillations excited with light pulses in the microcavity. Possibly, studies of other elastic materials for deposition on the sphere surface are valuable for further oscillation and deformation experiments.